

PRODUCTION OF AMORPHOUS SILICON/ P-TYPE CRYSTALLINE SILICON  
HETEROJUNCTION SOLAR CELLS BY SPUTTERING AND PECVD METHODS

A THESIS SUBMITTED TO  
THE GRADUATE SCHOOL OF NATURAL AND APPLIED SCIENCES  
OF  
MIDDLE EAST TECHNICAL UNIVERSITY

BY

ZEYNEP DENİZ EYGİ

IN PARTIAL FULFILLMENT OF THE REQUIREMENTS  
FOR  
THE DEGREE OF DOCTOR OF PHILOSOPHY  
IN  
PHYSICS

DECEMBER 2011

Approval of the Thesis:

**PRODUCTION OF AMORPHOUS SILICON/ P-TYPE CRYSTALLINE  
SILICON HETEROJUNCTION SOLAR CELLS BY SPUTTERING AND PECVD  
METHODS**

Submitted by **ZEYNEP DENİZ EYĞİ** in partial fulfillment of the requirements for the degree of **Doctor of Philosophy in Physics Department, Middle East Technical University** by,

Prof. Dr. Canan Özgen  
Dean, Graduate School of **Natural and Applied Sciences** \_\_\_\_\_

Prof. Dr. Sinan Bilikmen  
Head of Department, **Physics** \_\_\_\_\_

Prof. Dr. Raşit Turan  
Supervisor, **Physics Dept., METU** \_\_\_\_\_

Prof. Dr. Çiğdem Erçelebi  
Co-Supervisor, **Physics Dept., METU** \_\_\_\_\_

**Examining Committee Members:**

Prof. Dr. Mehmet Parlak  
Physics Dept., METU \_\_\_\_\_

Prof. Dr. Raşit Turan  
Physics Dept., METU \_\_\_\_\_

Prof. Dr. Aynur Eray  
Physics Engineering Dept, Hacettepe University \_\_\_\_\_

Prof. Dr. Bahtiyar Salamov  
Physics Dept., Gazi University \_\_\_\_\_

Assist. Prof. Dr. Alpan Bek  
Physics Dept., METU \_\_\_\_\_

**Date:** \_\_\_\_\_

**I hereby declare that all information in this document has been obtained and presented in accordance with academic rules and ethical conduct. I also declare that, as required by these rules and conduct, I have fully cited and referenced all material and results that are not original to this work.**

Name, Last Name: ZEYNEP DENİZ EYĞİ

Signature:

## ABSTRACT

### PRODUCTION OF AMORPHOUS SILICON / P-TYPE CRYSTALLINE SILICON HETEROJUNCTION SOLAR CELLS BY SPUTTERING AND PECVD METHODS

Eygi, Zeynep Deniz

Ph.D. Department of Physics

Supervisor : Prof. Dr. Raşit Turan

Co-Supervisor : Prof. Dr. Çiğdem Erçelebi

December 2011, 126 pages

Silicon heterojunction solar cells, a-Si:H/c-Si, are promising technology for future photovoltaic systems. An a-Si:H/c-Si heterojunction solar cell combines the advantages of single crystalline silicon photovoltaic with thin-film technologies. This thesis reports a detailed survey of heterojunction silicon solar cells with p-type wafer fabricated by magnetron sputtering and Plasma Enhanced Chemical Vapor Deposition (PECVD) techniques at low processing temperature. In the first part of this study, magnetron sputtering method was employed to fabricate a-Si:H thin films and then a-Si:H/c-Si solar cells. Amorphous silicon (a-Si:H) films were grown on glass in order to perform electrical and optical characterizations. The J-V characteristics of the silicon heterojunction solar cells were analyzed as a function of a-Si:H properties. It was shown that a-Si thin films with well-behaved chemical and electronic properties could be fabricated by the magnetron sputtering. Hydrogenation of the grown film could be achieved by H<sub>2</sub> introduction into the chamber during the sputtering. In spite of the good film properties, fabricated solar cells had poor photovoltaic parameters with a low

rectification characteristic. This low device performance was caused by high resistivity and low doping concentration in the sputtered film. The second part of the thesis is dedicated to heterojunction solar cells fabricated by PECVD. In this part a systematic study of various PECVD processing parameters were carried out to optimize the a-Si:H(n) emitter properties for the a-Si:H(n)/c-Si(p) solar cell applications. In the next stage, a thin optimized a-Si:H(i) buffer layer was included on the emitter side and on the rear side of the c-Si(p) to improve the surface passivation. Insertion of an a-Si:H(i) buffer layer yielded higher high open circuit voltage ( $V_{oc}$ ) with lower fill factor. It was shown that high  $V_{oc}$  is due to the efficient surface passivation by the front/rear intrinsic layer which was also confirmed by the measurement of high effective lifetime for photo-generated carriers. Low fill factor on the other hand is caused by increasing resistivity of the solar cells by inserting low conductivity a-Si:H(i) layers.

Keywords: Heterojunction solar cell, magnetron sputtering, PECVD.

# ÖZ

## AMORF SİLİSYUM/P-TİPİ KRİSTAL SİLİSYUM HETEROEKLEM GÜNEŞ GÖZELERİNİN SAÇTIRMA VE PECVD TEKNİĞİ İLE ÜRETİLMESİ

Eygi, Zeynep Deniz

Doktora, Fizik Bölümü

Tez Yöneticisi: Prof. Dr. Raşit Turan

Ortak Tez Yöneticisi: Prof. Dr. Çiğdem Erçelebi

Aralık 2011, 126 sayfa

Silisyum heteroeklem a-Si:H/c-Si güneş gözeleri gelecekteki fotovoltaik sistemler için umut vaat eden bir teknolojidir. a-Si:H/c-Si heteroeklem güneş gözesi, yüksek verimli kristal silisyum ve ince film teknolojilerinin bir birleşimidir. Bu tez çalışmasında düşük sıcaklıkta magnetron saçtırma ve plazma destekli kimyasal buhar biriktirme (PECVD) teknikleri ile büyütülen p-tipi heteroeklem silisyum güneş gözeleri ayrıntılı bir şekilde anlatılmıştır. Çalışmanın ilk kısmında, magnetron saçtırma yöntemi kullanılarak ince amorf silisyum (a-Si:H) filmler ve a-Si:H/c-Si heteroeklem güneş gözeleri üretilmiştir. a-Si:H filmleri elektriksel ve optiksel karakterizasyonlarının yapılabilmesi için cam alt taş üzerine üretilmiştir. Üretilen güneş gözelerinin değişen malzeme yapısı ve deney parametrelerine göre akım yoğunluğu-voltaj özellikleri incelenmiştir. Magnetron saçtırma yöntemiyle üstün kimyasal ve elektronik özellikli a-Si ince filmler üretilebildiği gösterilmiştir. Üretim sırasında büyütme kazanına hidrojen gazı eklenerek hidrojenlenmiş amorf silisyum filmler elde edilmiştir. Bu metodla yüksek kalitede filmler elde edilmesine karşın, üretilen güneş gözelerinde

düşük doğrultma özelliği ve zayıf fotovoltaik performans gözlenmiştir. Güneş gözelerindeki düşük performans sebebinin yüksek direnç ve filmlerdeki katkılama oranının yetersizliği olduğu sonucuna varılmıştır.

Tezin ikinci bölümü ise PECVD tekniği tarafından üretilmiş güneş gözeleri çalışmaları için ayrılmıştır. Bu kısımda, çeşitli PECVD üretim parametrelerine bağlı olarak elde edilen a-Si:H(n) filmler güneş gözeleri uygulamaları için optimize edilmiştir. Çalışmanın bir diğer aşamasında yüzey pasivasyonu artırmak amacıyla c-Si alt taşının ön ve arka yüzlerine a-Si tampon tabaka büyütülmüştür. Güneş gözesine eklenen bu tampon tabakaların açık devre voltajını ( $V_{oc}$ ) artırırken dolun çarpanının (FF) düşmesine neden olduğu gözlenmiştir. Artan açık devre voltajının iyileştirilmiş yüzey pasivasyonuna bağlı olduğu yük taşıyıcılarının yaşam ömürlerinin belirlenmesiyle tayin edilmiştir. Öte yandan düşük dolun çarpanının ise a-Si:H filmlerindeki düşük iletkenliğin güneş gözesinde neden olduğu yüksek dirençten kaynakladığı saptanmıştır.

Anahtar kelimeler: Heteroeklem güneş gözesi, magnetron saçtırma, PECVD

*To my family*

## ACKNOWLEDGMENTS

There are many people whom it is a pleasure to thank for their help and advice during the preparation of this thesis.

In the first place, I would like to thank to my supervisor Prof. Dr. Raşit Turan for his advice, guidance and excellent support during my PhD studies. He gave me the opportunity to work in his research group and introduced me to solar cell studies. I also thank him for his friendly attitude towards to me.

It gives me great pleasure in acknowledging to Prof.Dr. Robert Birkmire and Dr. Steve Hegedus for giving me the opportunity to study at Institute of Energy Conversion (IEC), University of Delaware. It was a great experience for me to be a visiting scholar one and half year at IEC. I believe this thesis would have not been possible without contribution of IEC. I hope to continue our collaboration in the future.

I would like to show my gratitude to Dr. Steve Hegedus for his advice, supervision and crucial contribution to my research and this thesis. I also thank him for his technical and personal support, and friendly behavior.

I gratefully thank Dr. Ujjwal Das. I have greatly benefited from his experiences, valuable comments and guidance. I also thank him for always being patient and kind to me for answering my questions about Si heterojunction solar cells, PECVD and all other experimental issues.

I would also like to acknowledge my co-advisor, Prof. Dr. Çiğdem Erçelebi, for her support and valuable comments on my dissertation.

I would like to thank to my thesis committee; Prof. Dr. M. Parlak, Prof. Dr. A. Eray, Prof. Dr. B. Salamov, Assist. Prof. Dr. A. Bek ; for their beneficial criticism on my thesis.

It is a pleasure to convey my gratitude to my colleagues and friends both from METU and IEC. Umut Bostancı, I thank you for teaching me how to use sputtering.

Mustafa Kulakçı, I appreciate for your help, advice and nice chats while sharing snacks with me.

Dr. A. İmer, M. Karaman, O. Demircioğlu, B.Kaleli and F. Es thanks for being around whenever I needed help. Thank you Y. Eke for your technical support. L. Zhang and L. Zhu thank you for all your helps during learning PECVD. L. Zhang and L. Zhu, thank you for all your help while I learned PECVD. I thank S. Mudigonda for her friendship and help in the measuring of my solar cells.

Many thanks go to John Allen for his friendship and support for both technical and personal issues. I also thank him for his patience with my questions!

I present my special thanks to Dr. Murat Kaleli. I am pleased by your friendly help in the laboratory, which made the work more fun.

Iraklis Argyriou, I thank you for your comments on my thesis drafts.

Special thanks to Agnijit Das Gupta who boosted me morally whenever it was needed. Thanks for your care, help and efforts to make my more enjoyable in Newark.

I would like to say a big thank you to the academic and administrative staff in the Department of Physics, METU, Z. Eke, G. Parlak, and in IEC, Paula Newton and Teresa Tritt, who kindly dealt with every kind of formal task.

I owe my deepest gratitude to my parents, my sisters and my aunts for their love and support throughout my life. I especially thank my mother Hatice Eygi. Without her endless encouragement and support this work would have been impossible. I should also thank my nephew Emin and my niece Esma whom made me always smile with their lovely encouragements.

Finally I am thankful to my all dears friends, of whom I have felt all of their encouragement and moral support.

# TABLE OF CONTENTS

|   |     |
|---|-----|
| ABSTRACT.....   | iv  |
| ÖZ .....  | vi  |
| ACKNOWLEDGMENTS.....  | ix  |
| TABLE OF CONTENT .....  | xi  |
| LIST OF TABLES .....  | xiv |
| LIST OF FIGURES.....  | xv  |
| CHAPTERS  |     |
| 1. INTRODUCTION.....  | 1   |
| 1.1 Overview to Energy Demand and PV .....                        | 1   |
| 1.2 Current Photovoltaic (Solar) Cell Technologies .....          | 4   |
| 1.2.1 Thin Film Solar Cell Technologies .....                     | 6   |
| 1.3 a-Si:H / c-Si Heterojunction.....                             | 9   |
| 1.4 Thesis Statement .....  | 14  |
| 1.5 Thesis Outline .....  | 15  |
| 2. a-Si:H / c-Si HETEROJUNCTION MODEL .....                       | 17  |
| 2.1 Heterojunction Fundamentals .....                             | 17  |
| 2.2 Solar Cell Principles in p-n Homojunction .....               | 24  |
| 2.3 p-n Heterojunction Solar Cells.....                           | 27  |
| 2.4 Losses in Heterojunction Solar Cells SRH Recombination.....   | 30  |
| 2.5 Reducing Recombination.....                                   | 34  |
| 3. EXPERIMENTAL: FABRICATION AND CHARACTERIZATION TECHNIQUES..... | 36  |
| 3.1 Fabrication Techniques .....                                  | 36  |
| 3.1.1 Plasma Enhanced Chemical Vapor Deposition: PECVD .....      | 37  |
| 3.1.2 Sputtering Deposition.....                                  | 40  |

|       |  |    |
|-------|--|----|
| 3.1.3 | Substrate Cleaning .....   | 43 |
| 3.1.4 | a-Si:H /c-Si Solar Cell Fabrication by PECVD .....   | 44 |
| 3.2   | Characterization Techniques .....  | 47 |
| 3.2.1 | Quantum Efficiency .....   | 47 |
| 3.2.2 | Current Density-Voltage Measurements .....   | 50 |
| 3.2.3 | Effective Minority Carrier Lifetime Measurement .....  | 55 |
| 3.2.4 | Conductivity Measurement .....   | 60 |
| 3.2.5 | Transmission and Reflection Measurements .....   | 61 |
| 4.    | SHJ SOLAR CELLS FABRICATED BY MAGNETRON SPUTTERING .....                                     | 63 |
| 4.1   | Amorphous Silicon Films Deposited by DC Magnetron Sputtering<br>Technique.....               | 63 |
| 4.1.1 | Experimental .....   | 64 |
| 4.1.2 | Results and Discussion.....  | 65 |
| 4.2   | Hydrogenated Amorphous Silicon Films Deposited by RF Magnetron<br>Sputtering Technique ..... | 67 |
| 4.2.1 | Experimental .....   | 67 |
| 4.2.2 | Results and Discussion.....  | 68 |
| 4.3   | SHJ Solar Cells by Magnetron Sputtering .....  | 72 |
| 4.4   | Conclusion.....  | 74 |
| 5.    | a-Si:H (n) / c-Si (p) SOLAR CELLS .....  | 75 |
| 5.1   | Introduction .....   | 75 |
| 5.2   | Experimental .....   | 77 |
| 5.3   | Results and Discussion.....  | 78 |
| 5.3.1 | Effect of PH <sub>3</sub> Gases Flow Rate .....  | 78 |
| 5.3.2 | Temperature Effect.....  | 81 |
| 5.3.3 | DC Plasma Current Effect.....  | 86 |
| 5.3.4 | Hydrogen Effect .....  | 88 |
| 5.3.5 | Thickness Effect:.....   | 90 |
| 5.4   | Conclusion.....  | 92 |
| 6.    | a-Si:H/ c-Si HETEROJUNCTION SOLAR CELLS WITH i-LAYER.....                                    | 94 |

|       |   |     |
|-------|---|-----|
| 6.1   | Introduction.....   | 94  |
| 6.2   | Effect of Hydrogen Dilution Ratio and Plasma DC on a-Si:H (i) Layer and It's Passivation Quality Effect ..... | 96  |
| 6.2.1 | Results and Discussion.....   | 97  |
| 6.3   | Effect of a-Si:H (i) Layer Thicknesses on the SHJ Cells.....  | 102 |
| 6.4   | Temperature Dependence of J-V Analysis .....  | 107 |
| 6.5   | Conclusion.....   | 110 |
| 7.    | CONCLUSION .....  | 111 |
|       | REFERENCES.....   | 114 |
|       | CIRRICULUM VITAE.....   | 124 |

## LIST OF TABLES

### TABLES

|  |     |
|--|-----|
| Table 1: The best Voc and efficiency values of SHJ solar cells on p-type and n-type c-Si by several groups . . . . .   | 14  |
| Table 2: Steady-state number density of radicals, emissive species and ions in a realistic silane plasma . . . . .   | 39  |
| Table 3: a-Si deposition condition parameters by DC magnetron sputtering. . . . .  | 66  |
| Table 4: The band gap of a-Si:H films deposited at different RF power and temperature. . . . .   | 71  |
| Table 5: The resistivity values of two samples deposited at two different power and H <sub>2</sub> flow rate. . . . .  | 72  |
| Table 6: Conductivity, R <sub>MF</sub> , band gap and lifetime of a-Si:H films depending on PH <sub>3</sub> flow rate. . . . .   | 79  |
| Table 7: Solar cell parameters with different emitter layer PH <sub>3</sub> gas flow rate and R <sub>s</sub> values calculated from dV/dJ vs 1/J curve. . . . .                | 80  |
| Table 8: Band gap, R <sub>MF</sub> , and conductivity results by varying deposition temperature. . . . .   | 81  |
| Table 9: Properties of the thin a-Si:H(n) films, measured from T&R and FTIR for increasing DC plasma current. . . . .  | 87  |
| Table 10: p-type SHJ solar cell J-V parameters with different emitter layer deposition currents. The results are the averages of three different samples for each run. . . . . | 87  |
| Table 11: PV characteristic parameters of SHJ solar cells with varying values of R. . . . .  | 89  |
| Table 12: The J <sub>0</sub> , n values evaluated from the temperature dependent J-V curves of SHJ solar cell with 3nm i buffer layer. . . . .                                 | 108 |

## LIST OF FIGURES

### FIGURES

|   |    |
|---|----|
| Figure 1.2-1: Best research solar cell efficiencies reported by NREL .....  | 9  |
| Figure 1.3-1: Illustration of p-type SHJ (a) and HIT (b) cell structures. ....  | 11 |
| Figure 2.1-1: Band lines of two isolated distinct semiconductors. ....  | 18 |
| Figure 2.1-2: Band diagram of a heterojunction at equilibrium formed between two<br>semiconductors.....   | 18 |
| Figure 2.1-3: Equilibrium band line-up of a a-Si:H(n)/c-Si(p) heterojunction and<br>possible transport paths for moderate forward bias . ....   | 21 |
| Figure 2.1-4: A $\ln(J)$ -V graph. At low biases, the recombination effects in depletion<br>region are dominant. At higher biases the slope becomes closer to unity. At highest<br>bias the behavior becomes more ohmic. ....   | 23 |
| Figure 2.2-1: The energy band profiles (a) of a p-n diode (solar cell) in the equilibrium<br>(b) under illumination.....  | 26 |
| Figure 2.3-1: High potential barrier in the valance band prevents holes from p side to n<br>side. As the potential barrier in conduction band is smaller than the barrier in the<br>valance band, electrons can transport toward to n side of the heterojunction..... | 27 |
| Figure 2.3-2: Schematic showing of photon absorption and window effect of emitter..   | 28 |
| Figure 2.3-3: Band diagram of a-Si:H(p) back-surface field for SHJ solar cell on p-<br>type c-Si substrates. BSF created by p type doped a-Si:H keeps minority carriers<br>away from high recombination surface.....  | 29 |
| Figure 2.3-4: Schematic band diagram of HIT structure on p-type c-Si .....  | 30 |
| Figure 2.4-1: Major recombination mechanism in semiconductors.....  | 31 |
| Figure 2.4-2: Four possible interactions of free carrier with localized states by electron<br>and hole ( $r_1$ and $r_3$ ) capture and emission ( $r_2$ and $r_4$ ) respectively.....   | 32 |
| Figure 3.1-1: Schematic cross-section of a deposition chamber in PECVD.....   | 37 |

|   |    |
|---|----|
| Figure 3.1-2: Steady-state number density of radicals, emissive species, and ions in realistic silane plasma .....  | 40 |
| Figure 3.1-3: The schematic representation of magnetron sputtering chamber.....   | 42 |
| Figure 3.1-4: Picture of nano-D100 sputtering system .....  | 42 |
| Figure 3.1-5: Picture of the sputtering chamber.....  | 43 |
| Figure 3.1-6: A basic diagram of multi chamber PEVCD system at IEC.....   | 45 |
| Figure 3.1-7: Sketch of shadow mask for ITO deposition on the front side of SHJ solar cell .....  | 46 |
| Figure 3.1-8: Picture of a complete cell (a) and the sketch of bus bar mask for Ni/Al deposition on ITO (b).....  | 47 |
| Figure 3.2-1: Possible reduction in quantum efficiency of a silicon solar cell is shown. Ideal quantum efficiency has a rectangular shape with a QE of 1 at whole spectra   | 48 |
| Figure 3.2-2: Optical Stage of the QE system at IEC. A) Light source, B) Filter wheel, C) Monochromator, D) Light chopper, E) Collimating and focusing lenses, F) Sample stage.....   | 49 |
| Figure 3.2-3: Example of a current density voltage (J-V) curve and the characteristic parameters. ....  | 51 |
| Figure 3.2-4: The equivalent circuit of an ideal solar cell .....   | 52 |
| Figure 3.2-5: The equivalent circuit of a solar cell with series and shunt resistance.....  | 53 |
| Figure 3.2-6: Picture of JV system. The simulator lamp shines on the sample placed on the stage. On the right is the source measurement unit which sweeps the voltage and measures the current. ....  | 55 |
| Figure 3.2-7: Solar simulator used for JV analysis of the cells deposited by sputtering.  | 55 |
| Figure 3.2-8: Figure of QSSPC setup for effective lifetime measurement. The inductively coupled coil with RF bridge circuit detects the photo conductivity changes of the sample. The reference cell evaluates the generation rate of illumination light. Both signals are amplified and preceded by an oscilloscope and recorded by software ..... | 57 |
| Figure 3.2-9: Flash lamp light intensity and photo conductance decay as a function of time.....   | 59 |
| Figure 3.2-10: Picture of Sinton WCT100 for effective lifetime measurement. ....  | 59 |

|   |    |
|---|----|
| Figure 3.2-11: The shadow mask using for conductivity measurements.....   | 60 |
| Figure 4.1-1: Dependence of $(\alpha h\nu)^{1/2}$ on photon energy for 200 nm a-Si film deposited at room temperature . .....   | 65 |
| Figure 4.1-2: Raman shift spectra of a-Si films deposited at four different temperatures.66   |    |
| Figure 4.2-1: FTIR spectra of films deposited under the hydrogen flow rate of 3 sccm for 150 W DC power, 5 sccm for 100W RF power and 10,15 sccm for 200 W RF power.....  | 68 |
| Figure 4.2-2: The Raman spectra of the samples deposited at RF power of 100 W and 200 W with the $H_2$ flow rate of 5, 10 and 15 sccm. ....   | 69 |
| Figure 4.2-3: The Raman spectra of the samples deposited at RF power of 200 W with the $H_2$ flow rate of 10 sccm with varying substrate temperatures of 30, 200 and 300 °C.....  | 70 |
| Figure 4.3-1: J-V characteristics for a-Si:H(n)/c-Si(p) heterojunction and the effect of illumination. ....   | 73 |
| Figure 4.3-2: Illuminated J-V measurements of samples deposited by magnetron sputtering.....  | 73 |
| Figure 5.1-1: Band diagram of a-Si:H/c-Si heterojunction and possible recombination paths due to : defect states in the c-Si (1), defects at Si:H / c-Si interface (2), disorder in the a-Si:H. Defects states are indicated by dash lines..... | 76 |
| Figure 5.2-1: The diagram of Ni-Al Grids/ ITO/ a-Si:H(n) / c-Si (p) / a-Si:H (p) / Al ..  | 77 |
| Figure 5.3-1: JV curves of the devices summarized in Table 2. While $R_s$ increase the J-V curve becomes more “S” shape.....  | 81 |
| Figure 5.3-2: FTIR spectra of a-Si:H(n) films at different deposition temperatures at 123 mA.....   | 82 |
| Figure 5.3-3: FF vs $V_{oc}$ of four SHJ cells with emitter layers deposited at 200 and 250 °C. Their $V_{oc}$ values vary around the same values.....  | 83 |
| Figure 5.3-4: Plot of $dV/dJ$ vs. $1/J$ curves for the solar cells whose emitter layers are deposited at 200 °C and 250 °C.....   | 84 |
| Figure 5.3-5: J-V curve of Al-Ni / a-Si:H(p) /c-Si(p) / a-Si:H (p) /Al.....   | 85 |
| Figure 5.3-6: J-V curve of ITO/ a-Si:H(n) /c-Si(n)/ a-Si:H(n) /Al .....   | 86 |

|   |     |
|---|-----|
| Figure 5.3-7: The JV curve of SHJ cells deposited at different DC plasma powers at the temperature of 250 °C. ....  | 88  |
| Figure 5.3-8: Raman spectra of emitter a-Si:H(n) layers deposited at different R values.  | 90  |
| Figure 5.3-9: Solar cell parameters of p-type SHJ with varying emitter a-Si:H(n) thicknesses.....   | 91  |
| Figure 5.3-10: QE of SHJ with the emitter a-Si:H(n) thickness of 10, 20, and 30 nm...   | 92  |
| Figure 5.4-1: Schematic of SHJ solar cell and high-resolution transmission electron microscopic image of abrupt c-Si(p)/a-Si:H(n).The picture was taken from High resolution TEM located in Central Lab. at METU..... | 93  |
| Figure 6.1-1: Illustration of a-Si:H deposited on c-Si surface as four layers .....   | 95  |
| Figure 6.2-1: Effective minority life times, $\tau_{\text{eff}}$ , of a-Si:H (i) / c-Si(p) / a-Si:H (i) structures as a function of R at the DC plasma of 60 and 123mA. ....  | 98  |
| Figure 6.2-2: Comparison of FTIR spectra of 10 nm thick a-Si:H(i) layers grown by two different DC plasma process under R=2.5. ....   | 99  |
| Figure 6.2-3: Comparison of FTIR spectra of 10 nm thick a-Si:H(i) layers grown by two different DC plasma process with R=2 .....  | 100 |
| Figure 6.2-4: FTIR spectra of 10 nm thick a-Si:H(i) layers grown by three different R at a constant DC plasma (123mA) .....   | 101 |
| Figure 6.3-1: J-V curves of Ni-Al grids / 70 (nm) ITO / a-Si:H (n) / c-Si (p) /Al hetero-junction solar with and without a-Si:H(i) buffer layers. ....  | 103 |
| Figure 6.3-2: Solar cell parameters of the SHJ plotted as a function of a-Si:H(i) layer thickness. ....   | 104 |
| Figure 6.3-3: J-V curves of Ni-Al grids / 70 (nm) ITO / a-Si:H (n) / c-Si (p) / Al hetero-junction solar with different thickness of a-Si:H(i) buffer layers. ....  | 105 |
| Figure 6.3-4: The QE spectra of SHJ cells with and without i-layer. ....  | 105 |
| Figure 6.3-5: The QE spectra of SHJ cells with varying i-layer thicknesses.....   | 106 |
| Figure 6.4-1: Semi-logarithmic graph of forward dark current density at different temperatures. ....  | 107 |
| Figure 6.4-2: The plot of $\ln(J_0)$ vs. $1000/T$ for the SHJ cell with 3nm i layer.....  | 109 |

# CHAPTER 1

## INTRODUCTION

### 1.1 Overview to Energy Demand and PV

The energy demand is continuously increasing by industrial development, growing population and increasing standards of modern life. The report of International Energy Agency (IEA) points out that world primary energy demand will be expanding by almost 60% within 20 years, with an average annual increase of 1.7% per year [1]. Conversely, in some poor countries, mainly in their rural areas, there is inadequate access to electricity for daily life (cooking, heating, health etc.).

Currently the main energy sources used to cover energy demand are non-renewable fossil fuels (gasoline, fuel oil, coal etc.) and nuclear power. However, fossil fuels are being depleted over time and their cost is increasing due to their limited availability. Additionally, the exploitation of fossil fuels is associated with negative impact on the environment due to the emission of air pollutants and greenhouse gases (e.g. CO<sub>2</sub>, CO, SO<sub>2</sub> and P<sub>2</sub>O<sub>5</sub>) which cause pollution and contribute to global warming. In nuclear power, the energy arises from the nuclear fission of radioactive elements like Uranium and Plutonium which are toxic and dangerous. Also, nuclear power stations are subject to safety risks. For example, the built of reactors and the management of nuclear waste products are major problems for the nuclear power.

The increasing demand for energy coupled with a diminishing availability of fossil fuel resources and relevant environmental problems are the main driving forces in searching for and paying more attention to alternative energy sources. Renewable energy sources which are reliable, clean and reasonably priced are the best option for satisfying today's and future's energy demand. Renewable energy means a source of

energy that has the capacity to replenish itself. They are natural and unlimited energy supplies. Renewable energy is also considered as clean energy, since it does not produce toxins or pollutants that are harmful to the environment in the same manner that non-renewable energy does. Renewable energy can be exploited for electricity generation, transportation, and thermal energy applications. Hydropower, biomass, wind power, and solar power (thermal and photovoltaic) are the main renewable energy sources. Renewable energy accounted for 8% of the world's total energy demand in 2010. Besides their widespread geographical availability, the use of renewable sources varies between countries and regions.

Biomass energy is commonly used for cooking and heating. Biomass is a kind of energy originated from plants such as woods. Using biomass energy causes air pollution due to release of large amounts of carbon dioxide gases into the atmosphere. Thus it is questionable whether biomass can be accounted as a clean renewable energy source.

Hydropower is the second-largest renewable energy sources used for the satisfaction of world electricity demand. However, hydroelectric systems rely on expensive generator systems whose installation is technically difficult. Also hydroelectric systems can have disastrous effects for the surrounding environment, wildlife and river life.

Wind power involves the conversion of wind energy into electricity using wind turbines. However, wind turbines are complex and expensive structures whose operation is becoming challenging. The main disadvantage of wind power is the need for alternative generating (backup) power capacity to match supply when there is no available wind energy; such a requirement increases the operational costs of wind energy. Among the renewable energy sources solar power systems, and specifically photovoltaic technology, have more advantages although currently the electric consumption from solar cells is still small compared to other renewable energy systems. Photovoltaic power generates electricity directly from the sun with easy installation parts and without any contribution to the air pollution. Electricity generation from solar power is expected to reach 119 TWh in 2030 [1]. 80% of which will be from photovoltaics (PV), while the rest will be produced in solar thermal power plants.

The photovoltaic technology has the highest investment and generating costs among all renewable energy technologies. Electricity generation from PV is economically most attractive in areas with abundant sunshine and high electricity prices.

The photovoltaics involve the conversion of light into electricity by means of solar cells. The solar cells are the main building block of the electric generation from the sun light. These cells are typically made of semiconductor materials. A number of solar cells are connected to each other in series or parallel to a mounted frame called "solar module" or "solar panel". Modules are designed to supply energy at a certain voltage. Several modules can be wired together to form an array whose usage can be very practical. The solar arrays can operate continuously without maintenance, which limits their cost to the initial investment needed for their purchase and installation. The solar panels generally last 25 years or longer.

Photovoltaic power is one of the most promising and fastest growing renewable energy sources. The number of researches and volume manufacturing of solar cells and modules have been considerably increasing recently. In 2010, solar photovoltaic generates electricity in more than 100 countries. However, the generated power from solar cells is still a small fraction of the total global power generated from other energy sources to cover today's world energy demand.

Under present conditions, PV energy sources are more expensive than fossil fuels. One of the important reasons for this cost difference is the high manufacturing cost of photovoltaics. For this reason, it is important to use fewer amounts of materials when fabricating high efficiency solar cells. Additionally, the electrical and optical designs of high efficiency solar cells have been studied to improve the efficiency of the solar cells.

## 1.2 Current Photovoltaic (Solar) Cell Technologies

The first solar cell was constructed by Charles Fritts in 1877 by using junctions formed by coating the semiconductor selenium with an ultra thin layer of gold. Fritts's devices were very inefficient, transforming less than 1 percent of the absorbed light into electrical energy. The first modern solar cells were based on silicon and they came about in 1954 by Bell Laboratories. The first practical solar module with energy conversion efficiency was around 6 percent [2]. A year later, a 6% GaAs p-n junction solar cell was reported by RCA Lab in the U.S. [3]. In these years solar cells mainly found applications as power sources in space craft's.

The highlight for gaining more importance of solar cells as an alternative energy is the energy crisis and oil embargos of the 1970s. Photovoltaic was a subject of intense research during the 1980s. The main focus on PV research from the mid-1960s to the mid-1980s was to increase the efficiency of the product so that it produces more power. During the 1990s studies on photovoltaics expanded along with a growing awareness for alternative energy sources and as a result the PV production rate increased. Today the efficiency of solar cell has improved significantly and has reached over 20%. Currently, the overall goal is to produce low cost PV systems, low cost efficient solar cells and mounting hardware, power conditioning electronics, storage and tracking systems [4].

Silicon is the most important and dominating material in PV markets, particularly in its crystalline form. 85% of the solar cells for terrestrial applications are based on mono-crystalline (c-Si) and multi-crystalline silicon (mc-Si) wafer technology. The main reason for this is that silicon technology has already been highly developed and high-quality material is being produced in large quantities for the microelectronics and PV market [5]. Terrestrial solar cells are mainly p-n homo-junctions typically fabricated with solid-state diffusion method which requires high temperature (700-900 °C) furnace steps. They are also called "First generation" solar cells [6]. So far, the highest efficiency for mono-crystalline Si solar cells is  $(25.0 \pm 0.5\%)$  and for multi-crystalline Si is  $(20.0 \pm 0.5\%)$  at laboratory scale. The efficiencies of commercial cells are

( $22.9 \pm 0.6\%$ ) and ( $17.3 \pm 0.5\%$ ) for c-Si and mc-Si solar modules, respectively [7]. Although high efficiencies have been achieved for c-Si solar cells, the percentage of the converted energy is small compared to other energy sources. One of the main reasons for this is that monocrystalline solar cells have high production costs. These cells are generally fabricated on expensive high quality single crystal wafers and almost 50% of the c-Si module cost is due to the cost of high purity silicon wafer process [5].

Another problem regarding crystalline silicon solar cells has been the concern about the supply of high impurity silicon materials. Due to the increment in the demand for photovoltaic industry, high quality silicon materials have been tight and prices have been increasing. The high costs and shortage of pure silicon for PV applications stimulated research efforts on finding alternative PV materials and new fabrication processes.

The increment in the demand for photovoltaic modules has created a silicon supply shortage until very recently. This provided an opportunity for thin film photovoltaic modules to widely enter the PV market. Almost 15% of the PV market relies on thin film solar cells today. In thin film technology, a thin layer semiconductor material grows on a substrate, which is needed as a mechanical support, such as silicon wafer, glass and flexible plastic. Thin film solar cells use less material, and they are deposited on cheap substrates which makes it possible to reduce manufacturing costs. The thin film technology offers an alternative way to the reduction of high costs of the single crystalline and multi-crystalline based PV materials. The photovoltaic industry has been subject to extended research for around 25 years concerning the transition to “second generation” thin film solar cell technology due to their advantages over silicon based homo-junction solar cells. Another practical advantage of the thin film technology is the increase in the size of the manufacturing unit from ( $\sim 100 \text{ cm}^2$ ) in silicon wafer to ( $\sim 1 \text{ m}^2$ ), about 100 times larger in area, in the thin film technology [8]. The major requirements for good thin film materials are low costs, non-toxicity, robustness and stability. At present, major thin film technologies are a-Si/ $\mu\text{c-Si}$ , CdS/CdTe and CdS/CuInGaSe based solar cells. In the case of thin silicon film

technology, solar cells can be fabricated either in a single junction or multiple junction configurations. These solar cell types are reviewed below.

## **1.2.1 Thin Film Solar Cell Technologies**

### **1.2.1.1 Single-Junction Amorphous Silicon**

The first report on amorphous silicon solar cells was published in 1976 [9]. These solar cells were fabricated by plasma enhanced chemical vapor (PECVD) deposition at low temperature. Deposition with PECVD is based on the decomposition of silane ( $\text{SiH}_4$ ) gas in plasma created with DC, RF or other power sources. The amorphous silicon films typically contain about 5 to 20% of hydrogen and are represented as a-Si:H. The hydrogen leads to improvements in the quality of the properties of a-Si [10]. The H atoms passivate a large number of the defects resulting from the incomplete bonding of the Si atoms. Amorphous silicon solar cells have been used in commercial products such as calculators and digital watches since the early 1980s.

Amorphous p-i-n / n-i-p structure are the mostly used for a-Si:H solar cells. The silicon is deposited on glass, or plastic which has been coated with a layer of transparent conducting oxide (TCO). A nominally 100 nm thick p-type layer and a 20-30 nm thick n-type layer generate a field across the 100-400 nm intrinsic layers (for p-i-n). The intrinsic a-Si:H layer becomes the absorber in this configuration, with the collection of the generated carriers enabled by the externally generated field. The strength of a-Si technology is its simplicity in deposition by various techniques (PECVD, hot wire CVD, sputtering) and the abundance of silicon. The weakness of this material is its relatively low efficiency due to light induced degradation; the so-called Staebler–Wronski effect [11]. Today, research continues in finding ways to reduce this effect by minimizing light induced degradation problems which has stabilized the

highest confirmed efficiency for a single-junction a-Si:H cell at 10%. Module efficiencies are in the range of 6–8% [4].

### **1.2.1.2 Multi-junction Amorphous Silicon Solar Cells**

In order to minimize the light induced degradation effect in single junction amorphous silicon solar cells, two or more p-i-n and n-i-p cells are stacked on the top of one another. The ‘stack structure’ solar cells are called multi-junction or tandem cells. Stacking cells with different band gaps where the energy decreases from the top makes better use of the solar spectrum. In this case, each solar cell converts part of the solar spectrum at maximum efficiency. The first approach for multi-junction structure is based on a 3-cell stack with a-Si and a-Si alloyed with germanium (a-Si:H / a-SiGe:H / a-SiGe:H). The efficiency of (a-Si/SiGe) is in the range of 6–7% which is comparable to that of single junction a-Si cells [12]. Another Si based multi-junction structure is the micromorph (a-Si:H /micro-Si:H) tandem cells. This structure termed as “micromorph” has been developed by the University of Neuchatel in the 1990s. The large difference in the band gap values of these two semiconductors (about 1.0 eV. and 1.8 eV) leads to a better utilization of the solar spectrum and hence a higher solar cell efficiency. The highest stable efficiency confirmed as yet is 11.7%.

### **1.2.1.3 a-Si:H / c-Si Heterojunction**

a-Si:H/c-Si hetero-junction is a hybrid structure of crystalline silicon and amorphous silicon. In this structure thin doped amorphous layers are grown on a single crystalline or multi-crystalline wafer by various deposition methods at low temperatures. Process at low temperatures allows the use of lower quality Si wafers. This type of cell represents a combination of c-Si and a-Si:H technologies. The amorphous silicon has a large band gap (~1.8 eV) and its high absorption coefficient

enables to use the sun light efficiently. This dissertation is dedicated on the analysis of a-Si:H/c-Si heterojunction fabricated by PECVD and sputtering techniques. In the next section the reader can find detailed information about this kind of solar cells through the description of their physics, historical development and the presentation of the relevant literature survey.

#### **1.2.1.4 Compound Semiconductors**

Compound semiconductors have greatly extended the range of available materials while II-VI binary compounds and I-III-VI ternary compounds (chalcogenide compounds) have been used for thin film photovoltaic's semiconductor. At present, cadmium telluride (CdTe), copper indium diselenide (CuInSe<sub>2</sub>), copper gallium indium diselenide (CuGaInSe<sub>2</sub>) and its related alloys are the mostly studied PV materials. The band gap of CdTe is approximately 1.45 eV, which is nearly ideal for absorbing the maximum amount of the solar spectrum. The band gap allows for a high absorption coefficient making approximately a few  $\mu\text{m}$  thick CdTe layers possible. CdTe modules on glass have obtained 11% efficiency [8]. The efficiencies of CGIS cells are around 20% with the area of 0.5 cm<sup>2</sup> on glass substrates, which is comparable to multi-crystalline Si wafer efficiency values [13]. Another fascinating solar cell type is based on multijunction (usually triple junction) cells fabricated using GaAs based compound semiconductor. GaInP/InGaAs/Ge stacked structure achieved in a world record for terrestrial concentrator solar cell efficiency at 41.6% [14] while another multifunction has the efficiency of 42.3% [15]. Figure 1.2-1 illustrates the best laboratory (small scale) PV efficiencies obtained for various materials and technologies. Commercial efficiencies can be lower than laboratory results.

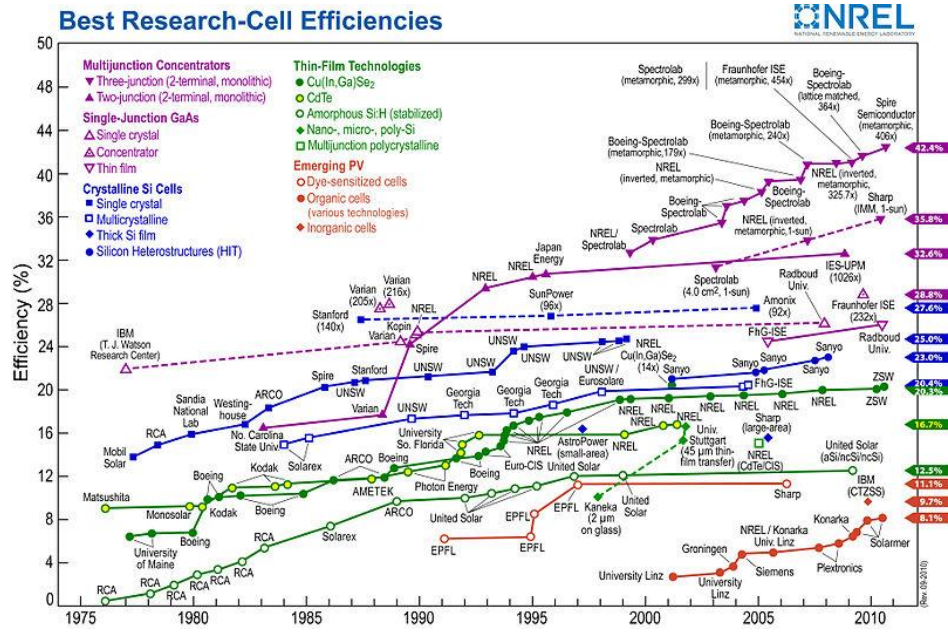


Figure 1.2-1: Best research solar cell efficiencies reported by NREL [16].

### 1.3 a-Si:H / c-Si Heterojunction

Today the PV market is one of the most rapidly growing industries due to the benefits mentioned in the section 1.1. However, the total electricity generated by PV systems is still small compared to fossil fuels. The main goal for the PV industry is the increase share of solar modules worldwide. Decreasing PV production costs is a key factor in enhancing the use of solar energy. Additionally, countries have some form of energy policies to support the use of solar energy, which compensates the higher production cost of PV modules. The technical requirements for decreasing the production cost of PVs can be listed as follows:

- Thin wafers.

The reduction of wafer thickness while improving the optoelectronic properties and stability of the material. The idea in reducing the thickness is using fewer materials to

form solar cells. However, current conventional crystalline technology requires high temperature furnace based processes which is not suitable for thin materials.

- Using less expensive materials.

Silicon based materials such as solar-grade Czochralski (CZ) Si and cast polycrystalline silicon (poly-Si) are not expensive as high purity mono silicon wafers. However, less expensive materials tend to be of lower quality with high impurity and crystal defects. Hence, they are not suitable for conventional diffusion processes because of the degradation in the bulk property caused by high-temperature cycling.

- Increasing the speed and simplicity of the processing steps.

Simplifying the technology leads to use less energy to produce large area devices in shorter time [17]. One of the promising solutions for these problems is the hydrogenated amorphous silicon crystalline heterojunction (a-Si:H/c-Si) (SHJ) solar cells. SHJ is the combination of c-Si wafer and amorphous thin film technology. The heterojunction is formed by the deposition of wide band gap a-Si:H doped layers on c-Si wafers at relatively low temperatures (<250 °C). Fabrication at low temperature assists preservation of the minority-carrier lifetime in contrast to the standard c-Si solar cell process at high temperature.

Figure 1.3-1 shows the typical structure of a p type SHJ. In this structure the absorber (base) is the c-Si (p) wafer. The emitter (window) is a doped a-Si:H(n) layer with a wide band gap (~1.8 eV) and light comes from the emitter side. The p-n junction is formed by depositing a-Si:H(n) layers on the c-Si(p) wafer. Transparent conductive oxide (TCO) layers, also working as an anti-reflection (AR) layer, are needed on the a-Si:H(n) layer due to low conductivity of the amorphous film. The Ni-Al grids are deposited on the top of TCO to collect the carriers. On the bottom of the wafer, the back-surface field (BSF) structure is applied with deposited a-Si:H(p) layers. At the back surface, an aluminum layer is used as the back contact.

The doped a-Si:H layer has a large density of defects in the form of dangling bonds. Dangling bonds create localized states throughout the band region. The

introduced intrinsic buffer layers between the doped a-Si:H layers and the c-Si wafer act as a passivation layer which leads to higher  $V_{oc}$ . This type of structure named as Heterojunction with Intrinsic Thin (HIT) solar cells was invented by Sanyo Electric Co., Ltd.

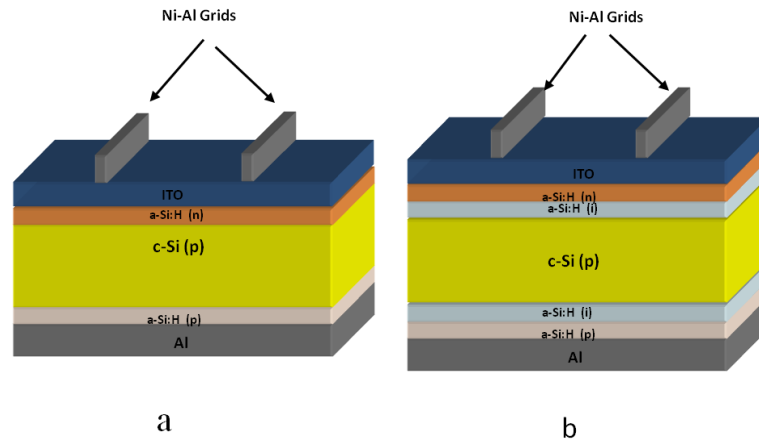


Figure 1.3-1: Illustration of p-type SHJ (a) and HIT (b) cell structures.

SHJ solar cells were first proposed by Fuhs et al. in 1974 [18]. Their cells were manufactured by using undoped hydrogenated amorphous silicon on Czochralski grown crystalline substrate by plasma enhanced chemical vapor deposition (PECVD) method. In 1975, the substitutional doping of amorphous silicon was achieved to form heterojunction by applying PECVD [19]. In the late eighties a Japanese company, Sanyo Ltd., developed high efficiency a-Si:H(p) /c-Si(n) heterojunction for efficiencies at about 12 %. However, the biggest success occurred in 1992, which also made SHJ cells more popular. In this year, SANYO presented a new type of a-Si:H/c-Si heterojunction solar cell having an a-Si:H(p) layer on c-Si(n) wafer with additionally a thin intrinsic (undoped) amorphous silicon interface layer and an a-Si:H(n) back passivation layer; namely the HIT (heterojunction with intrinsic thin layer) solar cell. The first publications on HIT cells reported an efficiency of 18.7% [20]. In the following years a continuous progress has been seen regarding the conversion efficiency of the HIT solar cell. According to Sanyo's 2001 report, the company has

reached their world's highest efficiency of 23.0% for a large area (100 cm<sup>2</sup>) HIT solar cell with a high open circuit voltage ( $V_{oc}$ ) of 720 mV [21].

The success of HIT cells has attracted much attention by many research groups and businesses. Several companies, laboratories and research groups, particularly in Europe, have been working on physical properties of the heterojunction and the development of c-Si wafer based SHJ solar cells.

The Hahn-Meitner-Institute (Berlin) studied the a-Si:H/c-Si band offset, determination of a-Si:H Fermi level and density distribution of defect states within doped and intrinsic a-Si:H layers on c-Si [22]. For these purposes they applied X-ray photo spectroscopy (XPS), ultra-violet photo spectroscopy (UPS) and ultraviolet-excited photoelectron yield spectroscopy (UV-PYS) measurements. This group has noticed that the density of defect states in doped a-Si:H are higher than those in intrinsic a-Si:H and the incensement in defect states are responsible for the recombination at the a-Si:H/c-Si interface which causes low open  $V_{oc}$  [23], [24]. Fujiwara et al. studied the growth process and structure of a-Si:H layer by using real-time spectroscopic ellipsometry (SE), and they also investigated the effect of the thickness of a-Si:H layer on the solar cell performance [25].

Plasma enhanced chemical vapor deposition (PECVD), hot-wire CVD (HWCVD) and very-high-frequency PECVD (VHF-PECVD) are the common techniques for the production of SHJ and HIT solar cells. So far, no group has repeated Sanyo's solar cell performance in terms of high  $V_{oc}$  and high efficiency. It is therefore clear that further investigation on the HIT and SHJ devices is needed. Only two groups have reached efficiency beyond 19% Helmholtz Zentrum Berlin on n -type wafers [26] by PECVD and the National Renewable Energy Laboratory (NREL-USA) on p-type wafers by HWCVD [27]. Although Wang achieved high efficiencies by HWCVD this techniques is not applicable for large scale production. Jagannathan et.al used sputtering method for fabrication of SHJ cells. They achieved ~10% efficiency with the  $V_{oc}$  of 550 mV [28]. However, there are not enough studies in the literature for SHJ fabrication through sputtering techniques. Due to its low efficiency and difficulty for large processes, sputtering cannot compete with the PECVD method.

Today, p-type crystalline silicon wafers are leading the production of solar cells. On the other hand, n-type silicon wafers have an advantage over the standard p-type wafers in terms of recombination lifetimes. Sanyo and SunPower Inc. have achieved efficiencies of over 20% on large-scale n-type Czochralski and float-zone wafers which proposes a potential for using n-type silicon wafers as a basis for commercial solar cells. Although promising potential of n-type wafers, p-type silicon wafers are dominant in the PV market.

One reason for the dominance of p-type wafers is the commercial diffused technological simplicity of the phosphorus diffusion process for the n<sup>+</sup> emitter formation applied today in most solar cell production lines.

The other reason is historical. The early usage of solar cells was mainly for space power applications. It is observed that the lifetime of space vehicle's power last longer with the p-type Si cells than the ones had n-type Si solar cells. It is mainly due to significant degradation of n type cells due to irradiation in space. As a result of the superior performance of p-type Si solar cells, photovoltaic market has been developed on the basis of the p-type solar cells.

Another reason for the dominance of p-type silicon wafers in the PV market is mobility of the minority carriers. Electrons have higher mobility and longer diffusion length than holes. Diffusion length of minority carriers has a significant influence in the light-generated current which leads to a preference toward p-type silicon wafers [29].

However, lifetimes measured on p-type Si wafers are typically one to two orders of magnitude below those of n-type Si wafers. The minority carrier lifetime is strongly affected by various defect-impurity mechanisms such as hydrogen-oxygen (H-O) centers, boron-oxygen (B-O) complexes. Boron doped p type wafers have smaller life time than n type wafers, due to the formation of B-O complexes which are not observed in the phosphorus-doped n type wafers [30]. Although p-type silicon is more common in the PV market, SHJ cells on p-type c-Si have not reached the same efficiencies as n type SHJ cells. Nevertheless, several groups achieved encouraging values of  $V_{oc}$  and FF with SHJ cells based on p-type c-Si. Achieving high p type SHJ cell performance is

also another challenge in the research area. Table summarizes the best  $V_{oc}$  and efficiency values of SHJ solar cells on p- and n-type c-Si.

Table 1: The best  $V_{oc}$  and efficiency values of SHJ solar cells on p- and n-type c-Si by several groups [22].

| Groups                   | n type       |        | p type       |        |
|--------------------------|--------------|--------|--------------|--------|
|                          | $V_{oc}(mV)$ | Eff(%) | $V_{oc}(mV)$ | Eff(%) |
| <b>Sanyo</b>             | 739          | 23     |              |        |
| <b>HMI</b>               | 660          | 19.8   | 639          | 17.4   |
| <b>NREL</b>              | 694          | 18.2   | 693          | 19.2   |
| <b>IEC</b>               | 694          | 18.4   |              |        |
| <b>Uni. of Neuchatel</b> | 713          | 18.4   |              |        |
| <b>ENEA</b>              |              |        | 601          | 17     |
| <b>Utrecht Univ.</b>     | 610          | 15.8   | 595          | 14.9   |
| <b>AIST</b>              |              |        |              |        |
| <b>Uni. of Stuttgart</b> |              |        | 655          | 14.1   |
| <b>CAS</b>               |              |        | 582          | 14.02  |
| <b>CNR-IMM</b>           | 638          | 14     | 579          | 13.31  |

## 1.4 Thesis Statement

This dissertation presents an electrical and optical characterization of a-Si:H(n)/c-Si(p) heterojunction solar cells. The primary goal of this thesis is to identify and understand the efficiency limiting mechanisms and device physics of a-Si:H(n)/c-Si(p) solar cells operation (with and without i-layer) under different deposition parameters. Particularly we focused on depositing good quality a-Si:H(n) emitter layers for high efficiency SHJ (p) solar cells with a-Si:H(p)/Al BSF at low temperatures. The relation between deposition parameters and a-Si:H film properties was investigated. Various electrical and optical characterization techniques were used to obtain information about the thin a-Si:H films and a-Si:H(n)/c-Si(p) cells such as: current density voltage (J-V), quantum efficiency, transmission and reflection, FTIR, Raman, minority carrier life time and conductivity measurements. Optimization of

laboratory cells was undertaken, i.e. passivating intrinsic buffer layer, interfaces between intrinsic and doped layers, interfaces between silicon and ITO. We believed that this study will be a good base for the future studies at the Center for Solar Energy Research and Applications (GÜNAM) - Turkey.

In this study, heterojunction solar cells were fabricated by two different deposition techniques: magnetron sputtering and PECVD. In the first stage a-Si:H(n)/c-Si(p) cells were fabricated by magnetron sputtering. Fabrication, characterization and all analysis for these cells were held at METU Physics Department. In the second stage of this thesis, PECVD method was used to fabricate the a-Si:H(n)/c-Si(p) solar cells. All PECVD processing and characterization steps for solar cells were performed at the University of Delaware-Institute of Energy Conversion (IEC).

## **1.5 Thesis Outline**

This thesis is mainly focused on the fabrication of n type hydrogenated amorphous silicon/p type crystalline silicon, a-Si:H(n)/c-Si(p), solar cells via sputtering and Plasma Enhanced Chemical Vapor Deposition (PECVD) techniques. Both techniques lead the deposition of good quality a-Si:H at relatively low substrate temperatures. In this thesis a reader can find investigation of the structural, electrical and optical properties of a-Si:H(n) films and the photovoltaic performance of a-Si:H(n)/c-Si(p) solar cells deposited by means of two different techniques. An overview on the contents of each chapter is described below.

The Chapter 1 is an introduction to photovoltaics and solar cells. General information is given about current status of photovoltaics and thin film technologies. A literature survey is presented in this chapter.

The second chapter covers a-Si:H(n)/c-Si(p) heterojunction fundamentals. It deals with physics of p-n junctions, the heterojunction solar cell operation principles and the recombination mechanism in solar cells.

Chapter 3 describes the fabrication and characterization techniques.

In Chapter 4 the properties of a-Si:H layers deposited by sputtering for application in solar cells are presented. Analysis of a-Si:H(n)/c-Si(p) solar cells deposited via sputtering method is also represented in this chapter.

Chapter 5 is dedicated to analysis of a-Si:H(n)/c-Si (p) solar cells fabricated by PECVD method. The investigation deposition effects such as temperature, doping gas and hydrogen flow, DC power on the solar cell performances are summarized. J-V curve analysis and QE measurements results as shown to gain information about the cells in detail. The effort in improving solar cell performances is discussed as well.

In Chapter 6 a-Si:H(n)/c-Si(p) solar cells structures with intrinsic buffer layer is discussed. As previous chapter all layers are fabricated by PECVD. Including buffer layer improves the passivation quality and hence  $V_{oc}$ . Deposition temperature and hydrogen flow effects on a-Si:H(i) is investigated.

In the conclusion part, Chapter 7 is a summary of the work done for this thesis. The solar cells performances are compared between two deposition techniques.

## CHAPTER 2

### **a-Si:H/ c-Si HETEROJUNCTION MODEL**

In this chapter the fundamentals of heterojunction model and basic operation mechanism of p-n junction solar cells are briefly described.

#### **2.1 Heterojunction Fundamentals**

Homojunction is the basic junction which is formed by n and p type of the same semiconductor material. For homojunctions the dominant transport mechanism is diffusion of charge carriers in the neutral bulk which is expressed by Shockley diode law [31]. Besides diffusion of carriers, another model was formulated by Sah. et al. includes the consideration of recombination in the space charge region [32]. Heterojunction is a p-n junction formed between two different semiconductor materials. Charge carrier transport in the p-n heterojunction can be unique and complicated than the basic p-n homojunction.

p-n heterojunction has the band discontinuities, shown in Figure 2.1-1, acting as barriers for the flow of charge carriers. Existence of barriers and defect states in the bulk and at the interface make the charge carrier transport (current flow) mechanism more complicated than a simple p-n homojunction. Various models have been developed to clarify the current flow in semiconductor heterojunction. Among them, the Anderson model is the fundamental model for understanding the heterojunction mechanism. This model, first described for Ge-GaAs hetero-structure, considers the current flow in a heterojunction by injection of carriers over the conduction or valance band barriers [33]. On the other hand, in real case current flow in heterojunction is not only injection but also a sum of injection, tunneling and interface recombination

components. Nevertheless, the Anderson model is accepted as a starting point for heterojunction transport theories. The energy band diagram of the heterojunction is considered by first drawing the energy band diagrams of two isolated different semiconductors separately and aligning them using the same vacuum level as shown in Figure 2.1-1

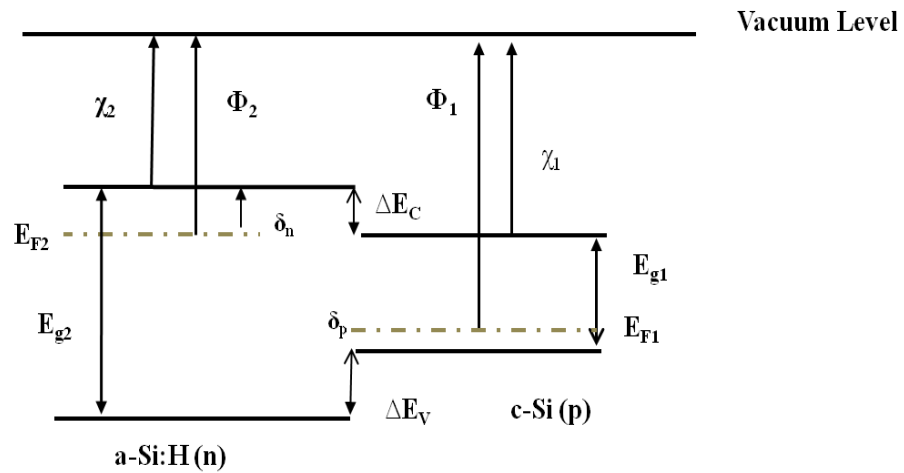


Figure 2.1-1: Band lines of two isolated distinct semiconductors.

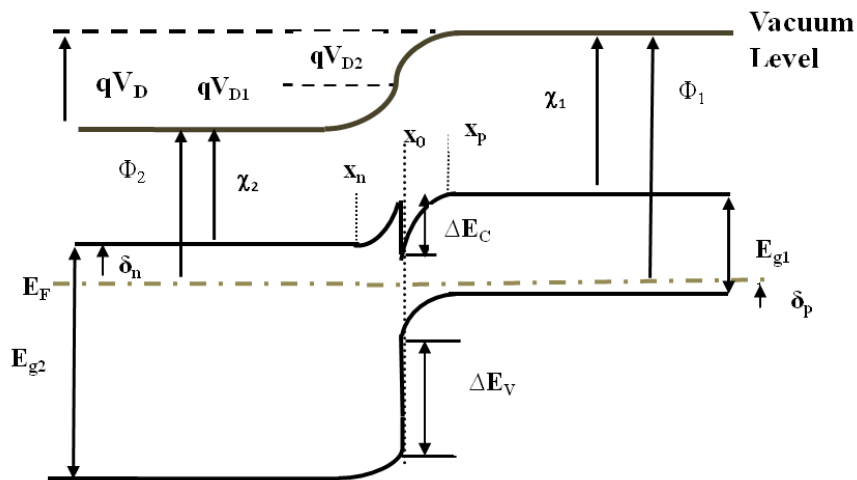


Figure 2.1-2: Band diagram of a heterojunction at equilibrium formed between two semiconductors.

The semiconductors in Figure 2.1-1 have different band gaps,  $E_g$ , different dielectric constants,  $\epsilon$ , different work functions,  $\phi$ , and different electron affinities,  $\chi$ . In

Figure 2.1-1 and Figure 2.1-2 the subscripts 1 and 2 refer to c-Si(p) and a-Si:H(n), respectively.  $\Delta E_C$  and  $\Delta E_V$  represent the discontinuities in the conduction band and valance band, respectively.

When two semiconductors are brought together, Fermi levels must accomplish at the same energy level by electron transfers between the semiconductors. This results in a partial depletion of electrons near the junction in semiconductor2 and therefore a bending upward of the band edges. There is also redistribution of charge in semiconductor1 and bending down of the band edges. At equilibrium the band edges and Fermi levels line up as shown in Figure 2.1-2. In Figure 2.1-2, the electrostatic potential difference between any two semiconductors can be represented by the vertical displacement of the band edges. The discontinuities in the band diagram of the junction affect the transport and recombination of charge carriers and therefore the electronic behavior of the solar cell. The relationships between discontinuities and important quantities in the heterojunction are defined by equations below.

$$\begin{aligned}\Delta E_c &= (Ec_2 - Ec_1) \\ \Delta E_c &= (\chi_1 - \chi_2)q\end{aligned}\tag{2.1}$$

$$\begin{aligned}\Delta E_V &= (E_{V2} - E_{V1}) \\ \Delta E_V &= (\chi_2 - \chi_1)q + E_{g2} - E_{g1}\end{aligned}\tag{2.2}$$

$V_{D1}$  and  $V_{D2}$  in the Figure 2.1-1 are the electrostatic potentials supported at the equilibrium by semiconductors. The band bending  $V_D$ , built-in potential, is assigned by is sum of the  $V_{D1}$  and  $V_{D2}$ .

$$qV_D = qV_{D1} + qV_{D2} = E_{g1} - \delta_n - \delta_p + \Delta E_c\tag{2.3}$$

$V$  is the applied bias and  $V_1$ ,  $V_2$  are the portions of applied voltage drop on either side of the junction.

$$V = V_1 + V_2 \quad (2.4)$$

$$\left( \frac{V_{D2} - V_2}{V_{D1} - V_1} \right) = \left( \frac{N_{A1} \cdot \epsilon_{s1}}{N_{A2} \cdot \epsilon_{s2}} \right) \quad (2.5)$$

Where  $N_A$  ( $N_D$ ) is acceptor (donor) concentration and  $\epsilon$  is the dielectric constant of semiconductors. With further algebraic manipulations the depletion widths on either side of the junction can be defined by Eq. (2.6) and Eq. (2.7).

$$W_p^2 = (x_0 - x_p)^2 = \frac{2\epsilon_{s1}\epsilon_{s2}(V_D - V)N_{D2}}{[qN_{A1}(\epsilon_{s1}N_{A1} + \epsilon_{s2}N_{D2})]} \quad (2.6)$$

$$W_n^2 = (x_n - x_0)^2 = \frac{2\epsilon_{s1}\epsilon_{s2}(V_D - V)N_{A1}}{[qN_{D2}(\epsilon_{s1}N_{A1} + \epsilon_{s2}N_{D2})]} \quad (2.7)$$

The diffusion current is defined by Eq. (2.8) which is similar to p-n homojunction derived from the Shockley diode assumption. The electron and hole diffusion currents are presented in Eq. (2.8) and Eq. (2.9).

$$J_n = q \frac{D_n}{L_n} \left( \frac{n_i^2}{N_A} \right) \left[ \exp\left( \frac{qV}{kT} \right) - 1 \right] \quad (2.8)$$

$$J_p = q \frac{D_p}{L_p} \left( \frac{n_i^2}{N_D} \right) \left[ \exp\left( \frac{qV}{kT} \right) - 1 \right] \quad (2.9)$$

$$J = J_p + J_n \quad (2.10)$$

Where  $D_n$  and  $D_p$  are diffusion constants for electrons and holes, respectively.  $L_n$  and  $L_p$  is the diffusion length of electrons and holes respectively [34].

Anderson heterojunction model is mainly based on the Shockley model which assumes that the dominant transport mechanism is the charge carrier diffusion [35]. The

disadvantage of Anderson model is the exclusion of the role of tunneling and other mechanism such as interface recombination in heterojunction. The recombination current predicted by the Anderson model is typically several magnitudes lower than that observed experimentally in typical heterojunctions. Therefore the Anderson model is not fully sufficient to explain carrier transport in p-n heterojunction. With certain modifications to the Anderson model, different heterojunction charge carrier transport models including recombination and tunneling mechanisms have been proposed. Figure 2.1-3 displays possible charge carrier transport paths in a p-n heterojunction. In Figure 2.1-3 both electron and hole current are shown but in real case one (electron or hole current) is dominant.

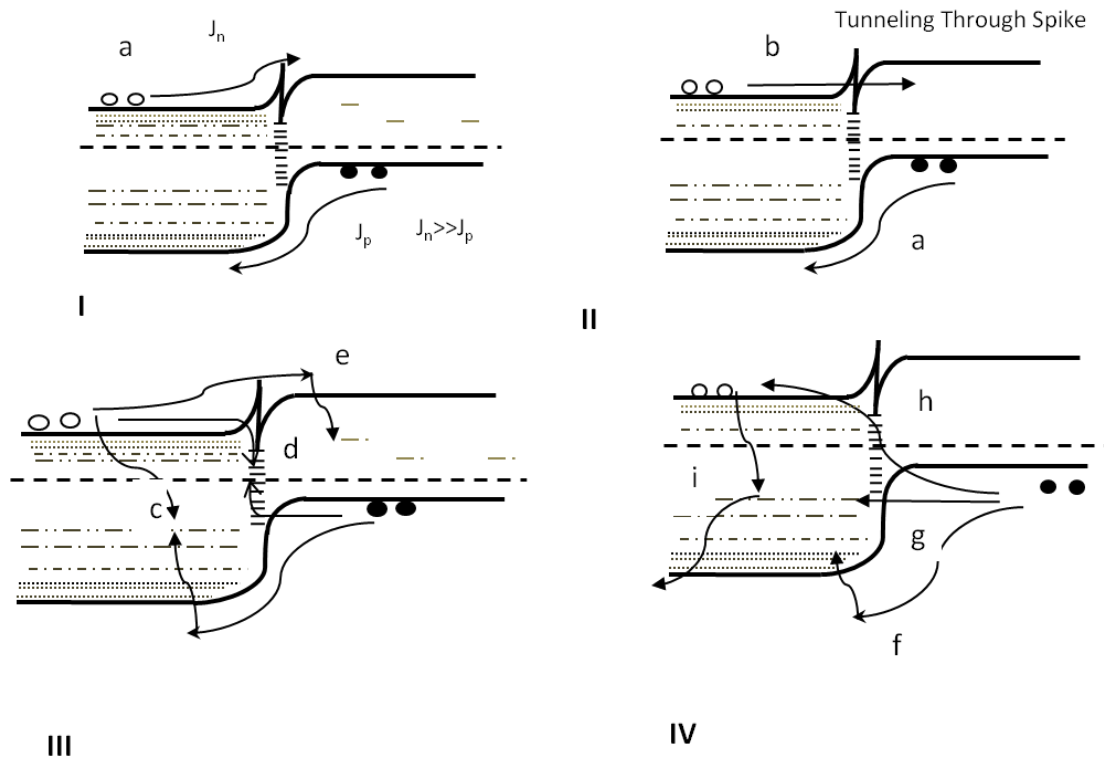


Figure 2.1-3: Equilibrium band line-up of a a-Si:H(n)/c-Si(p) heterojunction and possible transport paths for moderate forward bias [35].

Path (a) has emission or diffusion of currents flowing over the barriers at the heterojunction. This may be accompanied by some depletion region space-charge

recombination. This is basically the model proposed by Anderson. Path (b) shows the tunneling through spike.

The paths showed in III and IV of Figure 2.1-3 display possible recombination and tunneling mechanism, respectively.

Path (c), (d) and (e) represent the recombination via a-Si:H gap states, via interface states and recombination through deep defects states in c-Si, respectively.

Path (h) shows the band-to-band multi-tunneling process. Tunneling into interface states and successive recombination is displayed in Path (g). Path (f) represents tunnel hopping on the a-Si:H band tail. Path (i) shows multi-tunneling in the a-Si:H with successive recombination through carrier capture or reemission into the band.

As a result of Figure 2.1-3 several transport models are in principle applicable to the device structure. There is no single model accounting all possible transport paths. Analyzing the J-V curve with temperature dependence can give some information about the dominant transport mechanism with comparing their functional form. The dark current density can be written by a general diode expression for all transport mechanism as in Eq. (2.11).

$$J = J_0 \left[ \exp \left( \frac{q(V - JR_s)}{nkT} \right) - 1 \right] - \left( \frac{V - JR_s}{R_{SH}} \right) \quad (2.11)$$

Where  $J_0$  is saturation current density,  $R_s$  and  $R_{SH}$  are the series and shunt resistance and  $q$ ,  $n$ ,  $k$ ,  $T$  are electron charge, diode ideality factor, Boltzmann's constant and measurement temperature, respectively. Because  $R_{SH}$  is larger than  $R_s$  the second term in Eq. (2.11) is neglected. When the first term of Eq. (2.11) is plotted with semi-logarithmic scale for voltage, four different regions can be distinguished as indicated on Figure 2.1-4.

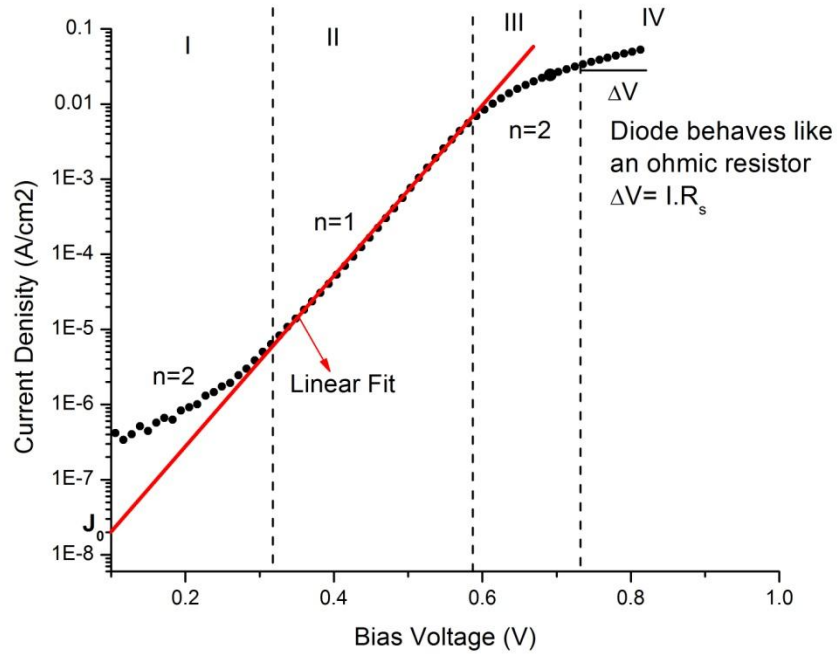


Figure 2.1-4: A Ln(J)-V graph. At low biases, the recombination effects in depletion region are dominant. At higher biases the slope becomes closer to unity. At highest bias the behavior becomes more ohmic.

Here, region I is the non-linear region due to the recombination effects in depletion region at low voltages; region II is the linear region and represents the ideal diode behavior, region III is the high injection level which occurs rarely and region IV shows the ohmic behavior of diode and the current is limited by the series resistance. In the region III,  $R_s$  is negligible (ideal diode behavior), in high voltage region the series resistance becomes important. And the Eq. (2.11) becomes:

$$J = J_0 \left[ \exp\left(\frac{qV}{nkT}\right) - 1 \right] \quad (2.12)$$

The  $R_s$  ( $\Omega \cdot \text{cm}^2$ ) can be deduced from deviation of the Ln(J)-V curve. In the high voltage region diode behaves like an ohmic resistor and  $R_s = \Delta V / J$  [36]. To evaluate the charge carrier transport mechanism Ln(J)-V graph is fitted to the general diode

equation. From the slope and intercept of the linear region of the semi-logarithmic plot of current density-voltage measurement plots  $n$  and  $J_0$  values were obtained depending on the Eq. (2.13).

$$\ln J = \ln J_0 + \frac{qV}{nkT} \quad (2.13)$$

After obtaining saturation current for each temperature, the activation energy ( $E_a$ ) can be found by plotting  $\ln(J_0)$  vs  $(-1/T)$  graph with regarding the Eq. (2.14).

$$J_0 = J_{00} \left[ \exp\left(\frac{-E_a}{kT}\right) \right] \quad (2.14)$$

Here,  $J_{00}$  is the saturation current pre-factor.

Analyzing temperature dependence of  $J_0$ ,  $n$  and  $E_a$  values the carrier transportation mechanism can be elucidated using the functional form of the transportation models [35].

In Chapter 6 reader can find an example for the temperature dependence J-V curve analysis. In depth discussion of these heterojunction transport models is beyond the scope of this study. The detailed analysis on transport models can be found in the mentioned references in this section.

## 2.2 Solar Cell Principles in p-n Homojunction

This section starts with a brief discussion of conventional basic p-n homojunction solar cells action. The differences for heterojunction solar cells are explained in the following section.

The operation of the p-n junction solar cell starts with generation of electron-hole pairs by sun light absorption. When the absorbed light energy is equal or greater than the band gap energy of semiconductor the electron excites from valance band to conduction band leaving a hole in the valance band. Due to electron-hole pair

generation the energy equilibrium is disturbed on both p and n sides of the junction. Therefore the Fermi level splits into two quasi Fermi levels: an electron quasi Fermi level,  $E_{FN}$ , and a hole quasi Fermi level,  $E_{FP}$ . The electron-hole pair is also called photo-generated carriers. The second step is the diffusion of the photo-generated carriers to the edge of the depletion region of the p-n junction before they recombine. If the carrier recombines before reaching the depletion region, then the light-generated electron-hole pair is lost and no current can be generated. The photo-generated carriers reached to the depletion region are separated by the built-in electric field. Under the influence of this built-in electric field in the depletion region, the photo-excited carriers are driven in opposite directions: electrons towards the n-type region and holes towards the p-type region. Transportation of the carriers and collection of electrical charges via ohmic contacts and grids on the opposite sides of a cell leads to the appearance of the photo voltage;  $V_p$ . When total current is zero the  $V_p=V_{oc}$ . The flow of photo generated carriers leads a photocurrent and the separation of photo generated carriers cause a voltage in the solar cell. Figure 2.2-1 shows the energy band diagram of the p-n homojunction solar cell at equilibrium and under light illumination.

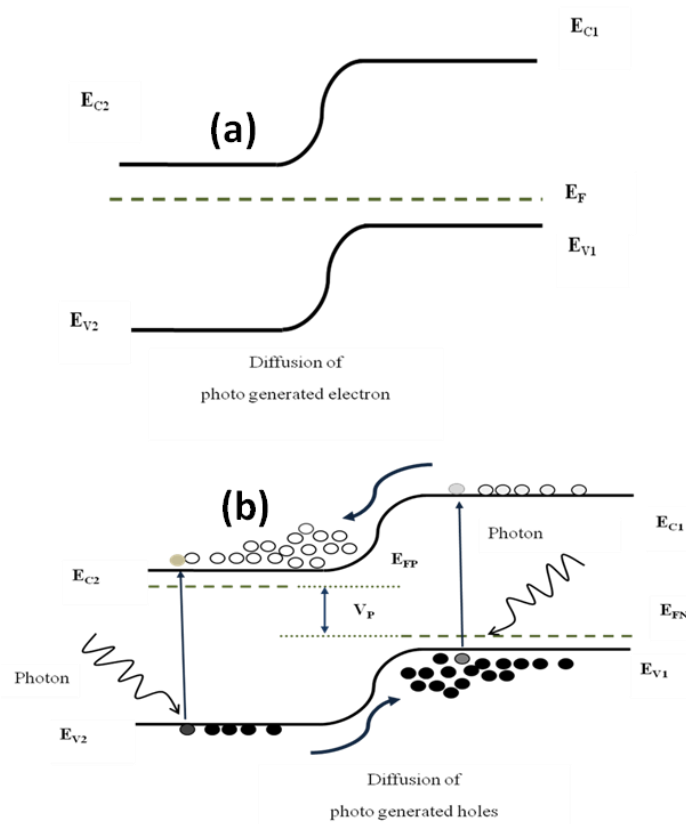


Figure 2.2-1: The energy band profiles (a) of a p-n diode (solar cell) in the equilibrium (b) under illumination.

The current density under illumination for a simple model of a p-n homojunction solar cell is given by Eq. (2.15) without considering series ( $R_s$ ) and shunt resistances ( $R_{sh}$ ).

$$J = J_0 \left[ \exp\left(\frac{qV}{nkT}\right) - 1 \right] - J_L \quad (2.15)$$

Where  $J_0$  is the Shockley model leakage current of the diode without illumination and  $J_L$  is the maximum current density that corresponds to the illumination. The open circuit voltage is obtained from Eq. (2.15) by setting the  $J$  equal to zero.  $V_{oc}$  becomes as:

$$V_{oc} = \frac{nkT}{q} \ln \left\{ \left( \frac{J_L}{J_0} \right) + 1 \right\} \quad (2.16)$$

## 2.3 p-n Heterojunction Solar Cells

Carrier transportation in the amorphous/crystalline Si heterojunction can be unique and has differences from the simple p–n homojunction [22]. The essential difference between homojunction and heterojunction is potential barriers (or band offsets) at the valance band of the p-n heterojunction (in that configuration p side is c-Si(p) and n side is a-Si:H(n) film). High potential barriers in the valance band prevents holes from moving from p type c-Si to a-Si:H(n) layer side. The barrier in the conduction band is smaller than the barrier in the valance band and hence electrons can transport toward n side of the heterojunction (Figure 2.3-1). Therefore, hole flow from c-Si(p) to a-Si:H(n) is negligible relative to electron flow from n side to p side of the heterojunction.

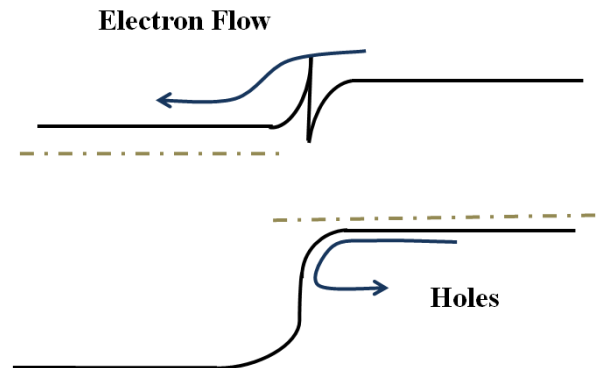


Figure 2.3-1: High potential barrier in the valance band prevents holes from p side to n side. As the potential barrier in conduction band is smaller than the barrier in the valance band, electrons can transport toward to n side of the heterojunction.

In heterojunction solar cells the emitter layer has wider band gap (1.6-2.0 eV) and this enhances the response in the blue area of solar spectra (window effect). Wide-gap window effect allows using the absorbed light efficiently and effects create a band pass region of sensitivity to photons of energy between two semiconductor's band gaps. This is shown in Figure 2.3-2.

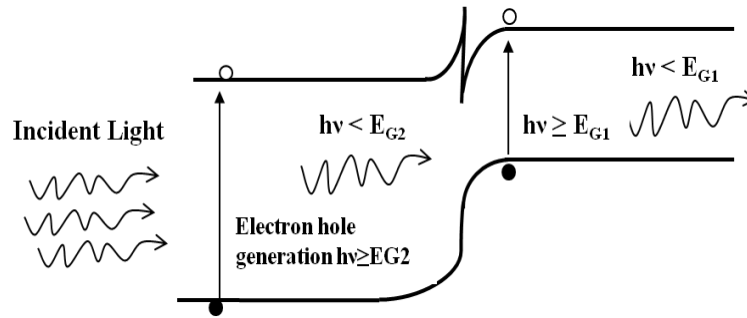


Figure 2.3-2: Schematic showing of photon absorption and window effect of emitter.

To obtain high efficiencies, the design of SHJ requires considering the way to reduce the band offset blocking the minority carriers flow. Yablonovitch et al. suggest that the ideal solar cell should be built in the form of a double hetero-structure. In this structure a narrower band gap active material is sandwiched between two wider band gap layers of opposite doping [37]. The SHJ structure studied in this thesis is Al-Ni grids / ITO / a-Si:H (n) / c-Si (p) / a-Si:H (p) / Al. In this configuration a-Si:H(p)/Al stack is used to create back surface field (BSF) for c-Si (p). This is an alternative way for the diffused Al-BSF which requires high-temperature ( $\sim 850$  °C) processing. High temperature causes degradation of lower grade Si wafers. Additionally, in the case of diffused Al-BSF, the efficiency reduces because of decreasing light response at longer wave lengths resulted from poor back-surface passivation [38]. The main advantage to use a-Si:H(p)/Al BSF is depositing at low processing temperatures ( $\sim 200$  °C). Additionally, larger conduction band offset could provide a much more effective mirror for the minority carrier electrons and a low back surface recombination as shown in Figure 2.3-3. This configuration leads to higher solar cell performance [39].

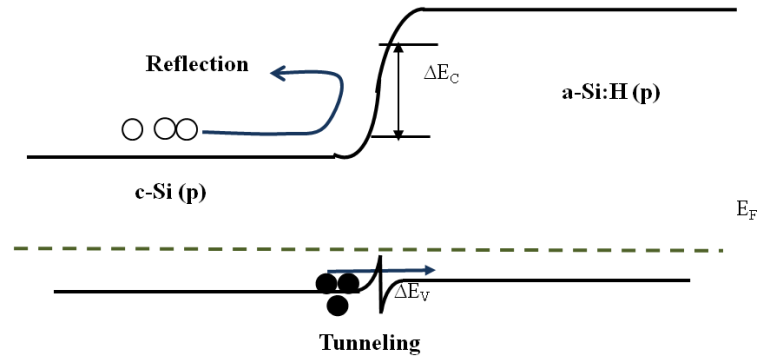


Figure 2.3-3: Band diagram of a-Si:H(p) back-surface field for SHJ solar cell on p-type c-Si substrates. BSF created by p type doped a-Si:H keeps minority carriers away from high recombination surface.

The key point for the performance of a heterojunction cell is minimizing the densities of interface defect states ( $D_{it}$ ). In HIT structure intrinsic a-Si:H is applied on both sides of c-Si(p) to passivate the interface defects. With the intrinsic a-Si:H layer the hetero interface is separated from the doped layer, so that these defects caused by the doping materials can be avoided [40].

The heterojunction band offsets to a p-type c-Si based HIT cell with an a-Si:H (n/i) emitter on the front surface and with a-Si:H (i/p) as the BSF contact on the back surface is shown in Figure 2.3-4. At the front junction the minority electron flow is resulted by a small barrier created by the conduction band offset. In order to collect generated carriers efficiently in p type SHJ, the emitter a-Si:H (n/i) should have low barrier at the conduction band for minority carriers and a-Si:H (i/p) back layer should have a large one in the valence band.

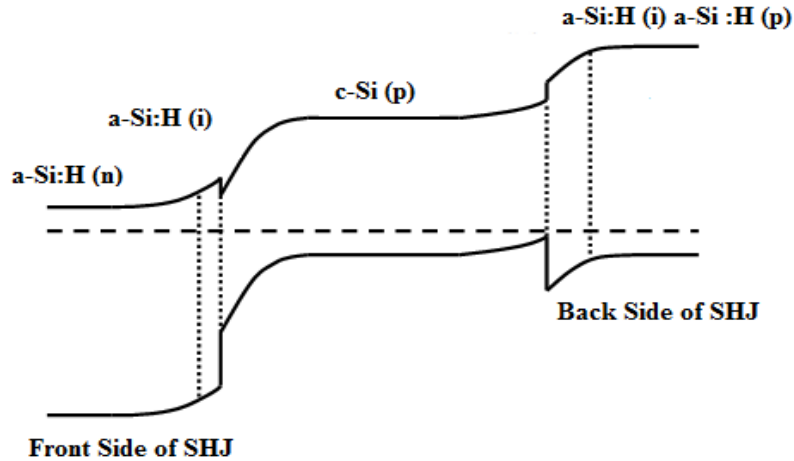


Figure 2.3-4: Schematic band diagram of HIT structure on p-type c-Si [41].

## 2.4 Losses in Heterojunction Solar Cells SRH Recombination

The solar cell process begins with the generation of photocurrent. Photo generated charge carriers that either recombine in the semiconductors bulk or at its surface cause a decrease the solar cells performances. Therefore, one of the major parameters for a-Si:H/c-Si solar cells is the generation and recombination of free charge carriers. Generation is an electronic excitation process which increases the free charge carrier in the conduction band of the semiconductor. Generation requires external energy for free charge carriers. In the solar cell action, the generation of electron hole pair occurs due to absorption of photons whose energy is greater than band gap of the semiconductor. The flow of these free charge carriers leads to a current named as photo-generated current or photocurrent. Recombination on the other hand, is the opposite process of generation i.e. loss of electron or hole though the decay of an electron in the conduction band to a lower energy state in valance band. Recombination can be from band to band annihilated electron hole pair, or it can be from conduction band to a trap state or from a trap state to valance band. Recombination mechanism can be classified as two groups: Intrinsic (unavoidable) recombination and extrinsic (avoidable) recombination.

Intrinsic (unavoidable) recombination is due to the essentially physical processes in the intrinsic material. Radiative recombination and Auger recombination are intrinsic type. In radiative recombination an electron directly combines with a hole in the conduction band and releases a photon. In Auger Recombination an electron and a hole recombine while the released energy is transfer to a third carrier, an electron in the conduction band, as sketched in Figure 2.4-1.

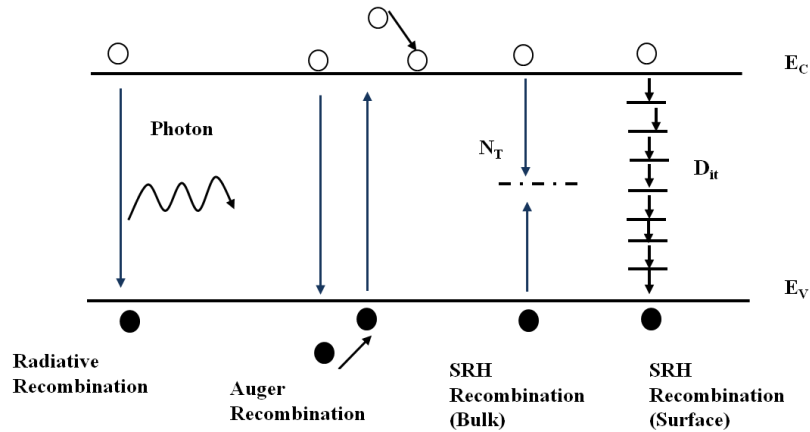


Figure 2.4-1: Major recombination mechanism in semiconductors.

Extrinsic (avoidable) recombination is mainly due to imperfect materials in which recombination occurs through defects and trap states. It is also called Shockley-Read-Hall (SRH) recombination. In SRH, recombination process has two possible paths for electrons (or holes) as shown in Figure 2.4-2.

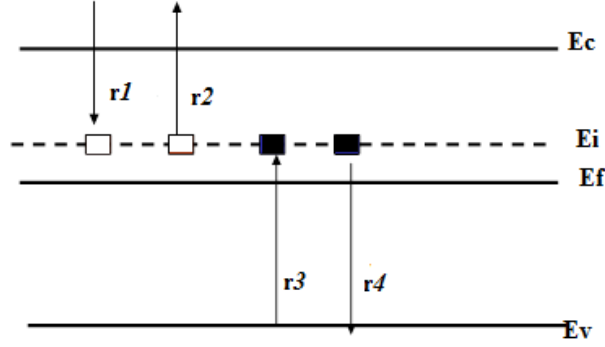


Figure 2.4-2: Four possible interactions of free carrier with localized states by electron and hole ( $r_1$  and  $r_3$ ) capture and emission ( $r_2$  and  $r_4$ ) respectively.

An electron (or hole) is trapped by localized (defect or impurity) state in the material. Then the captured electron (or hole) is thermally released in to valance band and completes the recombination process. To obtain the recombination rate it is assumed that rate of electron capture  $r_1$ - $r_2$  is equal to rate of hole capture  $r_3$ - $r_4$ .

$$U_{SRH} \equiv R - G = r_1 - r_2 = r_3 - r_4 \quad (2.17)$$

According to Shockley, Read [42] and Hall [43] the recombination rate  $U_{SRH}$  is expressed as follows.

$$U_{SRH} = \frac{(pn - n_i^2)}{\tau_{no}[p + p_1] + \tau_{po}[n + n_1]} \quad (2.18)$$

Where  $\tau_{no} = (N_t V_{th} \sigma_n)^{-1}$  and  $\tau_{po} = (N_t V_{th} \sigma_p)^{-1}$  are electron and hole lifetimes respectively.  $N_t$  is the density of defects  $\sigma_{n,p}$  is the capture cross sections of localized (recombination) center  $V_{th}$  is the thermal velocity.

$n_1$  and  $p_1$  express the case when Fermi level and defect level are consistent. Carrier densities in conduction and valance band are given by:

$$n_1 = N_c \exp\left[\frac{(E_C - E_T)}{kT}\right] \text{ and } p_1 = N_v \exp\left[\frac{(E_T - E_V)}{kT}\right]$$

Here  $N_V$  ( $N_C$ ) is the effective density of valance (conduction) band states.  $E_T$  represents the energy level of the trap.

Surface recombination is a special type of SRH recombination. It is generally accepted that the dominating loss mechanism in heterojunction solar cells is SRH recombination at interface states. Any defect or impurity within or at the surface of the crystal causes a recombination of carriers. The surface or the interface of the c-Si wafer corresponds to discontinuity of the crystal lattice. The discontinuity of the crystal lattice leads to the formation of “dangling bonds” whose energy levels are located within the band gap near the semiconductor surface. These localized energy levels act as recombination centers and increase the recombination rate. The high recombination rate at the surface of solar cell has a severe impact on the cell efficiency. Therefore it is crucial to minimize the density of surface states.

The surface SRH recombination rate,  $U_{SRH,S}$ , is expressed as :

$$U_{SRH,S} = S_n S_p \frac{n_s p_s - n_i^2}{(n_s + n_1)S_n + (p_s + p_1)S_p} \quad (2.19)$$

$S_n$  and  $S_p$  represent the surface recombination velocity of electrons and holes, respectively [44].

$$S_n = \frac{U_{SRH,S}}{(n_s p_s - n_i^2)} \quad (2.20)$$

$$S_{n,p} = V_{th} D_{it} \sigma_{n,p} \quad (2.21)$$

$n_s$  and  $p_s$  are the concentrations of electrons and holes at the surface.

To evaluate the effect from the surface recombination rate on the minority carrier lifetime we introduce  $\tau_{eff}$ , the effective lifetime as reciprocal sum of bulk ( $\tau_b$ ) and surface ( $\tau_s$ ) lifetimes ( Eq. (2.22) ).

$$\frac{1}{\tau_{eff}} = \frac{1}{\tau_b} + \frac{1}{\tau_s} \quad (2.22)$$

$$\tau_s = \frac{W}{2S_{eff}} + \frac{1}{D} \left( \frac{W}{\pi} \right)^2 \quad (2.23)$$

Hence by the help of contactless photo conductance decay measurement (the measured value of  $\tau_{eff}$ ), the  $S_{eff}$  can be determined (Eq. (2.23)). In this equation  $D$  is the diffusion coefficient of minority carrier and  $W$  is width of the wafer.

## 2.5 Reducing Recombination

Surface recombination is mainly due to the defects (such as dangling bonds) at the surfaces caused by the interruption of the periodic crystal lattice. Minimizing the density of surface states, hence the high surface recombination is mainly achieved by reducing the number of dangling bonds (also known as surface passivation). The methods to reduce surface recombination are based on: reduction of density of surface states ( $D_{it}$ ) and reduction of concentration of free carriers at the surface [44].

For reducing  $D_{it}$ , generally a thin dielectric layer is deposited on the wafer to passivate dangling bonds. Materials commonly used in Si solar cells are silicon dioxide ( $\text{SiO}_2$ ) [45], silicon nitride ( $\text{SiN}_x$ ) [46] and intrinsic hydrogenated amorphous silicon (a-Si:H) [47].  $\text{SiO}_2$  yields a low  $D_{it}$ , however it is deposited at high temperatures, and suffers from long term UV instability [48]. The  $\text{SiN}_x$  passivation quality depends strongly on the used Si-wafer doping type and level. a-Si:H on the other hand, has gained more interest mostly for hetero-junction solar cells due to the success of Si hetero-junction cells with intrinsic thin-layer. a-Si:H can be grown at low PECVD deposition temperatures (200 °C) which reduces the high temperature processing problems.

The other method for decreasing surface recombination is the reduction of concentration of free carriers. The surface recombination velocity determines the recombination at a surface and recombination velocity depends on the excess concentration of the minority carriers. When the surface electron ( $n_s$ ) and hole ( $p_s$ )

excess concentrations are high and equal to each other  $U_s$  will reach maximum. Therefore reducing the electron and hole density at the silicon surface will reduce the recombination rate. Technologically such a reduction of the surface concentration can be created by passivating surface with a charged a-Si:H layer. The presence of one carrier type in the c-Si near the interface causes the formation of electric fields (built in field) on the semiconductor surface. Formation of electric field hampers recombination either repelling the minority carriers such as in an emitter region or a BSF [49]. Hydrogen plasma method is another scheme for reducing  $D_{it}$  [50]. In this thesis thin a-Si:H(i) layer is used for surface passivation. In Chapter 6 a detailed analysis is given the effect of intrinsic layers to passivation and solar cell performances.

## **CHAPTER 3**

### **EXPERIMENTAL: FABRICATION AND CHARACTERIZATION TECHNIQUES**

In this chapter, fabrication and characterization techniques for a-Si:H film and a-Si:H/c-Si used in the study of this dissertation are introduced. a-Si:H films are deposited by two deposition techniques, plasma enhanced chemical vapor deposition and sputtering. a-Si:H films are investigated by optical and electrical characterization methods. Transmission-reflection spectra, FTIR and Raman spectroscopy are used for optical characterization. For electrical properties conductivity technique is applied. The a-Si:H/c-Si solar cell performance is evaluated by using current density-voltage and quantum efficiency techniques. The passivation quality of the intrinsic and doped layer is analyzed by photo conductance decay method.

#### **3.1 Fabrication Techniques**

This section summarizes the fabrication techniques. The amorphous films with and without hydrogen were deposited by sputtering method. Experiments with sputtering were carried out at laboratories located at Physics Department of METU. The a-Si:H/c-Si solar cells were fabricated by PECVD system at Institute of Energy Conversion (IEC)-University of Delaware.

### 3.1.1 Plasma Enhanced Chemical Vapor Deposition: PECVD

Plasma Enhanced Chemical Vapor Deposition (PECVD) is a widely used method for fabricating a range of thin films including doped and intrinsic a-Si:H films. Chemical Vapor Deposition (CVD) is a process that deposits films from the chemical reactions and decomposition of gaseous precursors at high temperatures. PECVD is a type of CVD which uses electrical energy instead of high temperature to generate a glow discharge (plasma) in vacuum and creates free electrons. In plasma the collision of electrons with the gas molecules leads decompositions of the gases into reactive radicals (ions, neutral atoms and molecules) and other energetic species [51].

Film formation process starts by the interaction of radicals and energetic species with the substrate. The species reaching the surface migrate and find adsorption sites on the substrate. Since the chemical reactions are enhanced by the plasma, the system does not require high thermal energy. Therefore PECVD method allows the film deposition at lower temperatures than in the conventional CVD. The low temperature deposition enables to use cheap and heat-labile materials like plastic or glass as a substrate. In PECVD, plasma is created either by radio frequency (RF) or direct-current (DC) discharge between two electrodes, where space between two electrodes is filled with the reacting gases in a chamber. In this thesis the samples were prepared by DC PECVD. One example of PECVD chamber is shown in Figure 3.1-1.

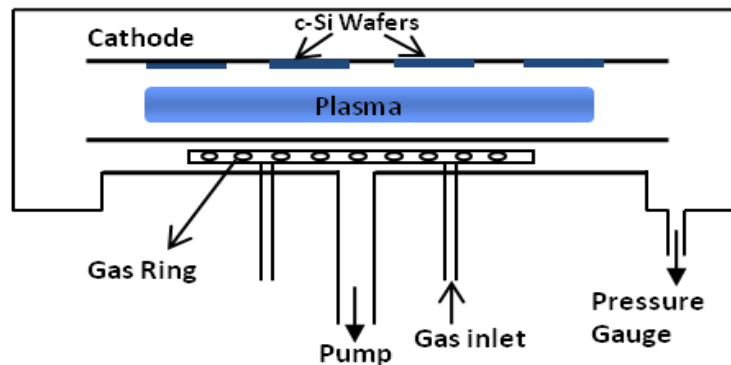
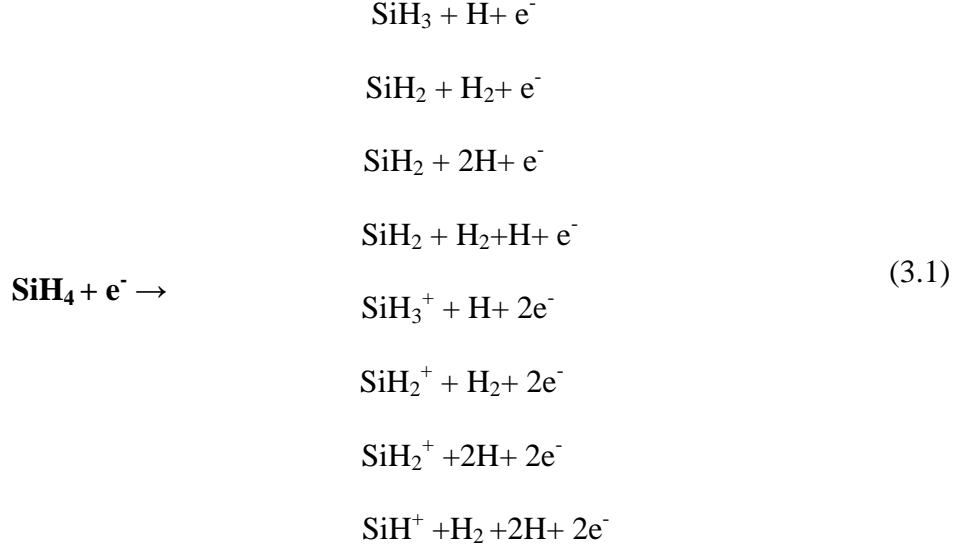


Figure 3.1-1: Schematic cross-section of a deposition chamber in PECVD

The substrate holder grounded on a tray, which serves as the top electrode (cathode) and the second electrode is located under tray which the distance between two electrodes is in a few cm. Reaction gases are introduced through very small holes situated under the anode plate to the process chamber. A turbo molecular pump is used to obtain low pressure in the process chamber. A processing pump is used for controlling the pressure during the deposition. The reaction gas flow rate is controlled by mass flow controllers. After deposition, the waste of reaction gas has to be diluted with chemically non reactive gases such as nitrogen or argon by the exhaust part of process pumps.

### **3.1.1.1 a-Si:H Film Growth by Silane and Hydrogen**

Silane  $\text{SiH}_4$  is the main source gases for the amorphous silicon film deposition. Additionally hydrogen  $\text{H}_2$  is included for the passivating dangling bonds during the amorphous silicon formation. In 1969, Chittick et.al obtained the first intrinsic amorphous silicon films by PECVD [52]. The dominant mechanism of the a-Si:H growth process is the electron impact dissociation of the silane hydrogen gas mixture. Electrons with different energies in the plasma excite the silane molecules depending on their energy. Excited silane molecules dissociate spontaneously to a variety of radicals such as  $\text{SiH}_3$ ,  $\text{SiH}_2$ ,  $\text{SiH}$ ,  $\text{Si}$ , and  $\text{H}$ . Emissive species  $\text{SiH}^*$  and  $\text{Si}^*$  and ionic species, called secondary reactions, are also produced via electron impact dissociation process. The Eq. (3.1) shows the some of the possible dissociations and ionization process.



Densities of radicals, emissive species, and ions in the steady-state silane plasma measured by various methods showed in the Table 2.

Table 2: Steady-state number density of radicals, emissive species and ions in a realistic silane plasma [53].

| Radicals and Ions   | Detection Method              | Density in a plasma/cm <sup>3</sup> |
|---|-------------------------------|-------------------------------------|
| SiH <sub>x</sub> <sup>+</sup> , H <sub>x</sub> <sup>+</sup> | Mass spectrometry             | 10 <sup>8</sup> -10 <sup>9</sup>    |
| Si <sup>*</sup> , SiH <sup>*</sup>                          | Luminosity                    | 10 <sup>5</sup>                     |
| Si  | Laser induced fluorescence    | 10 <sup>8</sup> -10 <sup>9</sup>    |
| SiH   | Laser induced fluorescence    | 10 <sup>8</sup> -10 <sup>9</sup>    |
| SiH <sub>2</sub>  | Intra cavity laser absorption | 10 <sup>9</sup>                     |
| SiH <sub>3</sub>  | Infrared laser absorption     | 10 <sup>12</sup>                    |

The deposition in plasma is a complex process which is difficult to define an exact reaction scheme. It has been reported that the highly reactive species such as SiH<sub>2</sub>, SiH and Si have much smaller values of densities than SiH<sub>3</sub> in the steady-state plasma hence it can be concluded that SiH<sub>3</sub> radicals are the dominant species in film growth [51]. Matsura proposed a surface diffusion growth model as shown in

Figure 3.1-2 [53]. When the  $\text{SiH}_3$  radicals reach to the substrate, it starts to diffuse on the surface. During the surface diffusion,  $\text{SiH}_3$  removes the hydrogen from the surface, forming  $\text{SiH}_4$  and leaving a dangling bond on the surface. Another  $\text{SiH}_3$  radical diffuse toward the dangling-bond site on the surface and forms the Si-Si bond and leads to the film growth. The substrate temperature, plasma power, and gas pressure effects the diffusion growth on the surface.

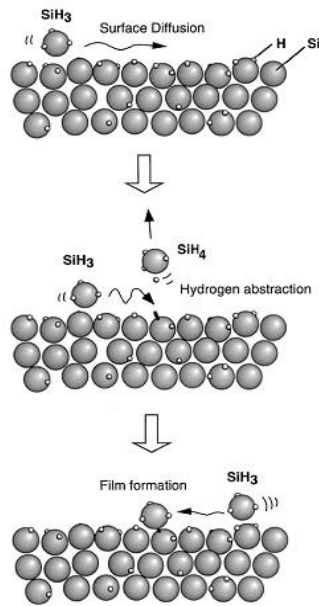


Figure 3.1-2: Steady-state number density of radicals, emissive species, and ions in realistic silane plasma [53].

### 3.1.2 Sputtering Deposition

Sputtering deposition is a physical vapor deposition (PVD) technique for thin-film deposition under plasma condition which utilizes on sputtering effects. Sputtering is basically the physical ejection of atoms from a solid source “target” due to energetic gas ions bombardment. Prior to the sputtering process a high vacuum chamber (base pressures  $\sim 10^{-6}$ - $10^{-7}$  Torr) is needed. Then controlled flow of an inert gas, generally Ar is introduced to the deposition chamber. Applying high voltage (target / cathode, substrate / anode) creates excited  $\text{Ar}^+$  ions and leads to accelerate towards the

negatively biased target. The energetic ions strike the target surface and sputter the target atoms. Sputtered atoms are spread around and they stick onto the substrate in the form of a thin film. Sputtering of a target atom is just one of the possible results of ion bombardment of a surface. When a target is subjected to energetic ion bombardment the electrons also are emitted which is known as secondary-electron emission phenomena. Secondary electron emission is induced the collisions of electrons, ions, neutral atoms and photons. Secondary electron is an important process in order to maintenance of plasma.

The types of discharge generally used are the diode types (operated by DC or RF) and magnetron type. During the sputtering process a magnetic field can be used to trap secondary electrons to the target. Magnetron sputtering cathodes utilize magnets to confine the plasma to the area closest to the 'target'. Magnets create uniform magnetic fields parallel to the targets surface and perpendicular to the electric field and hence the electrons follow helical paths around the magnetic field. This leads more ionizing collisions with neutral gaseous and improves the ionization of the plasma close the target yielding higher sputter rate. The sketch of magnetron sputtering chamber is shown in Figure 3.1-3. The sputtered atoms are not affected by the magnetic field due to charge neutrality. The magnetron sputtering can be done by direct current (DC) or radio frequency (RF) power supplies. For the sputtering process several varieties of materials can be used as targets, ranging from pure metals where a DC power supply can be used to semiconductors and isolators which require a RF power supply.

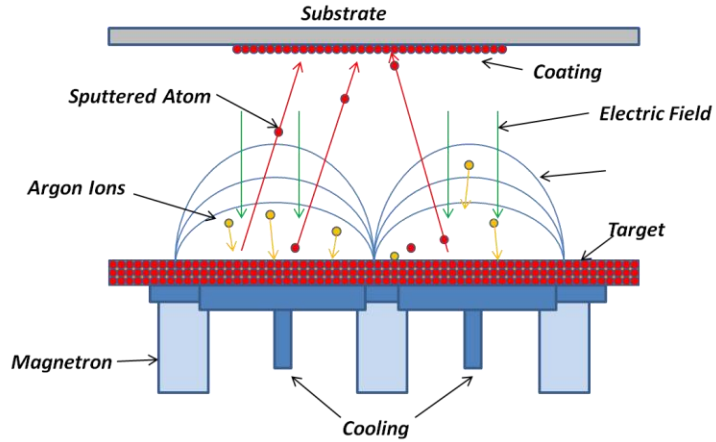


Figure 3.1-3: The schematic representation of magnetron sputtering chamber.

In this thesis sputtering technique was applied for a-Si:H deposition for solar cells application, transparent conductive oxide (TCO) and metal contact depositions. The sputtering system used in the a-Si:H deposition is Nano D100 magnetron sputtering system constructed by Vaksis. It has three independent magnetrons at the bottom of the vacuum chamber. Both RF and DC power supplies are present; also the sample can be rotated to obtain more uniform thin films. In Figure 3.1-4 and Figure 3.1-5, the picture of the sputtering system used in this work is shown.

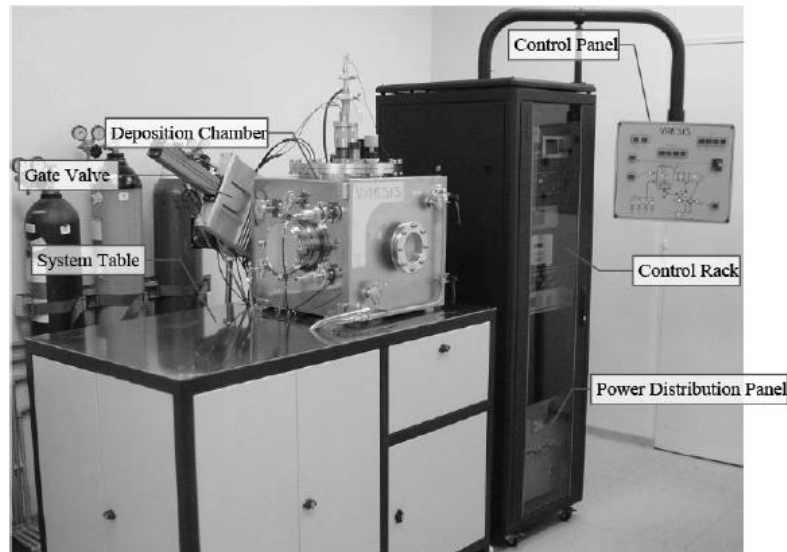


Figure 3.1-4: Picture of nano-D100 sputtering system

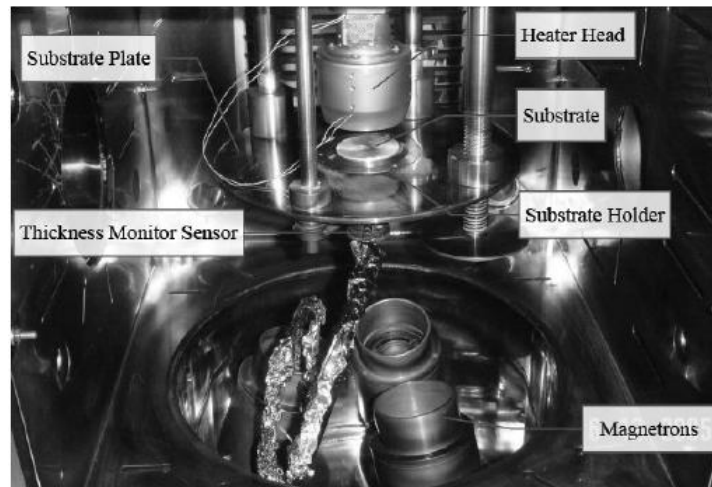


Figure 3.1-5: Picture of the sputtering chamber

In this section, the preparation of the wafers before the deposition is summarized in terms of the substrate cleaning. Further, fabrication steps of SHJ are briefly explained.

### 3.1.3 Substrate Cleaning

In a-Si:H/c-Si solar cells, a thin a-Si:H layer is deposited on clean c-Si wafer. Preparation of the wafer surface before fabrication has a significant effect on the performance of the solar cell as well as the wafer and doped a-Si:H layers quality. It has been reported that cleaning of the wafer surface has a crucial impact on reducing the surface recombination hence achieving high  $V_{oc}$  [54], [55], [56]. The wafers used in this research are double side polished 4 inch p type zone (FZ) mono-crystalline. The wafers have the thickness of 300  $\mu\text{m}$  with the resistivity of 2  $\Omega\cdot\text{cm}$ . Before cleaning, the 4 inch wafers are cut into smaller 1 $\times$ 1 inch squares by a diamond scribe or if needed by a laser saw.

The wafer cleaning is mainly based on three parts of wet chemical cleaning process. The sequence of the Si wafer cleaning is listed as:

1. The wafer pieces are firstly cleaned in ultrasonic bath with the chemicals:
  - 5 minutes in acetone
  - 5 minutes in methanol
  - Rinse with isopropanol alcohol (30sec).
  - Rinse with 5 minutes in de-ionized water (DI-water)
  - Blow dry with compressed nitrogen.

The first step is important to get rid of debris and hydrocarbon contamination during the growth of Si wafers.

2. The ultrasonic cleaning followed by a wet chemical oxidation of 2:1 Sulfuric acid ( $H_2SO_4$ ): Hydrogen Peroxide ( $H_2O_2$ ) etch, mostly called piranha, for five minutes at the temperature of 70-80 °C. Wet-chemical oxidation that both dissolve impurities including ionic, metallic, and surface hydrocarbon as well as growing oxide surface on Si wafer. Wet oxidation is followed by 5 min. rinsing with DI-water
3. Wafers are dipped in 10% hydrofluoric (HF) solution for 60 sec. to etch the oxide layer. The wafers should be hydrophobic after HF dipping. After this step wafers are loaded immediately to the deposition system.

Note that, for cleaning glass substrates only first step is applied.

### **3.1.4 a-Si:H /c-Si Solar Cell Fabrication by PECVD**

Following wet chemical cleaning, the wafers are transferred into the in-line multi chamber PECVD deposition system. The PECVD deposition system in IEC has two load locks chambers with four process chambers as display in Figure 3.1-6. The wafers are placed on a substrate holder tray that can hold sixteen 1×1 inch / four 3×3 inch / four 5×5 inch / one 1×1 ft. substrate. The substrate tray can be easily slide from one deposition chamber to another. Different chambers are used to deposit p, n, and intrinsic amorphous layers to avoid cross contamination from the chamber atmosphere.

If the cell structure contains buffer intrinsic layer, firstly thin intrinsic layers are deposited on the both sides of the wafer. A manually flipper mechanism is used to flip over the wafers in order to deposit other side of the wafer without breaking the vacuum. The flipper can hold four 1×1 inch wafer pieces.

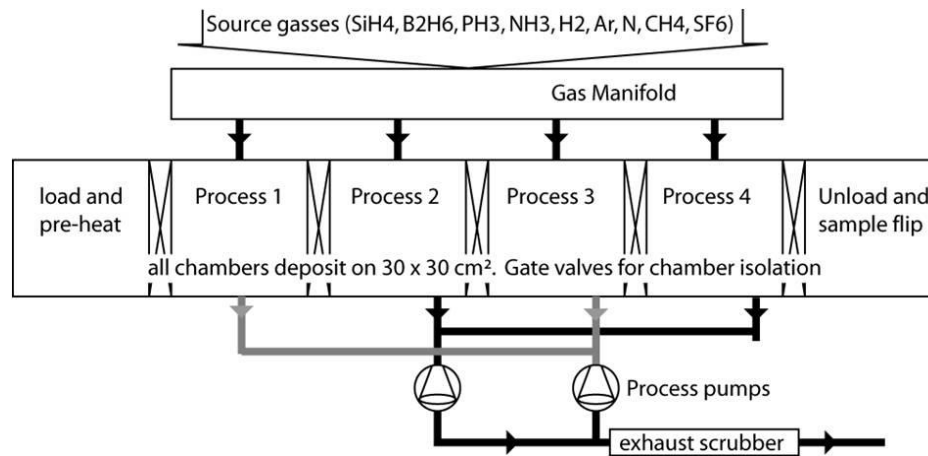


Figure 3.1-6: A basic diagram of multi chamber PEVCD system at IEC.

If the flipper cannot be used, the sample tray is moved to the load lock chamber to turn down samples with breaking the vacuum. When the samples exposed to atmosphere contamination and unwanted oxide growth can occur. To get rid of these effects, wafers with one side film can receive a second HF etch before another deposition. The second HF dip is a standard procedure to prevent silicon dioxide from forming on the sample which can lower the open-circuit voltage [55]. Following i layer deposition, first a thin a-Si:H(n) layer is deposited on front side of wafer to form the junction, and then a ~10 nm a-Si:H(p) layer is deposited on the rear side of the wafer to passivate back surface field and contact. The process gases for intrinsic layer deposition are hydrogen ( $H_2$ ) and silane ( $SiH_4$ ). For doped a-Si:H layers phosphine ( $PH_3$ ) and diborane ( $B_2H_6$ ) gases are introduced to the ( $H_2$ ) and ( $SiH_4$ ) gas mixture for n and p type doping respectively. The sequence of n and p layers deposition is important because diborane begins to dissociate into hydrogen and boron at the deposition temperature of ( $200\text{ }^\circ\text{C}$ ). Boron contamination on the wafer surface causes low  $V_{oc}$ .

a-Si:H film properties and solar cell device properties are dependent to deposition conditions; specifically deposition temperature, SiH<sub>4</sub>, H<sub>2</sub> and doping gases flow rates and ratio, plasma power. In this thesis, the influence of these deposition parameters on emitter a-Si:H(n) layer are investigated in Chapter 5 and 6.

After doped layers, a 70 nm indium tin oxide (ITO) is deposited on the front side of the solar cell by sputtering. ITO is transparent in visible light and it is widely used in SHJ solar cells as an anti reflecting coating which reduces the reflectance of incident light. The other advantage of fabricating ITO is its high conductivity which improves the charge carrier collection. ITO is fabricated by using a shadow mask with four separate parts with the areas of 0.56 cm<sup>2</sup> Figure 3.1-7.

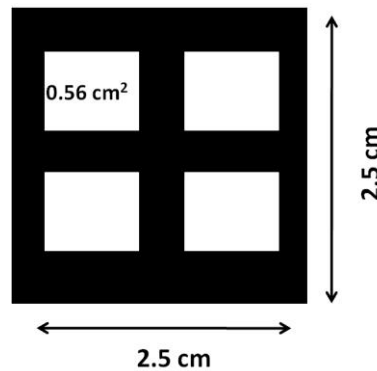


Figure 3.1-7: Sketch of shadow mask for ITO deposition on the front side of SHJ solar cell

Following ITO, Ni/Al grids are deposited on the ITO for front contacts with the mask of bus bar which positioned on the active area of 0.56 cm<sup>2</sup> cells. The sketch of the grid mask is shown in Figure 3.1-8b.

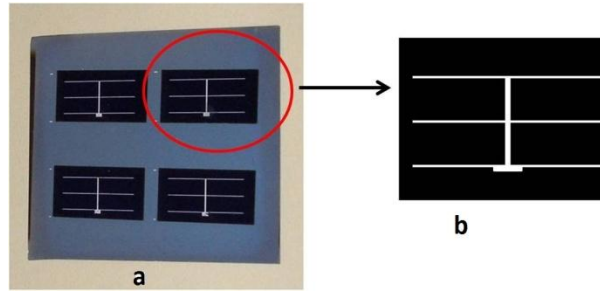


Figure 3.1-8: Picture of a complete cell (a) and the sketch of bus bar mask for Ni/Al deposition on ITO (b)

For the rear contact 0.5  $\mu\text{m}$  thickness Al is coated by the electron beam deposition system. The resultant device is shown in Figure 3.1-8b.

## 3.2 Characterization Techniques

### 3.2.1 Quantum Efficiency

Quantum efficiency (QE) measurement is one of the most functional characterization techniques for solar cells. QE allows quantifying the efficiency of the conversion of absorbed photons to electrical current as a function of the wavelength. Quantum Efficiency can basically be defined as the ratio of the number of charge carriers that are collected to the number of impinged photons of a given wavelength shining on the solar cells.

$$QE = \frac{\text{Number of Charge Carriers}}{\text{Number of Photons}} \quad (3.2)$$

The QE is zero for the photons with energy below the band gap. If a QE is 1, this implies that all the photons of a certain wavelength are absorbed and the resulting carriers can be collected. In ideal case QE has a rectangular shape as shown in

Figure 3.2-1. However for most solar cells it is not an exact rectangular shape. Because of the recombination effects or optical losses (reflected or parasitically absorbed photons), QE ranges from 0 to less than 1.

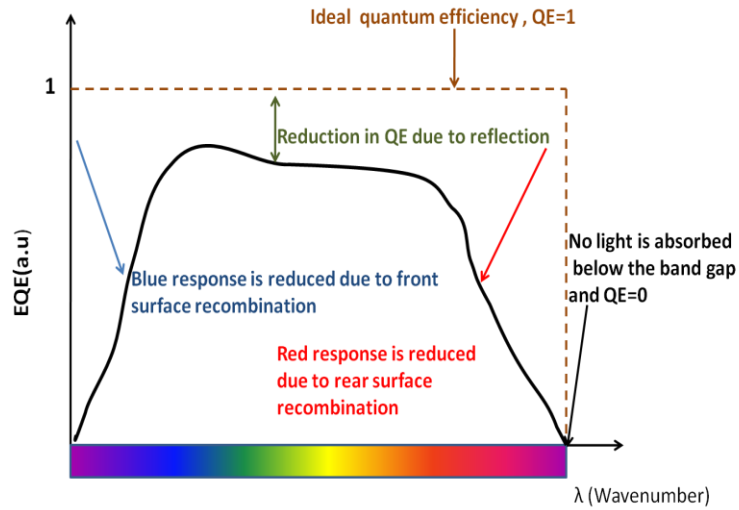


Figure 3.2-1: Possible reduction in quantum efficiency of a silicon solar cell is shown. Ideal quantum efficiency has a rectangular shape with a QE of 1 at whole spectra [57].

Generally two types of QE of a solar cell are measured. One is the “external quantum efficiency” (EQE) includes the efficiency of optical losses. The other one is “internal quantum efficiency” (IQE) refers to the efficiency which subtracts the effect of photons that are reflected or transmitted out of the cell. Internal quantum efficiency can be calculated via the corrected external quantum efficiency curve by extracting the reflection spectra of a device (Eq. (3.3))

$$IQE(\lambda) = \frac{EQE(\lambda)}{1 - R(\lambda)} \quad (3.3)$$

In this study, we will analyze only EQE measurements to obtain information about the photocurrent and determine optical loss mechanisms responsible for reducing the  $J_{sc}$ . A typical QE measurement setup has a tunable light source, detection system

and accessories for proper beam manipulation and delivery. Figure 3.2-2 shows the QE set up at IEC.

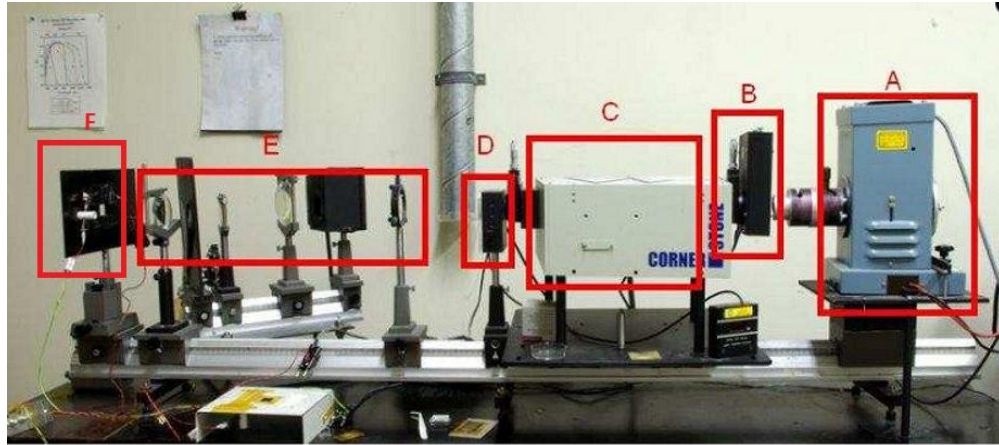


Figure 3.2-2: Optical Stage of the QE system at IEC. A) Light source, B) Filter wheel, C) Monochromator, D) Light chopper, E) Collimating and focusing lenses, F) Sample stage

The light source in Figure 3.2-2 is a 200 W quartz tungsten halogen (QTH) projector lamp. Light passes through the filter wheel and through the monochromator, which disperses the white light using the ruled grating. The monochromatic light goes through the light chopper that operates at 72 Hz. A chopper is used to provide a reference signal for the lock-in amplifier and facilitates phase sensitive detection. After chopper, the monochromatic light passes the collimating and focusing lenses. The monochromatic beam with an area of  $0.40 \text{ mm}^2$  is focused on the sample which is mounted on a stage in the path of the monochromatic beam [58]. The spectral response signal is measured through series of electrical connections, pre amplifier and a lock-in amplifier. The signal is then sent to the oscilloscope and the lock-in amplifier; the amplifier matches this signal with the signal from the chopper. The ammeter and the voltmeter monitor the current and voltage of the system. The QE system is controlled via a computer. Additional to white light, red or blue filters can be placed in the front of the light source for bias light measurements. In this work QE measurements were performed on different a-Si:H/c-Si solar cells in the range of 350-1200 nm.

### 3.2.2 Current Density-Voltage Measurements

Current density voltage (J-V) analysis is the widely used experimental technique to characterize solar cells. Figure 3.2-3 shows an example of J-V curve for a solar cell. Three major electrical parameters that ultimately define the cell efficiency: the open circuit voltage ( $V_{oc}$ ), short circuit current density ( $J_{sc}$ ) and the fill factor (FF) are obtained by analyzing J-V curve.

The definitions of the parameters in Figure 3.2-3 are:

- $I_{sc}$  is the current through the solar cell when voltage across the solar cell is zero. The  $I_{sc}$  occurs due to the generation and collection of photo generated carriers. Ideally  $I_{sc}$  is equal to the light generated current,  $I_L$ , at zero bias. It is more common to use the short circuit current density  $J_{sc}$  in ( $\text{mA} / \text{cm}^2$ ) rather than the  $I_{sc}$  to eliminate the dependence of the solar cell area ( $J = I / \text{Area of the solar cell}$ )
- $V_{oc}$  occurs when there is no current passing through the cell.  $V_{oc}$  refers to the amount of bias on the solar cell due to the bias of the solar cell junction with the light generated current [57].
- FF is a metric of “squareness” of the current density-voltage curve under illumination and it is a metric for the quality of the solar cell. The maximum power point of a solar cell is the point that maximizes J-V and can be found by the condition  $\frac{\partial P}{\partial V} = 0$ . As can be seen in Figure 3.2-3 the maximum power output of an ideal solar cell is found by the product of maximum voltage and maximum current density  $P_m = J_m \times V_m$ .

$$FF = \frac{P_{\max}}{V_{oc} J_{sc}} = \frac{V_{mp} J_{mp}}{V_{oc} J_{sc}} \quad (3.4)$$

The efficiency,  $\eta$ , of a solar cell is the ratio of the maximum power output of solar cell to the power incident due to solar irradiation and given by,

$$\eta = \frac{P_{out}}{P_{in}} = \frac{V_{mp} J_{mp}}{P_{in}} = \frac{V_{oc} J_{sc} FF}{P_{in}} \quad (3.5)$$

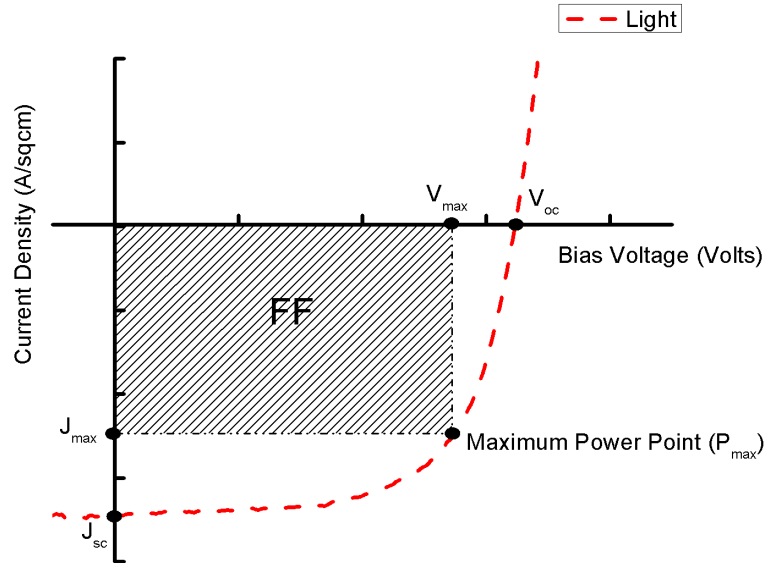


Figure 3.2-3: Example of a current density voltage (J-V) curve and the characteristic parameters.

The current density is for an ideal solar cell, without considering recombination effects and parasitic losses, is described by Eq. (3.6).

$$J = J_0 \left[ \exp\left(\frac{qV}{kT}\right) - 1 \right] - J_L \quad (3.6)$$

The first term in Eq. (3.6) describes the dark diode current density, where  $J_0$  represent a constant saturation current,  $k$  is Boltzmann's constant and  $T$  is temperature in degrees Kelvin. The second term describes the photo generated current density. For an ideal solar cell ( $J_L = J_{sc}$ ).

The ideal solar cell can be described by a simple equivalent circuit, in which a diode and a current source are connected in parallel as shown in Figure 3.2-4

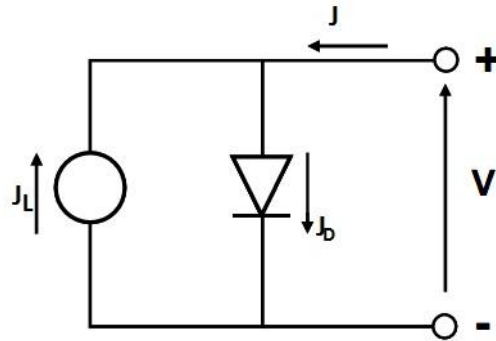


Figure 3.2-4: The equivalent circuit of an ideal solar cell

In real solar cells FF is influenced by several parasitic resistances such as series resistance,  $R_s$ , and the shunt resistance  $R_{sh}$ .  $R_s$  arise from bulk resistance of the layers forming the cell, front and back contact resistance. The series resistance is the resistance of the main current path through which the photo-generated carriers arrive to the external circuit.  $R_s$  does not affect open circuit voltage however it has an severe influence on the FF. Shunt resistance represent the leakage across the junction and around the cell edge. For lower shunt resistance photo generated carriers recombine by leakage and could not reach the contact by resulting reduction in efficiency. Figure 3.2-5 shows the equivalent circuit model for real solar cell consists of a diode in parallel with a photo current generator and two resistive elements, one in series with the circuit, and the other in parallel to diode.

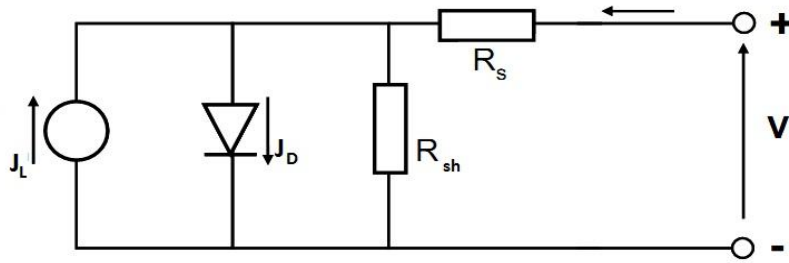


Figure 3.2-5: The equivalent circuit of a solar cell with series and shunt resistance.

For an efficient current flow and high FF for a solar cell,  $R_s$  should be as small and  $R_{sh}$  should be as large as possible. The current density with including parasitic resistances is expressed by the Eq. (3.7).

$$J = J_0 \left[ \exp \left( \frac{q(V - JR_s)}{nkT} \right) - 1 \right] - \left( \frac{V - JR_s}{R_{sh}} \right) - J_L \quad (3.7)$$

Here  $n$  is the ideality factor typically lies between 1 and 2.

Typically the value of  $(V - R_s J) / R_{sh}$  is negligible compared to dark diode current and  $J_L$ . Then the Eq. (3.7) can be expressed as:

$$J = J_0 \left[ \exp \left( \frac{q(V - JR_s)}{nkT} \right) - 1 \right] - J_L \quad (3.8)$$

The  $R_s$  and ideality factor can be obtained from Eq. (3.8) by some mathematical steps as represented in Eq. (3.9) and Eq. (3.10).

$$V = R_s J + \left[ \frac{nkT}{q} \right] \left[ \ln(J + J_L) - \ln(J_0) \right] \quad (3.9)$$

The derivative of  $V$  with respect to  $J$  ( $dV/dJ$ ) is:

$$\frac{dV}{dJ} = R_s + \frac{nkT}{q}(J + J_L)^{-1} \quad (3.10)$$

Where,

$$\frac{dR_s}{dJ} = 0$$

Ideality factor ( $n$ ) and  $R_s$  can be extracted from linear fit of  $dV/dJ$  vs  $(J + J_L)^{-1}$ . Ideally the graph of  $dV/dJ$  vs  $(J + J_L)^{-1}$  at a given temperature would be linear and a linear fit allows to calculate the ideality factor from the slope and the intercept will yield the series resistance [59].

Typically a J-V measurement system includes a light source, bias voltage supply, the measurement electronics and software to visualize the J-V curves. J-V measurements of our samples are done by an Oriel solar simulator under dark and light. The standard AM 1.5 testing conditions are applied for testing the solar cells. This testing condition requires the AM 1.5 spectrum,  $100 \text{ mW/cm}^2$  (one sun of illumination) light intensity, and cell temperature of  $25 \text{ }^\circ\text{C}$ . Cell temperature during JV measurements is tracked by a temperature sensor contacting the front surface of the cell. A thermo-electric cooler system is used to control the cell temperature and insure AM1.5 temperature conditions of  $25 \text{ }^\circ\text{C}$ . The cells are contacted with four point measurement technique to eliminate the effect of probe/cell contact resistance. (For detailed analysis for four probe method see [36]). The voltage bias supply is the Keithley 2400 which starts at  $-1.0 \text{ V}$  and swept into forward bias to the current limit of  $50 \text{ mA/cm}^2$ . The signal from the device is sent to the Keithley 2400 source measure unit (SMU) which is interfaced to a computer. JV sweeps are performed in light and dark for increasing voltage (reverse to forward bias) and then in the reverse direction to evaluate constancy. Figure 3.2-6 and Figure 3.2-7 show actual picture of the setup at IEC and METU respectively, used for JV measurements.

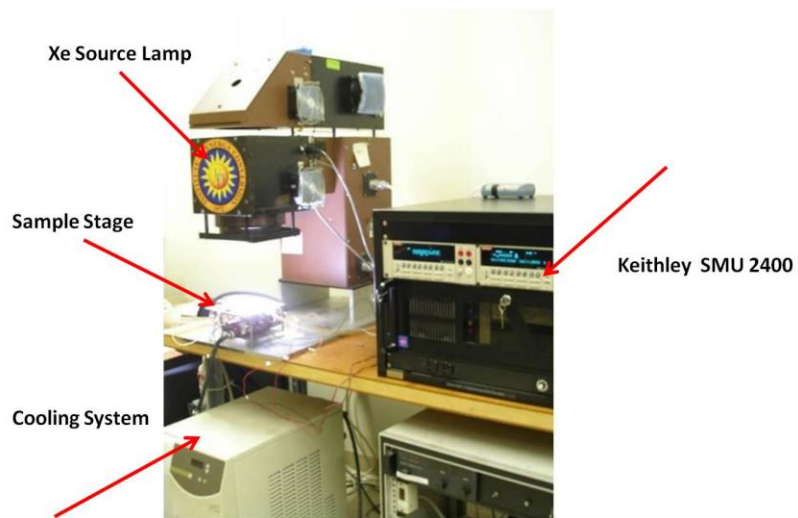


Figure 3.2-6: Picture of JV system. The simulator lamp shines on the sample placed on the stage. On the right is the source measurement unit which sweeps the voltage and measures the current.



Figure 3.2-7: Solar simulator used for JV analysis of the cells deposited by sputtering.

### 3.2.3 Effective Minority Carrier Lifetime Measurement

Measurements of minority carrier lifetime in SHJ cells are very important for controlling fabrication and device optimization. Minority carrier lifetime in a

semiconductor refers to the time of a minority carrier moves freely before recombination. Minimizing the surface recombination is one the main aspects in SHJ to obtain high  $V_{oc}$ . Measuring minority carrier life time allows obtaining information about the recombination rates and surface passivation quality [54]. The measured lifetime is usually called effective lifetime,  $\tau_{eff}$ , which is sum of all the recombination losses that occur within the c-Si bulk ( $\tau_b$ ) and surface ( $\tau_s$ ):

$$\frac{1}{\tau_{eff}} = \frac{1}{\tau_{bulk}} + \frac{1}{\tau_{surf}} \quad (3.11)$$

The most used method to measure,  $\tau_{eff}$  is the photoconductive decay (PCD) method [60]. This technique is basically based on the analysis of the photo conductance decay by time after a very short light stimulation. Conductance of a semiconductor changes under light stimulation. Since photoconductivity is a property dependent upon mobile free carriers, the time dependence of the photoconductivity is directly related with the  $\tau_{eff}$  and hence recombination rates. The PCD technique can be applied to the devices without their contacts which gives the possibility of measuring life time on devices at any step of fabrication. There are three types of contactless PCD methods depending on the stimulating modes [61]. The first mode light excitation is abrupt and analysis of photo conductance analysis is held after a short time of illumination (the transient decay method). This method can be applied high life time samples (>1 ms).

The second mode is the steady-state illumination. The third mode is the quasi-steady-state illumination (QSSPC).

The light stimulation leads the generating of electron-hole pairs (excess carriers) in the solar cell. The continuity equation for excess carrier is given by the Eq. (3.12)

$$\frac{\partial \Delta n(t)}{\partial t} = G(t) - R(t) \quad (3.12)$$

Where  $G$  is the generation rate,  $R$  is recombination rate in the bulk,  $\Delta n(t)$  is the excess minority carrier density. For the transient decay method  $\frac{\Delta \partial n(t)}{\partial t}$  is measured after light pulse then  $G$  is zero and then the rate of carrier density change is equal to the recombination rate:

$$\frac{\partial \Delta n(t)}{\partial t} = -\frac{\partial n}{\tau_{eff}} \quad (3.13)$$

Where

$$R = \frac{\partial n}{\tau_{eff}} \quad (3.14)$$

For the second mode, due to steady state illumination  $\frac{\Delta \partial n(t)}{\partial t}$  is zero. In the QSSPC mode the flash lamp is used to produce a slowly varying illumination and the resulting time dependence of the excess photo conductance of the sample is measured. Figure 3.2-8 displays sketch of the measurement set up.

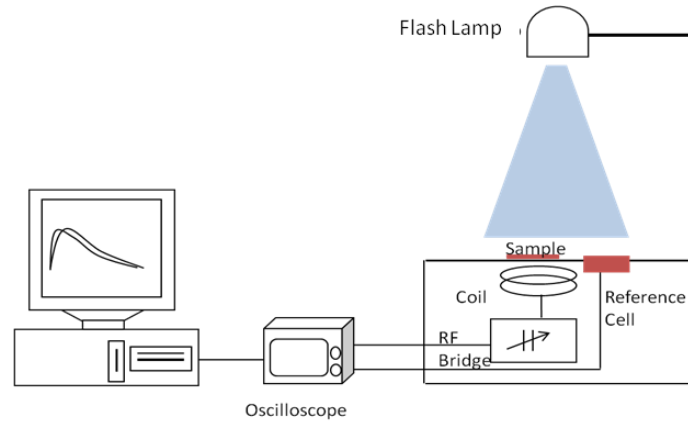


Figure 3.2-8: Figure of QSSPC setup for effective lifetime measurement. The inductively coupled coil with RF bridge circuit detects the photo conductivity changes of the sample. The reference cell evaluates the generation rate of illumination light. Both signals are amplified and preceded by an oscilloscope and recorded by software

For QSSPC mode  $\tau_{eff}$  is represented as:

$$\tau_{eff} = \frac{\Delta n(t)}{G(t) - \frac{\partial \Delta n(t)}{\partial t}} \quad (3.15)$$

The parameters in right hand side of Eq. (3.15) can be obtained by QSSPC and enables to find  $\tau_{eff}$ .

When the flash lamp illuminates the silicon wafer, the light causes increase in the conductivity (photoconductivity). The time dependence change in the photoconductivity of the silicon wafer is detected by radio frequency inductive coil (connected to a bridge circuit) situated beneath the sample stage. It senses the photoconductivity change by the imbalance of the bridge. Detecting the photoconductivity changes ( $\Delta\sigma_L$ ) leads us to find excess carrier density  $\Delta n(t)$  by the Eq. (3.16).

$$\sigma_L = q\Delta n(t)(\mu_n + \mu_p)W \quad (3.16)$$

Here W represents the thickness of the sample and  $\mu_n$ ,  $\mu_p$  are the electron and hole mobility's which are well known for Si.

The generation rate, G(t), is measured by using a calibrated solar cell.  $\frac{\Delta\sigma_L(t)}{\partial t}$  is obtained by the monitoring of incident light pulse decays in QSSPC mode. Figure 3.2-9 displays the flash lamp light intensity on the left axis and photo conductance on the right of a sample analyzed in the transient decay mode from the Sinton Tester software. The software used for life time measurements does the calculations regarding of Eq. (3.13) and displays with the other parameters in an excel sheet.

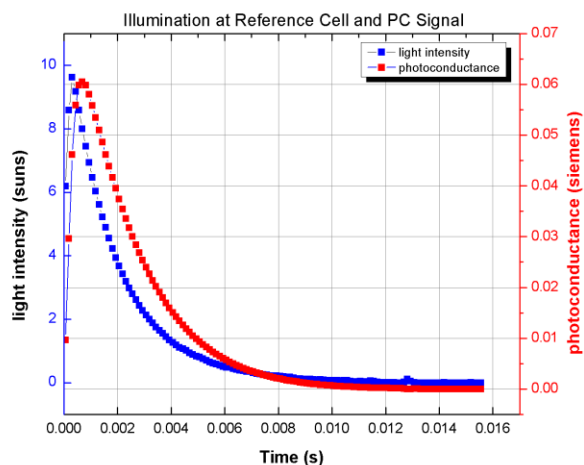


Figure 3.2-9: Flash lamp light intensity and photo conductance decay as a function of time.

In our study, the effective lifetime measurements are measured using commercially available Sinton WCT100 instrument in QSSPC. Figure 3.2-10 shows the picture of the instrument.

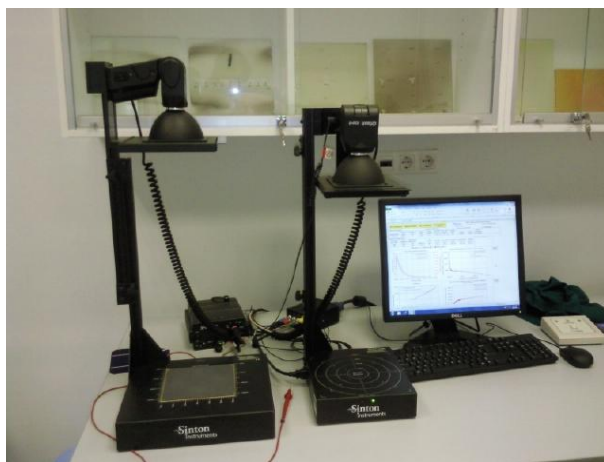


Figure 3.2-10: Picture of Sinton WCT100 for effective lifetime measurement.

### 3.2.4 Conductivity Measurement

To achieve high efficiency solar cells it is needed to minimize parasitic resistive losses as well as recombination losses. Both shunt and series resistance losses decrease the fill factor and efficiency of a solar cell. The series resistance is affected by the contact, wafer and doped layers resistivity. In this study the resistivity of the doped layer is evaluated by the conductivity measurements. For the conductivity measurement, a-Si:H thin film is grown on glass and Ohmic Al contacts are deposited on the film. The conductivity  $\sigma$  is obtained by applying a voltage  $V$  between the electrodes, and measuring the current via using the formula:

$$\sigma = \left(\frac{I}{V}\right) \left(\frac{W}{l \cdot d}\right) \quad (3.17)$$

Where  $d$  is thickness of thin film,  $W$  is distance between the contacts,  $l$  and is contact length. Temperature dependent conductivity measurements allow obtaining activation energy ( $E_a$ ) of doped layers.

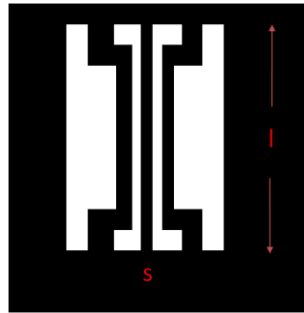


Figure 3.2-11: The shadow mask using for conductivity measurements

$E_a$  refers to the distance of the Fermi level ( $E_F$ ) from the conduction band edge ( $E_c$ ) for n type doped and intrinsic and distance from the valance band edge ( $E_v$ ) for p type doped a-Si:H films.

$E_a$  is obtained from the temperature dependent conductivity formula:

$$\sigma = \sigma_0 \exp\left(\frac{-E_a}{kT}\right) \quad (3.18)$$

### 3.2.5 Transmission and Reflection Measurements

The Beer-Lambert Law is an efficient tool to analyze transmittance to obtain information about optical properties of films. Neglecting the reflectance contribution, Beer-Lambert Law is represented by Eq. (3.19). In Eq. (3.19),  $I_T$  and  $I_0$  show transmitted and incident light intensities, respectively;  $\alpha$  is the absorption coefficient, and  $d$  is the sample thickness.

$$I_T = I_0 \exp(-\alpha d) \quad (3.19)$$

From Eq. (3.19)  $\alpha$  can be obtained as:

$$\alpha = \frac{1}{d} \ln\left(\frac{I_0}{I_T}\right) \quad (3.20)$$

The absorption coefficient is also calculated for a direct or indirect semiconductor from Eq. (3.21) [62].

$$\alpha = C \sum n_i n_f P_{if} \quad (3.21)$$

Where  $C$  is a constant, and  $P_{if}$  is the probability of the transitions from the initial to the final state,  $n_i$  is the density of electrons in the initial state and  $n_f$  is the density in final states. The summation is over all states separated by photon energy.

From Eq. (3.21), it can be seen that, the absorption coefficient is related to the transition probabilities between the electronic energy levels. Using the transition probability between the valence and conduction bands, calculated by the help of the quantum perturbation theory, the dependence of the absorption coefficient on photon energy and band gap energy for semiconductors can be written as in Eq.(3.22).

$$(\alpha h\nu) = A (h\nu - E_g)^p \quad (3.22)$$

Where A is a constant independent of  $h\nu$  and mainly depends on the transition probability, p is an index that characterizes the optical absorption process, and it is theoretically equal to 2 and 1/2 for indirect and direct allowed transitions, respectively.

The transmission experiments were carried out for all samples having different deposition conditions by UV-Visible spectrometer. From transmission spectra the absorption coefficient,  $\alpha$ , was calculated using Eq. (3.20). Analysis of the experimental data have shown that the absorption coefficient and the photon energy of indirect semiconductors can be related by Eq. (3.22) with  $p=2$  [62]. The optical gap “ $E_g$ ” can be derived from  $(\alpha h\nu)^{1/2}$  vs  $f(h\nu)$  plot. From the,  $(\alpha h\nu)^{1/2}$  vs  $f(h\nu)$  plot also known as Tauc plot, we can estimate the optical band gap “ $E_g$ ”.

## CHAPTER 4

### SHJ SOLAR CELLS FABRICATED BY MAGNETRON SPUTTERING

In this chapter the performance of SHJ solar cells fabricated by magnetron sputtering is summarized. The analysis in the chapter is divided into two parts. In the first part non hydrogenated (a-Si) and hydrogenated (a-Si:H) amorphous silicon thin films deposited on quartz substrates were investigated.

In the second part a-Si:H(n)/c-Si(p) solar cells were investigated. A complete a-Si:H(n)/c-Si(p) device was obtained by depositing a thin a-Si:H(n) layer on c-Si(p) wafers by sputtering method. Optical transmission analysis and Raman spectroscopy techniques were applied to examine optical and micro structural characteristics of a-Si:H films. The performances of solar cells were evaluated by current-voltage analysis.

#### **4.1 Amorphous Silicon Films Deposited by DC Magnetron Sputtering Technique**

Amorphous silicon is one of the major materials used in today's microelectronic and photovoltaic technology. Amorphous silicon films are usually fabricated by physical and chemical deposition techniques for which the process conditions such as substrate temperature, gas pressure, discharge power and the film thickness can be controlled.

The low deposition temperature is crucial in the production of a-Si:H/c-Si solar cells to eliminate the problems of defect creation and doping redistribution associated

with high temperature processing [63]. DC-RF magnetron sputtering techniques provide good quality a-Si:H films with high deposition rates at relatively low deposition temperatures. The magnetron sputtering technique avoids using of toxic gases for doping which eliminates considerable safety problems and expensive protection systems. Moreover solid sputtering targets that are initially doped can last for many years, which an economical advantage both for laboratory researches and large scale manufacturing [64].

This section describes the study for achieving high quality amorphous silicon films deposited by DC magnetron sputtering technique. Raman spectroscopy, optical transmission measurements were applied to determine the micro structural and optical characteristics of a-Si films. The analysis of the optical transmission spectra allows getting information about absorption coefficient, band gap and several optical properties of the material.

#### **4.1.1 Experimental**

a-Si films were deposited on quartz substrates to investigate film properties. Quartz substrates were cleaned by ultrasonic treatment in acetone followed by an ultrasonic treatment in alcohol. After each treatment substrates were rinsed by distilled water. The amorphous films were deposited by nano-D 100 DC & RF magnetron sputtering system (manufactured by Vaksis ltd.) located in Phys. Dept. at METU. The sputtering target was n-type mono-crystalline silicon and chamber pressure was kept constant at 4 mTorr during the deposition. The substrate temperature ( $T_s$ ) can be maintained at room temperature with water cooling or heated at temperatures up to 500 °C. The films were deposited at different substrate temperatures on cleaned quartz wafer. The a-Si was sputtered in an atmosphere of argon. The deposition condition parameters are summarized in Table 3. A Dektak profilometer was used for measuring the film thicknesses. The optical characteristics of the films were determined by means of a UV-Visible spectrometer in the wavelength range from 200 to 1100 nm. From the transmission spectrum optical band gaps of films were obtained using the method

explained in Section 3.2.5. Figure 4.1-1 shows, as an example, Tauc plot of 200 nm a-Si film and fitted solid line to a linear equation to evaluate the band gap (1.42 eV).

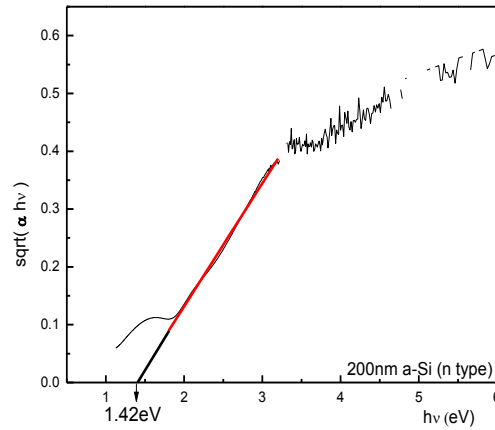


Figure 4.1-1: Dependence of  $(\alpha h\nu)^{1/2}$  on photon energy for 200 nm a-Si film deposited at room temperature .

## 4.1.2 Results and Discussion

The optical band gaps of different films measured by analyzing transmission spectrum were summarized in Table 3. As it is seen from Table 3 the band gap increases slightly by increasing substrate temperature. For the window effect of an emitter layer, its band gap should be high to use the incoming light in most efficient way. In this point of view the a-Si(n) deposited at high temperature seems more suitable as an emitter layer for a SHJ solar cell. However as mentioned in previous chapters processing at high temperatures has destructive effects on life time of minority carriers due to temperature dependent recombination centers. Additionally the samples deposited at high temperatures showed microstructure phase besides amorphous phase via Raman spectroscopy as presented in Figure 4.1-2.

Table 3: a-Si deposition condition parameters by DC magnetron sputtering.

| Argon Pressure (mTorr) | Argon Flow Rate(sccm) | DC Power(W) | T <sub>s</sub> ( <sup>o</sup> C) | Film Thickness(nm) | Band Gap (eV) |
|------------------------|-----------------------|-------------|----------------------------------|--------------------|---------------|
| 4                      | 20                    | 150         | Room Temp.                       | 200                | 1.42          |
| 4                      | 20                    | 150         | 200                              | 200                | 1.50          |
| 4                      | 20                    | 150         | 300                              | 200                | 1.55          |
| 4                      | 20                    | 150         | 500                              | 200                | 1.76          |

Raman spectroscopy technique was applied to obtain information about the micro structures of the films. The Raman spectrums in Figure 4.1-2 showed a peak around 475 cm<sup>-1</sup> which indicates that structure of these films is amorphous. However, the spectrum of the film deposited at 500 °C presents also a peak around 515-520 cm<sup>-1</sup> which indicates the presence of crystalline phase within the amorphous phase.

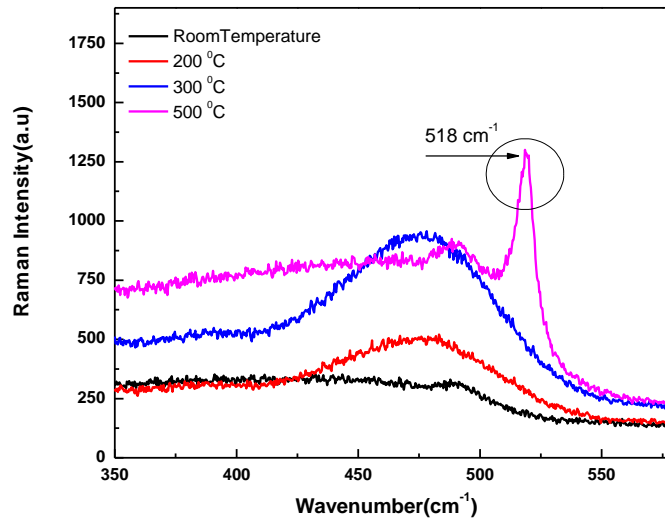


Figure 4.1-2: Raman shift spectra of a-Si films deposited at four different temperatures.

To achieving higher band gap a-Si films hydrogen is needed to be involved in the chamber during deposition instead of high temperature deposition processing. The

following section is related to the studies about hydrogenated a-Si:H films by RF magnetron sputtering.

## **4.2 Hydrogenated Amorphous Silicon Films Deposited by RF Magnetron Sputtering Technique**

Many studies showed that hydrogen has a very important role during the formation of the hydrogenated amorphous silicon (a-Si:H) film. It was demonstrated that hydrogen incorporation into sputtered a-Si:H reduces number of defects [65]. It is also found that hydrogen removal from SiH<sub>4</sub> plasma deposited a-Si:H films increase the defect density [66]. Electrical and optical properties of a-Si:H thin films mainly depend on hydrogen incorporation in the film and passivation of dangling bonds. Hydrogen gas was introduced into the sputtering chamber to incorporate hydrogen into the film during the sputtering process.

In this section, the study of the hydrogenated amorphous silicon (a-Si:H) film deposited by RF magnetron sputtering with argon and hydrogen gas mixture plasma is represented.

### **4.2.1 Experimental**

n-type doped Si targets ( $\rho < 0.1 \Omega \cdot \text{cm}$ ) was sputtered onto <100> Si wafers and quartz substrate in an atmosphere of argon and hydrogen. The effect of H<sub>2</sub> flow rate, RF power level and substrate temperature ( $T_s$ ) on deposited film properties was analyzed. During the deposition, chamber pressure was kept constant at 4 mTorr while the base pressure was about  $10^{-6}$  Torr. Three series of a-Si:H films with thicknesses of ~200 nm were deposited at an RF power of 100 W and 200 W. For the first series an RF power of 100 W was maintained during deposition and H<sub>2</sub> flow rate in the gas mixture was varied to 5 to 10 sccm. The second set of sample was deposited at a higher power of 200 W with H<sub>2</sub> flow rate of 10 and 15 sccm in the gas mixture. For both first and

second set of samples the substrate temperature was kept constant at  $\sim 30^{\circ}\text{C}$ . For the third series, the RF power was maintained at 200 W. During deposition,  $\text{H}_2$  flow rate was kept constant at 10sccm while the substrate temperature was varied  $200^{\circ}\text{C}$ ,  $300^{\circ}\text{C}$  and  $400^{\circ}\text{C}$  respectively. For each series films were deposited on silicon and quartz substrates. Samples with Si substrate were used to investigate Si-H bonds using FTIR spectrometry in the range of  $400\text{--}4000\text{ cm}^{-1}$ . Films grown on quartz substrates were used for the optical transmission measurements by means of UV-Visible spectrometer in the wavelength range from 200 to 1000 nm. A Dektak profilometer was used to determine the thickness of the deposited films. Raman spectroscopy technique was applied to characterize the a-Si:H films.

## 4.2.2 Results and Discussion

### 4.2.2.1 FTIR and Hydrogen Bonding

FTIR spectroscopy was used to confirm the existence of hydrogen in the deposited films. Figure 4.2-1 represents FTIR spectra of films deposited with hydrogen flow in the deposition chamber.

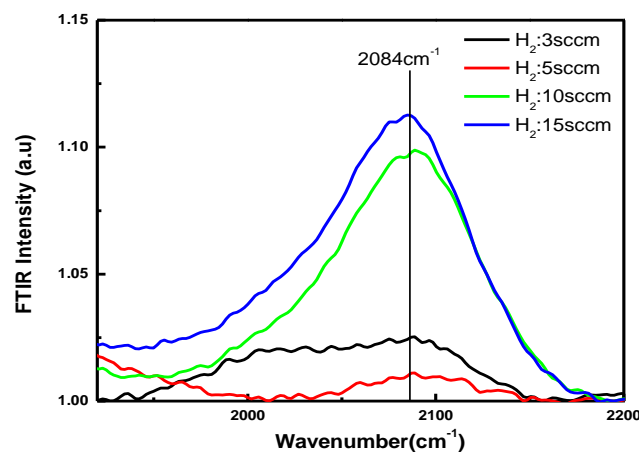


Figure 4.2-1: FTIR spectra of films deposited under the hydrogen flow rate of 3 sccm for 150 W DC power, 5 sccm for 100W RF power and 10sccm,15 sccm for 200 W RF power.

From Figure 4.2-1, it can be observed that the peak around 2000-2100  $\text{cm}^{-1}$  corresponding to the Si-H stretching vibration modes and the peak at 2080  $\text{cm}^{-1}$  confirms the presence of hydrogen in the films [67]. It can be easily seen that FTIR intensity increase by the increasing  $\text{H}_2$  flow rate. However from the figure it can be seen that Si-H<sub>2</sub> bonding is dominant which means a very high defective layer. It should be noted that DC power cannot be used for high hydrogen flow rates due to instability of the plasma in our sputtering system.

#### 4.2.2.2 Raman Spectroscopy Results

Raman spectroscopy technique was applied to characterize the Si-Si bonds in a-Si:H films and to determine the crystallinity of the film. The microstructures of the films were investigated for deposition powers of 100 and 200 W. Since the films were deposited under Ar and  $\text{H}_2$  plasma it was important to confirm that the microstructure of the deposited films showed no trace of micro-crystallites at the power levels being used. Raman spectroscopy results, Figure 4.2-2, showed no trace of micro-crystallites at the power levels being used.

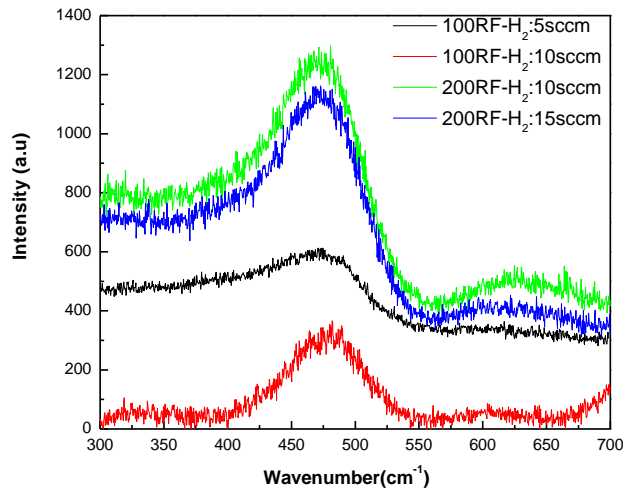


Figure 4.2-2: The Raman spectra of the samples deposited at RF power of 100 W and 200 W with the  $\text{H}_2$  flow rate of 5, 10 and 15 sccm.

Both sets of the samples deposited at room temperature with 100 W and 200 W showed a spectrum with only a broad peak around  $480\text{ cm}^{-1}$  indicates an amorphous structure. There were no peak around  $515\text{-}520\text{ cm}^{-1}$  for a crystalline phase within the amorphous matrix, therefore a higher power of 200 W can also be suitable for high rate deposition of a-Si:H film. The deposition rate was nearly doubled with power increased from 100 W to 200 W. However, the spectrum of the films deposited at RF power of 200 W with 10 sccm hydrogen flow rate and substrate temperature of  $200\text{ }^{\circ}\text{C}$  to  $400\text{ }^{\circ}\text{C}$  presents an additional peak around  $515\text{ cm}^{-1}$ . This results show that the crystallization is induced when the substrate is heated during the deposition.

However, Raman spectra of the third series that is; RF 200 W and hydrogen flow rate was fixed at 10 sccm, substrate temperature of  $200$  to  $400\text{ }^{\circ}\text{C}$ ; showed an additional peak around  $515\text{ cm}^{-1}$  along with the usual amorphous silicon peak at  $480\text{ cm}^{-1}$ . Figure 4.2-3 shows that the crystallization is induced when the substrate is heated during the deposition.

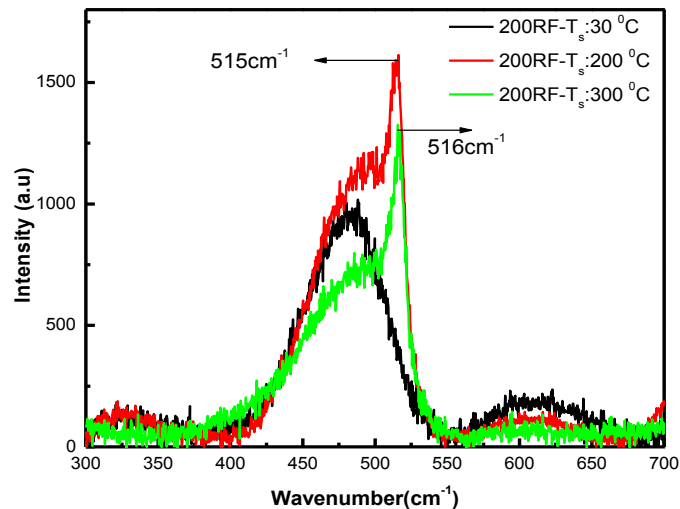


Figure 4.2-3: The Raman spectra of the samples deposited at RF power of 200 W with the  $\text{H}_2$  flow rate of 10 sccm with varying substrate temperatures of 30, 200 and  $300\text{ }^{\circ}\text{C}$ .

### 4.2.2.3 Transmission Spectra and Band Gap

The transmission experiments were performed on these films deposited at different substrate temperatures and different hydrogen flow rates by UV-Visible spectrometer. The band gaps of the deposited films were calculated from the transmission spectra of the films and listed in Table 4. The band gap increased from 1.4 eV to about 1.9 eV with the addition of hydrogen to the sputtering chamber. However, the band gap reduced from 1.8 eV to 1.4 eV while substrate temperatures increase (from 200 °C to 400 °C). The drop in the band gap is caused by the reduced hydrogen content in the films at higher deposition temperature.

Table 4: The band gap of a-Si:H films deposited at different RF power and temperature.

| Power (W) | H <sub>2</sub> Flow Rate (sccm) | T <sub>s</sub> (°C) | Deposition Rate (nm/min) | Band Gap (eV) |
|-----------|---------------------------------|---------------------|--------------------------|---------------|
| 150 DC    | 3                               | 30                  | 2.0                      | 1.79          |
| 100 RF    | 5                               | 30                  | 0.60                     | 1.87          |
| 200RF     | 10                              | 30                  | 1.27                     | 1.85          |
| 200RF     | 10                              | 200                 | 1.23                     | 1.62          |
| 200RF     | 10                              | 300                 | 1.22                     | 1.68          |
| 200RF     | 10                              | 400                 | 1.23                     | 1.44          |

### 4.2.2.4 Electrical Measurements

200 nm of a-Si:H films were deposited on glass substrates by using the same Si target and approximately 200 nm of metal was evaporated through a mask for electrical contacts. The mask used for these contacts has 0.5 cm in length and 2 mm in width. The spacing between the bars was 0.5 cm. We obtained a resistivity value in the order of  $10^4$ - $10^5$  Ω.cm. Table 5 shows some resistance and resistivity values of a-Si:H deposited

by different sputtering types. It is clear that the resistivity values are very high, indicating that the deposited layers are not properly doped.

Table 5: The resistivity values of two samples deposited at two different power and H<sub>2</sub> flow rate

| <b>Power</b> | <b>H<sub>2</sub> (sccm)</b> | <b><math>\rho</math> (<math>\Omega</math>.cm)</b> |
|--------------|-----------------------------|---|
| 200W (RF)    | 10                          | $2.02 \times 10^5$                                |
| 150W (DC)    | 3                           | $2.74 \times 10^4$                                |

### 4.3 SHJ Solar Cells by Magnetron Sputtering

After achieving progress in a-Si:H films by sputtering technique, we will exploit these films for solar cell production. In this section SHJ solar cells fabricated by magnetron sputtering are examined.

All the SHJ solar cells were formed by fabrication of thin a-Si:H(n) layer deposited using highly doped n-type Si targets ( $\rho < 0.1 \Omega$ .cm ) on 300  $\mu$ m thick p-type c-Si wafer. As summarized in the previous section the optimum conditions for emitter a-Si:H(n) layer was decided as 200 W power and the gas mixture of Ar: 20 sccm and H<sub>2</sub>:10 sccm at two different substrate temperature : room temperature and 200 °C. The front Al grids were evaporated with the thickness of 200 nm and the width of the bus bar 1 mm. The back surface of wafer covered with Al for the back contact. 1 cm<sup>2</sup> area solar cells parameters were evaluated using a halogen lamp with a power of ~30 mW/cm<sup>2</sup>.

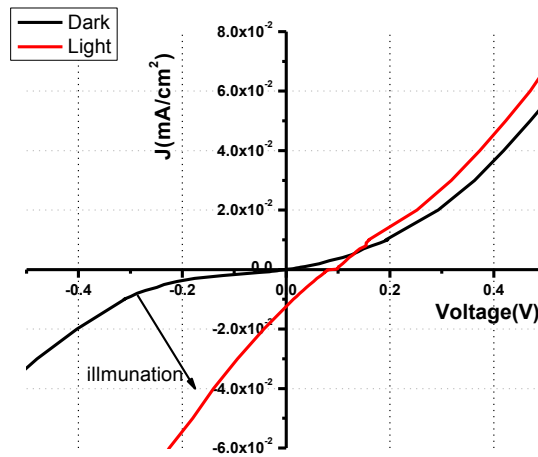


Figure 4.3-1: J-V characteristics for a-Si:H(n)/c-Si(p) heterojunction and the effect of illumination.

The a-Si:H(n)/c-Si(p) devices exhibited very little rectification properties as shown in Figure 4.3-1.

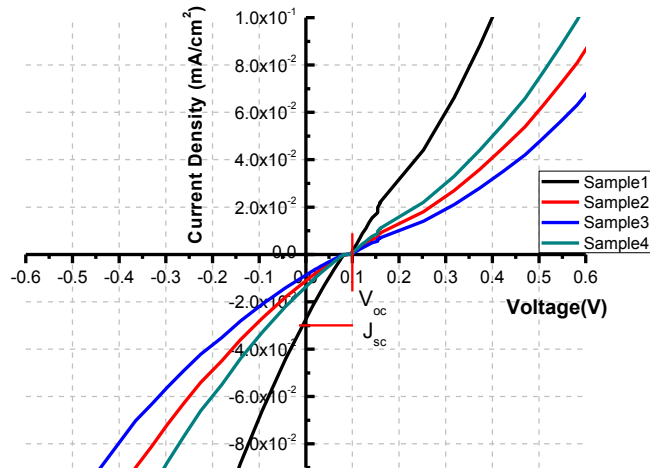


Figure 4.3-2: Illuminated J-V measurements of samples deposited by magnetron sputtering.

Figure 4.3-2 shows the illuminated I-V curve of the four samples; sample 2 and sample 4 were deposited at the temperature of 200 °C while the others were deposited at the room temperature. From Figure 4.3-2 it can be seen that we achieved very poor SHJ solar cells with low  $J_{sc}$  (0.02 mA/cm<sup>2</sup>) and  $V_{oc}$  (~0.1 V) values at both deposition temperatures. The obtained J-V curves showed a very high series resistance ( $R_s > 2000 \Omega \cdot \text{cm}^2$ ). The high resistance of the device is mainly due to high resistivity of the bulk a-Si:H(n) as summarized in Table 5. The high  $R_s$  cause a significant loss in the current flow even though the photo generated charges are created. The low  $V_{oc}$  indicates both poor interface quality and insufficient band bending. In p-n junctions the band bending mainly depends on the doping concentration in Si wafer and in bulk amorphous silicon layer. It appears that the dopant incorporation into the right location has not been achieved using pre-doped targets. One possible solution of this problem is to use a separate target for doping.

#### 4.4 Conclusion

In this chapter the results on the a-Si:H films and SHJ solar cells deposited via magnetron sputtering technique are given. Although we could achieve to obtain high band gap amorphous thin films, they were not suitable for our solar cell studies. This was mainly due to high resistivity of the a-Si:H film which indicates that deposited films are not sufficiently doped. The insufficient doping in a-Si:H causes a poor p-n junction with low rectification and hence low  $V_{oc}$ . Because of the use of pre-doped solid Si targets, it was not easy to control doping in a-Si:H films. Although dopant atoms are deposited into the film, a highly doped target does not necessarily leads to incorporation of dopant atoms into substitutional sites, which is a requirement for the p-n junction formation for solar cell fabrication. Besides sputtering, the widely used method is PECVD. In the next two chapters reader will find detailed study about SHJ solar cells deposited by PECVD method.

## CHAPTER 5

### a-Si:H (n)/ c-Si (p) SOLAR CELLS

#### 5.1 Introduction

Silicon heterojunction (SHJ) solar cells enable high open-circuit voltage ( $V_{oc}$ ) and fill factor (FF) with relatively easy processing steps at low temperatures ( $<300\text{ }^{\circ}\text{C}$ ). In p-type SHJ cells (a-Si:H(n)/c-Si(p)) the p-n junction is formed by the deposition of phosphorus doped a-Si:H layer on the front side of p type c-Si wafer. The main purpose of the emitter a-Si:H(n) layer is to create a band bending to separate photo-generated charges while passivating dangling bonds on the c-Si surface. A strong band bending leads to a decrease in the recombination velocity at the c-Si surface. Additionally, a sharp band bending with higher Fermi-level splitting leads to a higher  $V_{oc}$ .

The key point for high performance SHJ solar cells is to minimize the generated carrier recombination in the structure. The recombination occurs mainly because of the defect states in the solar cell and it severely reduces efficiency. The defect states can be due to low bulk quality of c-Si wafer, poor electrical properties and microstructure of a-Si:H emitter layer. Additionally, lower defect states between the interfaces of emitter-wafer, TCO-emitter interface, and wafer-back contacts have crucial importance for high  $V_{oc}$  [68]. The recombination possibilities for c-Si(p) surface and a-Si:H(n) film are shown in Figure 5.1-1.

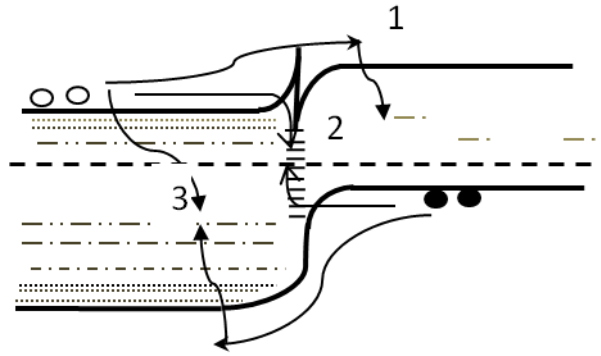


Figure 5.1-1: Band diagram of a-Si:H/c-Si heterojunction and possible recombination paths due to : defect states in the c-Si (1), defects at Si:H/c-Si interface (2), disorder in the a-Si:H. Defects states are indicated by dash lines.

When the interface between emitter and c-Si has high number of defect centers, photo generated carriers recombine and hence  $V_{oc}$  drops. If the carriers overcome the junction potential and reach the doped amorphous layer the disorder in the a-Si:H causes high amount of interface states and thus increased effective recombination probability [69]. High defective a-Si:H(n) layer obstructs the charge carriers from reaching the front contact due to recombination in the a-Si:H [70]. For a SHJ, the challenge is to keep the density of defects states, at the a-Si:H/c-Si interface and in the a-Si:H layer, as low as possible to prevent recombination losses. A high quality a-Si:H emitter layer also requires sufficient electrical contact and interface properties with the ITO to obtain higher FF.

In this section, a-Si:H(n)/c-Si(p) solar cell performance is investigated with particular emphasis on the effect of plasma process parameters of emitter a-Si:H(n). We focused on optimization of a-Si:H(n) as an emitter on p-type SHJ thin films by probing its conductivity, band gap, and hydrogen bonding profile.

The film properties are mainly affected by the choice of deposition parameters. In the PECVD technique the major parameters affecting electrical, optical and micro structural characteristics of a-Si:H films are doping gas flow rate, deposition temperature and plasma power. A systematic study of various PECVD processing parameters were carried out to optimize the a-Si:H(n) emitter properties for the SHJ

cell applications. The cells analyzed in this chapter have no intrinsic layers between the c-Si wafer and the doped a-Si:H layers. This increases the recombination at the a-Si:H/c-Si interface and leads to considerably lower  $V_{oc}$ .

## 5.2 Experimental

SHJ solar cells were fabricated in a multi-chamber DC PECVD system; with different emitter deposition conditions on double side polished 300  $\mu\text{m}$  thick p-type c-Si (100) float zone (FZ) wafers with resistivity of  $\sim 2 \Omega\cdot\text{cm}$ . The solar cell structure was Ni-Al Grids / ITO/ (10nm) a-Si:H (n) / (300  $\mu\text{m}$ ) c-Si (p) / (10nm) a-Si:H (p) / Al as shown in Figure 5.2-1.

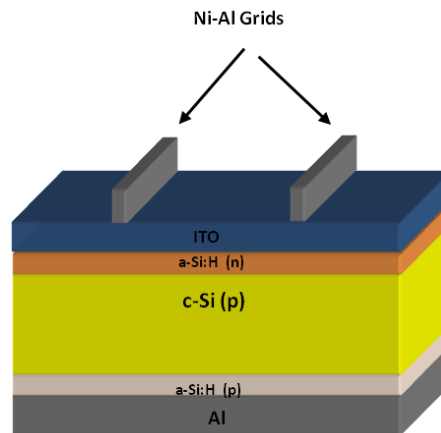


Figure 5.2-1: The diagram of Ni-Al Grids/ ITO/ a-Si:H (n) / c-Si (p) / a-Si:H (p) / Al

Prior to the deposition of the a-Si:H layers, the wafers were cleaned with acetone, isopropanol alcohol (IPA), and de-ionized (DI) water. These sequences were followed by piranha etching and HF dip before loading the wafers in to the system (Cleaning steps are explained in detailed in Chapter 3).

Due to the comparatively low conductivity of doped a-Si:H, a transparent conductive oxide (TCO) layer, also working as an anti-reflection coating, on top of the a-Si:H(n) emitter is essential. Sputtered indium tin oxide ( $\text{In}_2\text{O}_3$ : Sn) was used for the

TCO, and Ni-Al grids were evaporated for the front contact of the cell. The a-Si:H(p) layer was deposited on the rear side of c-Si(p) to obtain the back surface field, and Al is evaporated by electron beam deposition to form the rear contact.

To measure thickness and the band gap of the a-Si:H(n) films transmission and reflection measurements (T&R) were applied. The Quasi-Steady State Photo Conductance (QSSPC) decay method [71] was used to evaluate the passivation quality of the wafer. The hydrogen bonding configuration was evaluated by FTIR spectrometry. The microstructure factor ( $R_{MF}$ ) was calculated for all a-Si:H series.  $R_{MF}$  is the ratio of integrated absorbance of the di-hydride mode (Si-H<sub>2</sub>: peak at the 2090 cm<sup>-1</sup>) over the mono-hydride (Si-H: peak at the 2000 cm<sup>-1</sup>) plus di-hydride modes in the bulk,  $R_{MF} = I [\text{Di-Hydride}] / (I [\text{Di-Hydride}] + I [\text{Mono-Hydride}])$  [72].

The cell performance with an active area of 0.56 cm<sup>2</sup> was evaluated under the AM1.5G (100 mW/cm<sup>2</sup>) condition. Samples for FTIR analysis were deposited on c-Si wafers while those for optical and electrical measurements were deposited on glass.

In all cells, the rear a-Si:H(p), ITO, front and back contact properties and deposition conditions were held constant while the a-Si:H(n) layer deposition conditions were changed by varying PH<sub>3</sub> flow rate, deposition temperature ( $T_s$ ), plasma current, hydrogen dilution, and a-Si:H(n) thickness. This mainly leads to focus on the effect of depositions parameters of the a-Si:H(n) emitter layers.

## 5.3 Results and Discussion

### 5.3.1 Effect of PH<sub>3</sub> Gases Flow Rate

The n-type doped a-Si:H film is formed by introducing phosphine (PH<sub>3</sub>) in to the deposition chamber during glow discharge of SiH<sub>4</sub> and H<sub>2</sub> gas mixture. The electronic structure and the Fermi level of a-Si:H film are changed by substitutional impurity doping in the gas phase. For SHJ solar cells, the main purpose of the highly doped amorphous emitter is to build up a high band bending [73]. By increasing doping

concentration, the Fermi level of the film can be shifted with respect to the band edges, and hence, the conductivity increases. However, increasing doping concentration also increases the defect density in doped a-Si:H films and reduces passivation quality. On the other hand, the low doping concentration can cause higher contact resistance with TCO or metal contacts which affects the series resistance and hence, FF of heterojunction solar cells [74]. Thus, it is essential to control doping concentration and PH<sub>3</sub> flow during deposition of the amorphous layer [73].

This subsection of the chapter is dedicated to the investigation of optimum gas flow for a-Si:H(n) as an emitter layer for p-type SHJ. The flow rate of the PH<sub>3</sub> was varied between 2-20 sccm (sccm: standard cubic centimeters per minute) at fixed SiH<sub>4</sub> flow (20 sccm) and the thickness of n-type a-Si:H films were about 10 nm while T<sub>s</sub>=200 °C and DC=123 mA. Table 6 summarizes the conductivity, microstructure factor R<sub>MF</sub>, and band gap of the a-Si:H(n) layer at different PH<sub>3</sub> flow rates.

Table 6: Conductivity, R<sub>MF</sub>, band gap and lifetime of a-Si:H films depending on PH<sub>3</sub> flow rate.

| PH <sub>3</sub> Flow Rate (sccm) | Conductivity (Ω.cm) <sup>-1</sup> | R <sub>MF</sub> | Band Gap (eV) | Lifetime (μsec) |
|----------------------------------|-----------------------------------|-----------------|---------------|-----------------|
| 2                                | 10 x 10 <sup>-3</sup>             | 0.19            | 1.87          | 240             |
| 5                                | 14 x 10 <sup>-3</sup>             | 0.28            | 1.80          | 130             |
| 10                               | 61 x 10 <sup>-3</sup>             | 0.26            | 1.87          | 85              |
| 15                               | 67 x 10 <sup>-3</sup>             | 0.32            | 1.87          | 71              |
| 20                               | 97 x 10 <sup>-3</sup>             | 0.39            | 1.88          | 71              |

As seen from Table 6, band gap shows almost no change for different PH<sub>3</sub> flow rates while the conductivity increases by increasing PH<sub>3</sub> flow rate. In Table 6, a-Si:H(n) films with a high lifetime obtained by lower PH<sub>3</sub> flow rates can suggest a high-quality surface passivation. However, the low dark conductivity yields more defect states inside the a-Si:H(n) film, which causes it to be too resistive to conduct minority carriers and further are responsible for a high series resistance which is a trade-off between the series resistance and lifetime. High effective lifetime does not ensure a high SHJ solar cell efficiency because of the low fill factor (FF). A high quality emitter layer should have high conductivity.

The solar cells performances with different emitter layer PH<sub>3</sub> flow rate are summarized in Table 7. PH<sub>3</sub> flows of 2-4 sccm were not chosen as an emitter layer gas flow due to their low conductivity. We achieved higher FF and V<sub>oc</sub> by increasing PH<sub>3</sub> flow rate which implies that the improvement in the band offset between a-Si:H and c-Si. The FF increased from 53% to 64% by increasing the flow from 5 to 10 sccm. This can be evidence for suggesting that a higher doping concentration layer forms a better abrupt junction and ohmic contact with the ITO.

Table 7: Solar cell parameters with different emitter layer PH<sub>3</sub> gas flow rate and R<sub>s</sub> values calculated from dV/dJ vs 1/J curve.

| PH <sub>3</sub> (sccm) | V <sub>oc</sub> (V) | J <sub>sc</sub> (mA/cm <sup>2</sup> ) | FF (%) | Eff. (%) | R <sub>s</sub> (Ω.cm <sup>2</sup> ) |
|------------------------|---------------------|---------------------------------------|--------|----------|-------------------------------------|
| 5                      | 0.552               | 31.2                                  | 53.0   | 9.0      | 5.0                                 |
| 10                     | 0.594               | 32.2                                  | 64.1   | 12.3     | 2.4                                 |
| 20                     | 0.599               | 31.4                                  | 64.3   | 12.0     | 2.5                                 |

In Figure 5.3-1, the J-V characteristics of the samples under illumination are shown. The J-V curve shows that emitter layer deposited at higher doping eliminates “S” shaped characteristics and improves 10 sccm and 20 sccm during a-Si:H(n) deposition can be considered efficient FF from 53% to 64% while reducing R<sub>s</sub>. Consequently, the flow rate between for the acceptable doping concentration of a-Si:H(n).

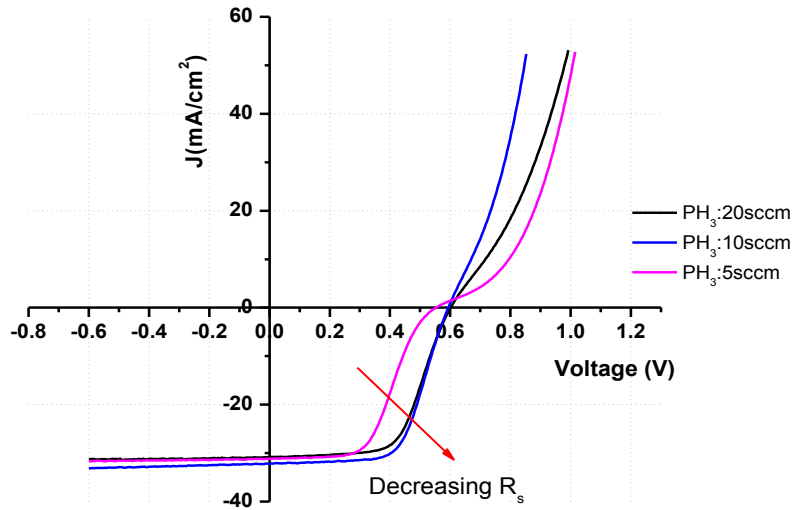


Figure 5.3-1: JV curves of the devices summarized in Table 2. While  $R_s$  increase the J-V curve becomes more “S” shape.

### 5.3.2 Temperature Effect

In order to investigate the temperature effect on the optical, electrical, and structural properties of a-Si:H films, four different substrates (deposition) temperatures ( $T_s$ : 175, 200, 250, 300 °C) were used.

Table 8: Band gap, microstructure factor  $R_{MF}$ , and conductivity results by varying deposition temperature.

| $T_s$ (°C) | a-Si:H(n) Thickness (nm) | $E_g$ (eV) | $R_{MF}$ | Conductivity $\sigma$ ( $\Omega.cm$ ) <sup>-1</sup> |
|------------|--------------------------|------------|----------|---|
| 175        | 10                       | 1.86       | 0.86     | $4.2 \times 10^{-3}$                                |
| 200        | 12                       | 1.85       | 0.81     | $9.6 \times 10^{-3}$                                |
| 250        | 14                       | 1.82       | 0.46     | $1.1 \times 10^{-2}$                                |
| 300        | 13                       | 1.76       | 0.16     | $2.4 \times 10^{-2}$                                |

Table 8 shows that changing  $T_s$  has a substantial effect on film structure, conductivity,  $R_{MF}$ , and band gap. The microstructure factor,  $R_{MF}$ , decreases from 0.85 to 0.16 by increasing the temperature from 175 °C to 300 °C. This indicates a transition from dihydride bonding to predominantly mono-hydride, as shown in the FTIR spectra in Figure 5.3-2. Also, note that the conductivity increases with substrate temperature. This may be related to the microstructure since the mechanism of doping in a-Si:H involves creating simultaneous dangling bond defects. Reducing the dangling bond density via improved H-bonding would increase the free carriers available for conduction.

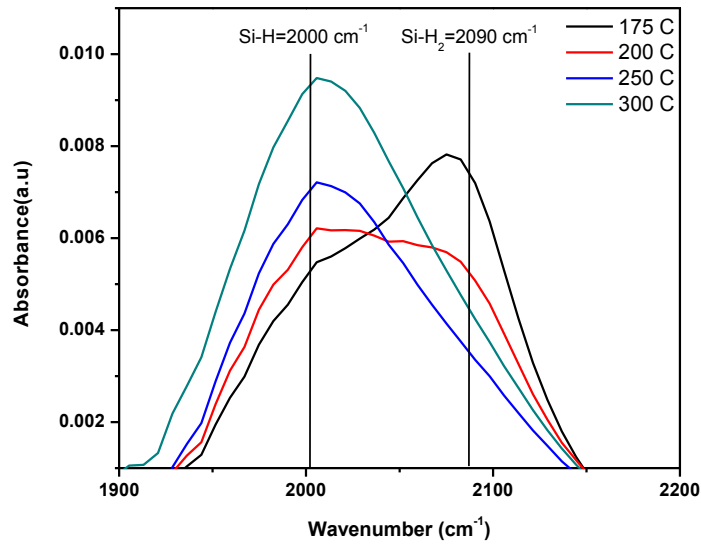


Figure 5.3-2: FTIR spectra of a-Si:H(n) films at different deposition temperatures at 123 mA.

In order to evaluate the effect of emitter layer deposition temperature, two different a-Si:H(n) layer deposition temperatures (200 and 250 °C) were used for a-Si:H/c-Si solar cell fabrication. It was observed that the reduction of  $R_{MF}$  did not lead to higher  $V_{oc}$  for lower defect densities in emitter layer. However, the FF of the cells improved significantly from 70 to 76 % with deposition temperature, while  $V_{oc}$  is still in the range of ~0.600 V (Figure 5.3-3).

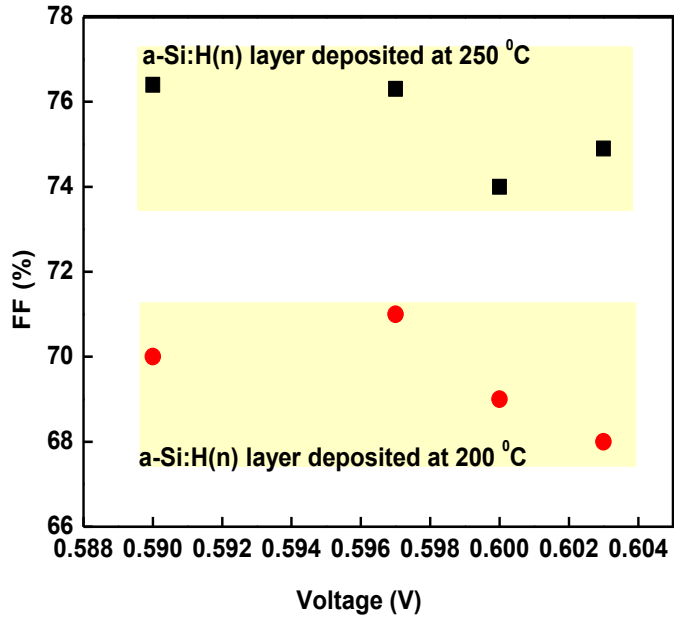


Figure 5.3-3: FF vs  $V_{oc}$  of four SHJ cells with emitter layers deposited at 200 and 250 °C. Their  $V_{oc}$  values vary around the same values.

The FF of a solar cell primarily depends on parasitic losses, such as series resistance or blocking contacts, as well as recombination losses at the wafer surface and doped layers [75]. Therefore we focused on p-n junction properties and series resistance ( $R_s$ ) to understand the reasons for the higher FF on the higher temperature emitter a-Si:H(n) layers.  $R_s$  and ideality factor  $n$  of the samples are evaluated by analyzing  $dV/dJ$  vs.  $1/J$  plots from the J-V curves as explained in Chapter 3. Figure 5.3-4 shows the  $dV/dJ$  vs.  $1/J$  graph for cells with FF=67% (200 °C) and 76% (250 °C). The lumped  $R_s$  and ideality factor  $n$  were evaluated from a linear fit to the data in Figure 5.3-4 and found to be  $R_s$ : 1.06  $\Omega\cdot\text{cm}^2$ ,  $n$ : 1.24 and  $R_s$ : 2.35  $\Omega\cdot\text{cm}^2$ ,  $n$ : 1.12 for deposition temperatures at 250 and 200 °C, respectively. Though the ideality factors are similar,  $R_s$  shows a significant decrease for the 250 °C case. Current blocking behavior for the emitter deposited at 200 °C is clearly evident from the large peak. Thus, we can conclude that the lower FF at 200 °C is due to both higher  $R_s$  and the blocking contact.

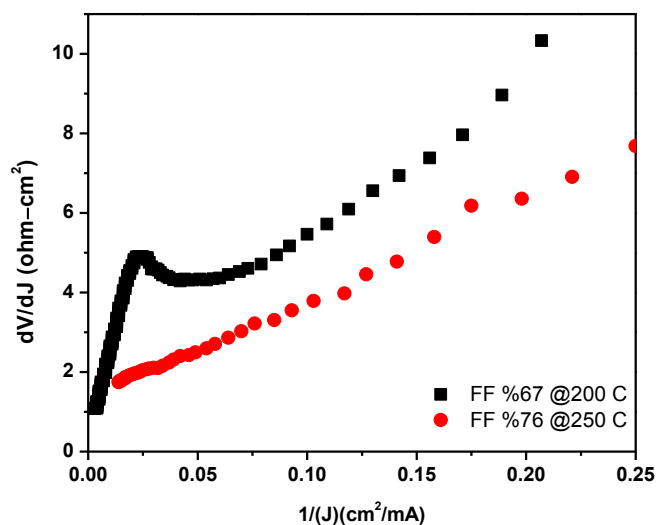


Figure 5.3-4: Plot of  $dV/dJ$  vs.  $1/J$  curves for the solar cells whose emitter layers are deposited at 200 °C and 250 °C.

The dominant sources of a solar cell's  $R_s$  values are contact resistance and lateral conductions in the emitter. Therefore to reduce  $R_s$ , high conductivity in the emitter layer and low contact resistance between front and back layers are essential.

In Table 8, it is shown that the conductivity of the films deposited at 200 and 250 °C do not vary significantly. This suggests that the difference in  $R_s$  of the solar cells is due to the contact resistance between the doped emitter (rear) layers and/or ITO (Al). To investigate front and back contact properties separately, we prepared test structures. First, a Al Grids / a-Si:H (p) / c-Si (p) / a-Si:H (p) /Al structure was prepared to ascertain the back contact properties between a-Si:H(p) and Al. Next, the impact of deposition temperatures on contact properties between the emitter layer and ITO was investigated by using ITO/ a-Si:H (n) /c-Si (n) / a-Si:H (n) /Al test structures. Ideally, both structures should give linear J-V curves with very low resistance. Figure 5.3-5 and Figure 5.3-6 show the contact properties of back a-Si:H(p) and emitter a-Si:H(n) layers with Al and ITO respectively.

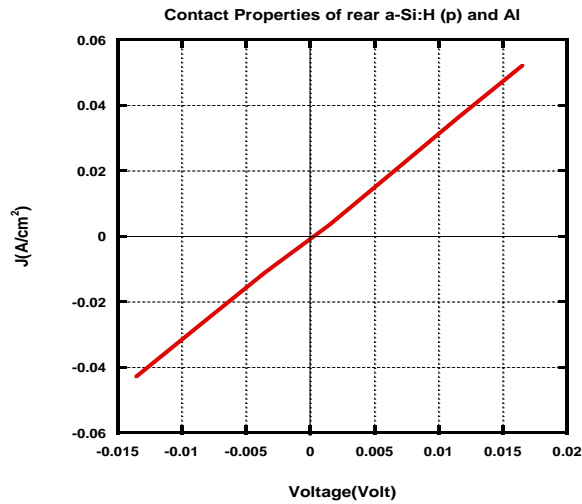


Figure 5.3-5: J-V curve of Al-Ni / a-Si:H(p) / c-Si(p) / a-Si:H (p) / Al.

Figure 5.3-5 shows that the ohmic characteristics between a-Si:H(p) back layer and Al is linear and very adequate for carrier transport with the lumped series resistance of  $0.32 \Omega \cdot \text{cm}^2$ . In contrast, Figure 5.3-6 shows that as n-layer deposition temperature increases from 175 to 250 °C, the contact between ITO and n-layer transitions from blocking and high resistance to nearly linear and low resistance. This is consistent with the increase in a-Si:H(n) layer conductivity with temperature presented in Table 8. Increasing temperature from 175 to 200 °C has little impact on contact properties.

Figure 5.3-6 provides evidence that the commonly observed ‘S-shape’ JV curve is at least partially due to a blocking contact between the ITO and n-layer as shown in Figure 5.3-4.

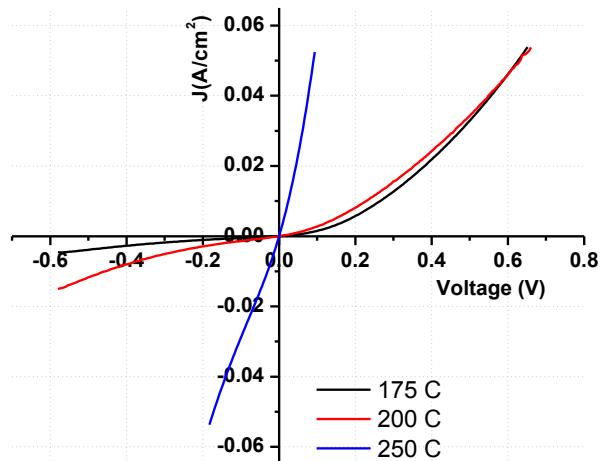


Figure 5.3-6: J-V curve of ITO/ a-Si:H(n) /c-Si(n)/ a-Si:H (n) /Al

### 5.3.3 DC Plasma Current Effect

The bias plasma voltage is another parameter which affects the deposition process and film properties of a-Si:H films. The study of plasma current, hence plasma power, is important to evaluate possible plasma damage on the c-Si wafer surfaces due to ion bombardment. High power leads to possible detrimental conditions for the a-Si:H/c-Si interface by high-energy ion bombardment in PECVD.

Five different DC plasma discharge currents (40, 60, 90, 123, and 150 mA) were applied to investigate the influence of discharge current (directly to power) on a-Si:H(n) films and solar cells. The investigated solar cells for plasma DC effect were fabricated with optimized doping  $\text{PH}_3$  gas flow of 10sccm and the temperature of 250 °C. In Table 9,  $E_g$  and  $R_{MF}$  values for DC current series are summarized.

Table 9: Properties of the thin a-Si:H(n) films, measured from T&R and FTIR for increasing DC plasma current.

| Plasma DC (mA) | $E_g$ (eV) | Growth Rate (nm/sec) | $R_{MF}$ | Conductivity $\sigma$ ( $\Omega.cm$ ) <sup>-1</sup> |
|----------------|------------|----------------------|----------|---|
| 40             | 1.86       | 1.20                 | 0.27     | --  |
| 60             | 1.87       | 1.18                 | 0.31     | $1.11 \times 10^{-2}$                               |
| 90             | 1.86       | 2.20                 | 0.29     |   |
| 123            | 1.86       | 2.40                 | 0.29     | $1.12 \times 10^{-2}$                               |
| 150            | 1.87       | 2.70                 | 0.30     |   |

Table 9 shows that changing plasma current does not show a substantial effect on  $R_{MF}$ , conductivity and band gap. The growth rate is increasing with power. Table 10 summarizes the p-Si SHJ solar cell parameters with three different plasma currents.

Table 10: p-type SHJ solar cell J-V parameters with different emitter layer deposition currents. The results are the averages of three different samples for each run.

| Plasma DC (mA) | FF(%) | $V_{oc}$ (V) | $J_{sc}$ (mA/cm <sup>2</sup> ) | Eff. (%) |
|----------------|-------|--------------|--------------------------------|----------|
| 60             | 75.0  | 0.603        | 30.2                           | 13.7     |
| 123            | 74.9  | 0.604        | 29.5                           | 13.3     |
| 150            | 73.3  | 0.598        | 29.0                           | 12.5     |

Studying the plasma current is important to obtain information about the plasma damage on the c-Si wafer surfaces. The J-V results show that the plasma current between the ranges of 60 - 150 mA does not cause significant difference on solar cell properties.  $V_{oc}$  does not vary with plasma current, showing no correlation with the ion damage. Figure 5.3-7 illustrates the best cell parameters obtained from the solar cells with different plasma power emitter layer deposition.

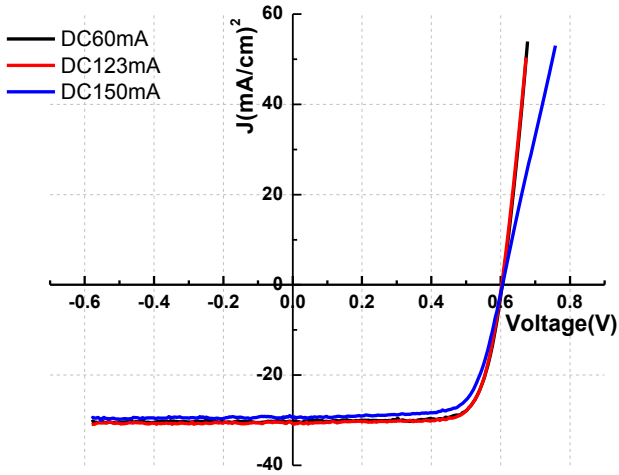


Figure 5.3-7: The JV curve of SHJ cells deposited at different DC plasma powers at the temperature of 250 °C.

### 5.3.4 Hydrogen Effect

This subsection presents the results of investigating the H<sub>2</sub> dilution effect by varying the ratios of hydrogen and the mixture of silane. The emitter a-Si:H(n) layers in these series were prepared by the optimum deposition conditions as explained in plasma DC of 123 mA, T<sub>s</sub>= 250 °C and SiH<sub>4</sub>/ PH<sub>3</sub> ratio is 2. The dilution ratio R = [H<sub>2</sub>] / [SiH<sub>4</sub>] was varied at the values of 6, 8, 13, 28.

Hydrogen dilution with silane gas is extensively used in a-Si:H deposition to assist the surface growth reactions. As known, a-Si films have a large concentration of dangling bonds because of their disorder network structure. The dangling bonds cause defect states that act as carrier traps and/or recombination centers that reduce the carrier lifetime and the mobility. For a-Si:H films, hydrogen passivates the dangling bonds, thereby reducing many traps and recombination centers and improving the performance and the stability of a-Si:H.

Hsiao et.al showed that at R=0, a well passivated surface with an abrupt a-Si:H/c-Si interface is obtained, but because of the insufficiency of the hydrogen, the defects in the a- Si:H film cannot be effectively passivated. By involving hydrogen during deposition the defects inside an a-Si:H film are passivated. However, as the amount of hydrogen is increasing, localized epitaxial occurs at the a-Si:H/c-Si interface, detrimentally affecting the transportation of the minority carriers [76]. Das et al. [77] showed the GIXRD (glancing incidence X-ray diffraction) pattern of intrinsic a-Si:H layers deposited with R=6 are amorphous, while intrinsic a-Si:H layer deposited with high R (R=40) has includes small size crystallite grains.

Table 11 shows the PV characteristic parameters including series resistance ( $R_s$ ) of SHJ solar cells as functions of R during the deposition of emitter a-Si:H (n) layers.

Table 11: PV characteristic parameters of SHJ solar cells with varying values of R.

| <b>R</b> | <b>FF(%)</b> | <b><math>V_{oc}(V)</math></b> | <b><math>J_{sc}(mA/cm^2)</math></b> | <b>Eff. (%)</b> | <b><math>R_s(\Omega.cm^2)</math></b> |
|----------|--------------|-------------------------------|-------------------------------------|-----------------|--------------------------------------|
| 6        | 75.0         | 0.603                         | 29.6                                | 13.4            | 1.35                                 |
| 8        | 72.2         | 0.595                         | 30.2                                | 13.1            | 1.20                                 |
| 13       | 71.4         | 0.596                         | 32.1                                | 13.7            | 1.50                                 |
| 28       | 68.9         | 0.586                         | 31.8                                | 13.0            | 1.25                                 |

From Table 11, it can be seen that both  $V_{oc}$  and FF decrease with R, while  $J_{sc}$  changes slightly. The emitter layer's band gaps were almost the same value of ~1.88 eV while increasing hydrogen. The low  $V_{oc}$  at high R might be related to the presence of a microcrystalline structure possibly mixed with the amorphous phase. To investigate the crystallinity in the emitter layers, their Raman spectra at different R values were analyzed as shown in Figure 5.3-8.

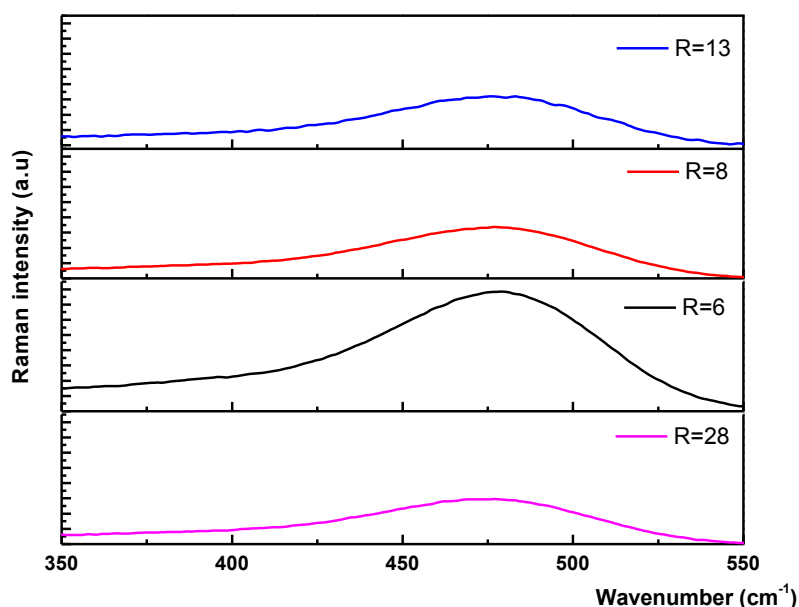


Figure 5.3-8: Raman spectra of emitter a-Si:H(n) layers deposited at different R values.

From Figure 5.3-8 it is seen that there is no peak corresponding to crystalline which is expected at around  $\sim 512 \text{ cm}^{-1}$ . There is only amorphous peak at around  $\sim 475 \text{ cm}^{-1}$ .

### 5.3.5 Thickness Effect:

Another important parameter for SHJ solar cells is the emitter layer thickness. Ideally, the emitter layer should be as thin as possible in order to avoid absorption losses especially in the blue and near-infrared region and recombination in bulk a-Si:H(n). The diffusion length of carriers in a-Si:H is shorter than c-Si due to the high defective structure. Furthermore, a-Si:H(n) has higher doping concentration, which is why the space charge region of the p-n junction is mainly on the crystalline silicon side. This leads to a very low electric field in the a-Si:H(n) side where there is only drift current [78]. The thickness of the highly doped a-Si:H(n) emitter layer should be optimized to obtain high photon collection. Emitter thickness was decided by

experimental results. Figure 5.3-9 demonstrates the influence of emitter thickness on the photovoltaic parameters of SHJ solar cells.

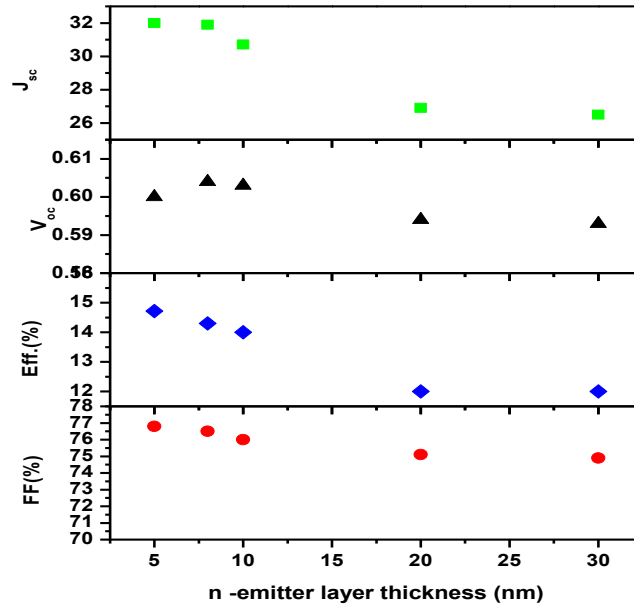


Figure 5.3-9: Solar cell parameters of p-type SHJ with varying emitter a-Si:H(n) thicknesses.

As can be seen from Figure 5.3-9 shows when the emitter thickness is increased, the open circuit voltage changed slightly, while the short circuit current is dramatically reduced. In order to understand the mechanism of losses responsible for reduction in  $J_{sc}$ , quantum efficiency (QE) measurements were performed. Figure 5.3-10 shows the measured external QE of SHJ solar cells with varying thicknesses. From this figure we see that, the loss in the blue region is mainly due to the absorption in the a-Si:H emitter layer, and increases with the increasing thickness.

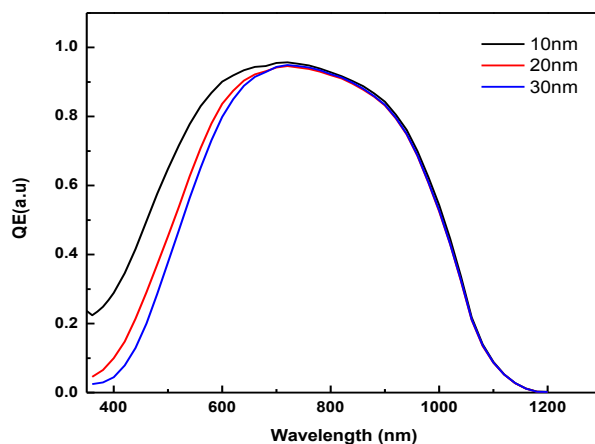


Figure 5.3-10: QE of SHJ with the emitter a-Si:H(n) thickness of 10, 20, and 30 nm.

Increasing emitter thickness with high amount of recombination centers hamper photo-generated carriers to reach the space charge region and resulting in the reduced blue region response and short circuit current. Fill factor decreases with increasing n layer thickness as well because of increasing series resistance with thickness [78]. Considering the short circuit current and the cell efficiencies, the emitter thickness should be around 5-10 nm.

## 5.4 Conclusion

In this chapter, plasma deposition parameters were studied for evaluating a-Si:H(n) quality as an emitter on p SHJ. It is observed that gas flow and temperature has significantly more effect than deposition current on optical and structural properties of a-Si:H(n) layer. The contact resistance needs to be low to get a good contact between ITO and emitter layer in SHJ solar cells. A correlation has been found between emitter deposition temperature and FF in a series of SHJ cells without a-Si:H(i) passivating layer. The optimal emitter a-Si:H(n) thickness was found to be ~10 nm at the temperature of 250 °C. This finally led to an efficiency of 14.1% and a  $V_{oc}$  of 603 mV

on polished p-type FZ c-Si wafers with a FF of 76%. From TEM picture (Figure 5.4-1) it can be observed that we achieved an abrupt interface between the c-Si/a-Si:H with no epitaxial growth.

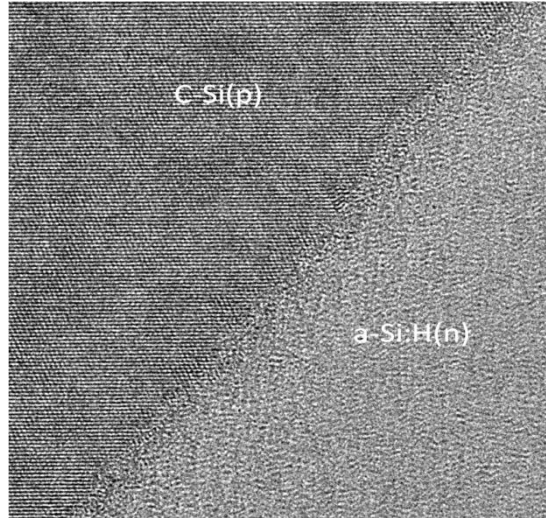


Figure 5.4-1: Schematic of SHJ solar cell and high-resolution transmission electron microscopic image of abrupt a-Si:H(n)/c-Si(p). The picture was taken from High resolution TEM located in Central Lab. at METU.

## CHAPTER 6

### **a-Si:H/ c-Si HETEROJUNCTION SOLAR CELLS WITH i-LAYER**

After obtaining an optimal emitter layer for the heterojunction solar cells (with the FF of ~75%), a thin buffer layer was incorporated on the front and the rear side of the hetero-structure to improve the c-Si surface passivation. Insertion of an a-Si:H(i) buffer layer exhibits higher  $V_{oc}$  (~650 mV) but with lower FF. High  $V_{oc}$  is due to the efficient surface passivation by the front/rear intrinsic layer, apparently due to its lower defect density compared to the n-doped emitter layer, which was also by the measurement of high effective lifetime ( $\tau_{eff}$  ~550  $\mu$ s) for photo-generated carriers.

We fabricated a-Si:H(n)/c-Si(p) heterojunction solar cells with different a-Si:H(i) layer deposition parameters and thicknesses in order to determine effects of a-Si:H layer on the performance of a-Si:H/c-Si solar cells. With increasing a-Si:H(i) layer thicknesses,  $V_{oc}$  increases slightly and  $J_{sc}$  reduces gradually. When i-layer thickness is greater than 15 nm FF reduces sharply due to increasing  $R_s$ . We achieved a solar cell efficiency of 14.1% using optimum a-Si:H layer thicknesses and deposition conditions without incorporating surface texture.

#### **6.1 Introduction**

In silicon heterojunction solar cells, suppression of a-Si:H/c-Si interface recombination and low emitter saturation current are the main factors for high cell performance. Inserting a thin intrinsic amorphous silicon (a-Si:H) buffer (i-layer) between doped layers and c-Si reduces interface recombination by minimizing defect states at the a-Si:H/c-Si interface [25]. In silicon heterojunction solar cells, suppression of a-Si:H/c-Si interface recombination and low emitter saturation current are the main factors for high cell performance. Inserting a thin intrinsic amorphous silicon (a-Si:H)

buffer (i-layer) between doped layers and c-Si reduces interface recombination by minimizing defect states at the a-Si:H/c-Si interface [25].

Structural and electronic properties of a-Si:H(i) layers have a significant role in interface quality. The properties of a-Si:H films vary strongly with the growth condition [79]. The main approach is to achieve optimal deposition condition for a-Si:H, which causes the least amount of c-Si surface damage while avoiding damaging epitaxial growth on the surface of the c-Si [80]. The deposition of a-Si:H film by PECVD can be visualized by four-layer model which the layers are defined as surface, bulk amorphous interface as basically shown in Figure 6.1-1. There can also be an epitaxial layer between the wafer and interface layer, which strongly depends on the deposition condition.

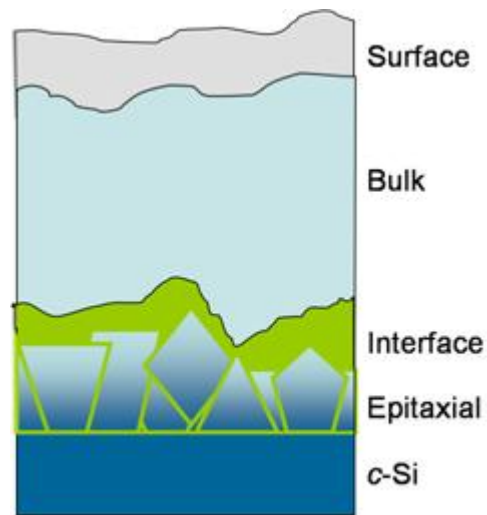


Figure 6.1-1: Illustration of a-Si:H deposited on c-Si surface as four layers [81].

Fujiwara et al. applied real-time in situ ellipsometry (SE) and infrared attenuated total reflection (ATR) spectroscopy methods to characterize the a-Si:H properties during growth process [82]. They observed that the interface is not an abrupt transition from crystal lattice to a homogenous bulk amorphous network. A low density and SiH<sub>2</sub> rich porous structure interface layer formed on c-Si wafer with a thickness of ~ 2 nm.

The large fraction of  $\text{SiH}_2$  indicates a poor network. Depending on the depth profiles of  $\text{SiH}_n$  ( $n=1, 2$ ) hydrogen contents obtained from ATR, the growth rate of interface layer is higher than the bulk a-Si:H film growth [82]. Here, bulk is the homogenous and purely amorphous network. After the formation of interface layer, the growth rate becomes almost stabilized and reaches the steady state conditions. Fujiwara et al. observed that the highest cell efficiency was obtained at the thickness where a-Si:H growth reaches a steady state after the defective interface layer formation. The top layer of bulk is a roughness layer which is formed due to exposure to air and has more Si-O bonding. There can also be an epitaxial layer (epi-Si) between interface and wafer. Epitaxial-Si (epi-Si) enhances the recombination at the interface and thus reduces the solar cell performance. Epitaxial layer can be identified by FTIR and TEM analysis [83]. The existence of an epitaxial layer is strongly dependent on deposition conditions such as deposition temperature, hydrogen dilution, plasma power and c-Si substrate crystal orientation [84], [25]. However, the epitaxial growth mechanism is not clear. Wolf et al. showed that the surface passivation quality of PECVD a-Si:H films improves when the a-Si:H/c-Si interface is abrupt [80].

The theme of this section is the establishment of a strategy required for achieving ideally passivate a-Si:H(i)/c-Si interfaces. For this purpose i-layer studies were divided in to two parts. In the first part a-Si:H(i) layers were investigated in terms of their passivation quality depending on the deposition parameters. In the second part, the thickness effect of i-layers on the performance of SHJ cells were analyzed.

## **6.2 Effect of Hydrogen Dilution Ratio and Plasma DC on a-Si:H(i) Layer and It's Passivation Quality Effect**

In this section, we studied the surface passivation quality of intrinsic a-Si:H(i) layers deposited with varying hydrogen dilution ratio at two different (60,123 mA) direct current (DC) PECVD processes on float zone (FZ) p-type single crystalline Si

(100) wafers. Here hydrogen dilution ratio,  $R$ , represents ratio of flow rate of  $H_2$  to flow rate of  $SiH_4$  ( $R = H_2/SiH_4$ ).

Other relevant parameters such as  $T_s$ , electrode spacing, and gas pressure were held constant at the optimum values for the deposition chamber. The surface passivation quality was evaluated by measuring effective minority carrier lifetime ( $\tau_{eff}$ ) using QSSPC (quasi steady state photo conductance) measurement method and Si-H bonding configuration in a-Si:H(i) films was examined by FTIR spectroscopy.

Prior to deposition of a-Si:H(i) layers, the Si wafers were cleaned by ultrasonic rinsing in acetone–methanol–deionized water. After the solvent cleaning, wafers were exposed to a mixture of  $H_2SO_4:H_2O_2$  (2:1) followed by 10% HF to remove oxide prior to a-Si:H deposition. (Cleaning procedure is explained in detail in chapter 3)

The a-Si:H i-layers (~10 nm) were deposited under  $R$  values of 1.5-2.5 at a constant substrate temperature (250 °C) and deposition pressure (1250 mTorr).

## 6.2.1 Results and Discussion

For a-Si:H deposition,  $H_2$  dilution is generally adopted to  $SiH_4$ . The  $H_2$  dilution leads to an improvement of the film quality due to the contribution of increasing the amount of  $SiH_3$  which is the dominant radical in forming a-Si:H film [85]. The  $H_2$  dilution also suppresses the formation of reactive (poly) silane radicals,  $(Si-H_2)_n$  cause high surface reactivity resulting to a high surface roughness and void rich structure [86].  $H_2$  diluted a-Si:H films also showed less photo-induced degradation [83].

However the incensement of the hydrogen on the growing surface gives rise to crystal growth. Thus, a certain threshold value for dilution ratio,  $R$ , should be defined for a-Si:H deposition. Hydrogen dilution during the deposition of a-Si:H (i) therefore causes variation on the material properties of the film. The investigation of the film properties in terms of Si-H bonding configuration is an important consideration about the variety.

To obtain information about the electronic surface passivation, properties of  $\tau_{\text{eff}}$  were evaluated. Figure 6.2-1 represents the  $\tau_{\text{eff}}$  as a function of R for 10 nm i-layers deposited on both sides of c-Si wafers by two different plasma DC (60 and 123 mA) at the temperature of 250 °C. The highest lifetime ( $\sim 1$  ms) value was achieved at the temperature of 250 °C.

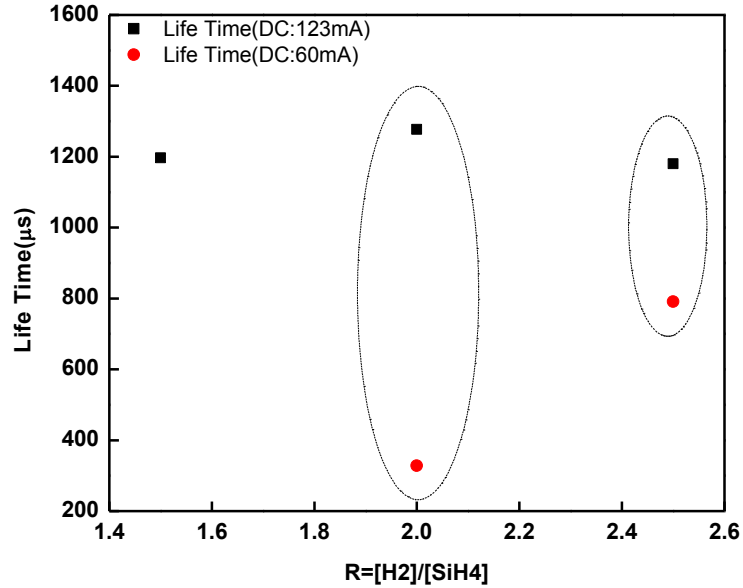


Figure 6.2-1: Effective minority life times,  $\tau_{\text{eff}}$ , of a-Si:H (i) / c-Si(p) / a-Si:H (i) structures as a function of R at the DC plasma of 60 and 123mA.

Here R was chosen in the range of 1.5-2.5 on regarding the study of Das et al. for the same deposition systems for n-type c-Si wafers [84]. They showed that  $\tau_{\text{eff}}$  at  $R < 2$  and  $R > 4$  is lower than the range of  $R = 2-4$ . From Figure 6.2-1,  $\tau_{\text{eff}}$  has a strong dependence to the plasma DC while it does not vary significantly with R in the range of 1.5-2.5. Figure 6.2-2 and Figure 6.2-3 illustrate the FTIR absorption spectra for  $R = 2.5$  and  $R = 2$ , respectively. From FTIR spectra Si-H bonding configuration is obtained: the peak at  $\sim 2090 \text{ cm}^{-1}$  originates from Si-H<sub>2</sub> stretching mode and the peak at  $\sim 2000 \text{ cm}^{-1}$  is due to Si-H stretching. Si-H<sub>2</sub> stretching modes are responsible for internal voids and this implies a porous structure and high defect density structure.

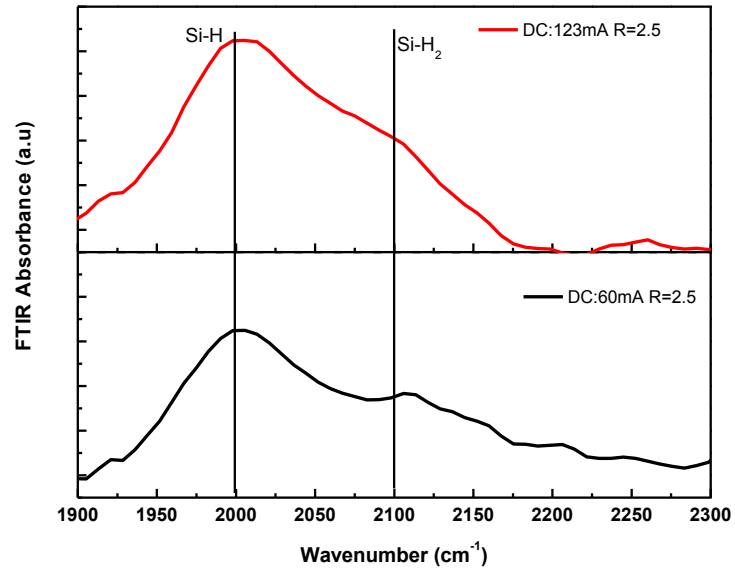


Figure 6.2-2: Comparison of FTIR spectra of 10 nm thick a-Si:H (i) layers grown by two different DC plasma process under  $R=2.5$ .

From Figure 6.2-2, as plasma DC is decreased di-hydride becomes more dominant, thus a-Si:H is expected more defective and has poor electrical quality. It is also in agreement with  $\tau_{\text{eff}}$  which is almost half the value at low plasma DC. At this condition we note that low life time correlates with the poor passivation quality seemingly due to higher Si-H<sub>2</sub> bonding i.e. large bulk defects.

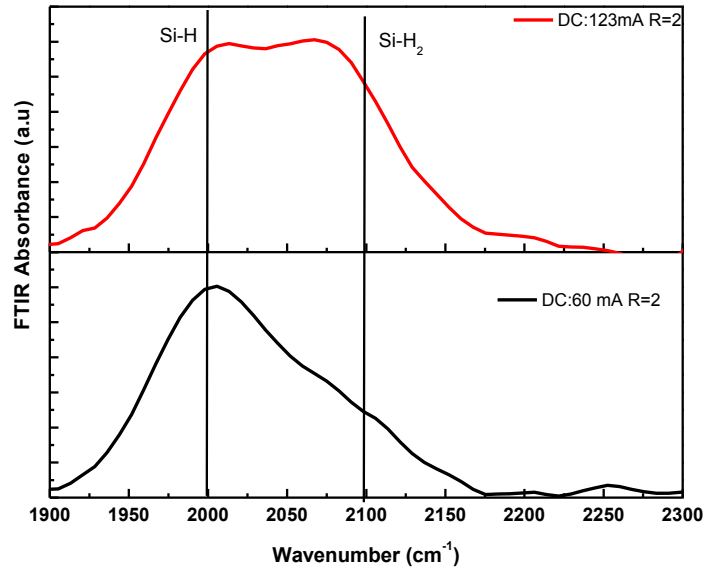


Figure 6.2-3: Comparison of FTIR spectra of 10 nm thick a-Si:H (i) layers grown by two different DC plasma process with R=2

On the contrast, in Figure 6.2-3 the di-hydride peak is higher at higher plasma DC for R = 2. However, there is a substantial difference in  $\tau_{\text{eff}}$  values of DC's. In this case, Si-H bonding configuration in bulk is not necessarily deterministic with respect to as-deposited quality. In this case  $\tau_{\text{eff}}$  can be limited by a more dominant recombination pathway through interface defects in the interface layer and not in bulk defects.

From life time measurements and FTIR absorption spectra one can conclude that within this R range low plasma DC leads lower lifetime and for high quality passivation plasma DC should be chosen as 123 mA.

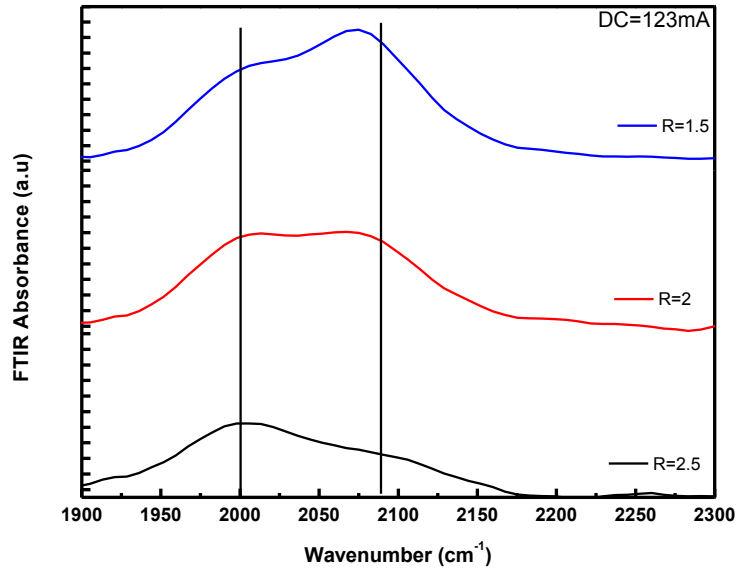


Figure 6.2-4: FTIR spectra of 10 nm thick a-Si:H (i) layers grown by three different R at a constant DC plasma (123mA)

In Figure 6.2-4 a remarkable shift of Si-H<sub>2</sub> bonding in the film deposited by higher DC plasma with different R can be seen. However, variation of  $\tau_{\text{eff}}$  values for each R is not significant. This suggests that the  $\tau_{\text{eff}}$  hence passivation quality of a-Si:H(i) layers are slightly dependent on the amount of SiH<sub>2</sub> and defects in the i-layer in this range of H<sub>2</sub> dilution. While plasma DC is decreasing the growth rate is decreasing as well. Lower growth rate can cause epi-Si growth on wafer surface [25].

In general it is argued that annealing has deleterious effects on epitaxial growth on the wafer surface and that annealed epi-Si causes more reduction in passivation quality. The life times were measured for as-deposited samples and after annealing at 300 °C under vacuum. It was seen that  $\tau_{\text{eff}}$  after annealing the samples deposited at higher DC is almost unchanged while the ones deposited at lower DC is reduced (for R=2 from ~420  $\mu\text{sec}$  to 320  $\mu\text{sec}$  and for R=2.5 from ~900  $\mu\text{sec}$  to 405  $\mu\text{sec}$ ). This confirms an epi-Si growth at the c-Si/a-Si:H interface during DC PECVD deposition.

In conclusion, micro structural bulk defects related with Si-H<sub>2</sub> bonding have a weak impact on  $\tau_{\text{eff}}$ . The higher plasma DC, hence more energetic ions, during a-Si:H

growth does not have deteriorate effect on c-Si surface passivation quality. However, the epitaxial-Si growth between the c-Si/a-Si:H(i) layer severely degrades passivation properties.

### 6.3 Effect of a-Si:H (i) Layer Thicknesses on the SHJ Cells

In the previous section we studied the effect of plasma DC and R on the a-Si:H film properties in terms of passivation. It is concluded that films deposited at higher plasma DC and R=2.5 showed better passivation quality. We fabricated SHJ solar cells with inserting a-Si:H(i) buffer layer at R=2.5 to correlate surface passivation quality with the SHJ cell performances.

In this section, we fabricated a-Si:H/c-Si hetero-junction solar cells with varying buffer layer thicknesses on p-type c-Si substrates, in an attempt to determine the influence of the buffer layer thicknesses on the solar cell performance. The solar cell structure is Ni-Al grids / 70 (nm) ITO / 10 nm a-Si:H (n) / 10 nm a-Si:H (i) / c-Si (p) / 10 nm a-Si:H (i) / 10 nm a-Si:H (p) / Al with varying a-Si:H (i) thickness. Before processing, the wafers were cleaned by the method summarized in Chapter 3. First 10 nm a-Si:H(i) buffer layers were deposited on both sides of c-Si(p) wafer at  $T_s=250$  °C and R =2.5 conditions. Then, a 10 nm a-Si:H(n) layer was deposited on the front side by using the gas flow ratios of  $[\text{SiH}_4]:[\text{H}_2]:[\text{PH}_3]$  20:120:10 sccm. Also, a 10 nm a-Si:H(p) layer is deposited on the rear side with the gas flow ratio of  $[\text{SiH}_4]:[\text{H}_2]:[\text{B}_2\text{H}_6]=20:120:15$  sccm. 70 nm Indium Tin Oxide (ITO) with metal grids on the front and evaporated Al contact on the rear were deposited to fabricate SHJ cells. The SHJ cells with the area of  $0.56 \text{ cm}^2$  were characterized by J-V measurement with AM1.5 illumination after a post annealing of 15 min at the temperature of  $150$  °C.

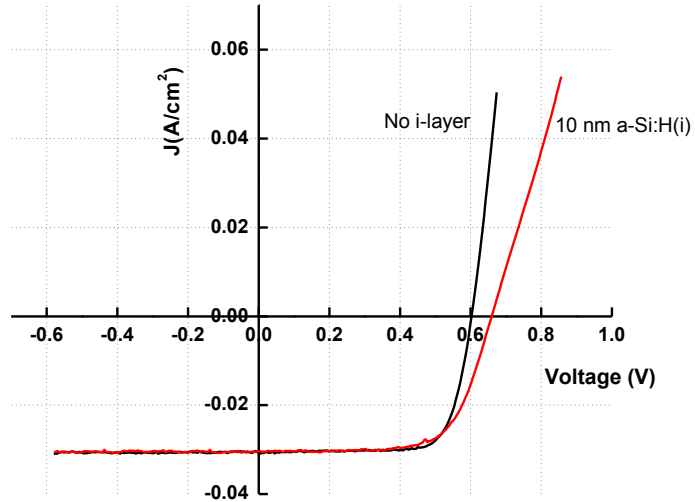


Figure 6.3-1: J-V curves of Ni-Al grids / 70 (nm) ITO / a-Si:H (n) / c-Si (p) / Al hetero-junction solar with and without a-Si:H (i) buffer layers.

Figure 6.3-1 shows the J-V curve of SHJ cells with and without a-Si:H(i) buffer layers. As it can be seen, the incorporation of buffer layer leads to increment of  $V_{oc}$  ~50 mV due to suppressing the interface recombination. The advantageous role of intrinsic layer can be seen evidently since  $V_{oc}$  improved from ~ 600 mV for SHJ to 650 mV for both side a-Si:H(i) layers.

As a-Si:H(i) layer has an influence on the carrier transport and recombination mechanism, in particular i layer thickness is one of the critical parameters for SHJ parameters. A set of SHJ were prepared by varying i-layer thickness while emitter a-Si:H(n) and back a-Si:H(p) layers thicknesses are fixed at 10 nm.

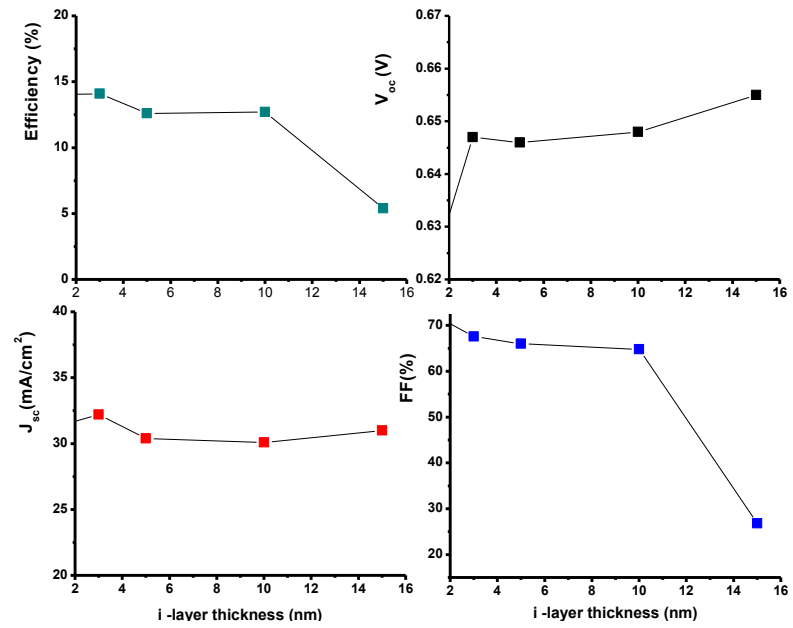


Figure 6.3-2: Solar cell parameters of the SHJ plotted as a function of a-Si:H (i) layer thickness.

With increasing i-layer thickness  $V_{oc}$  and  $J_{sc}$  slightly changes. However, efficiency and FF shows a sharp decrease at the thickness of 15 nm.

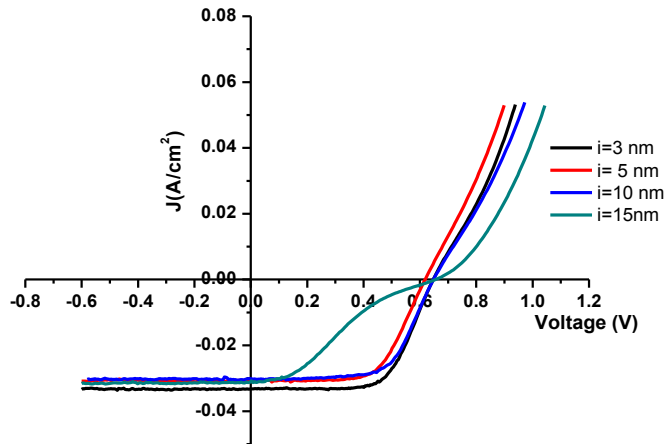


Figure 6.3-3: J-V curves of Ni-Al grids / 70 (nm) ITO / a-Si:H (n) / c-Si (p) / Al hetero-junction solar with different thickness of a-Si:H(i) buffer layers.

From Figure 6.3-3 it is obviously seen that the “S” shape of JV curve by high a-Si:H(i) thickness. The a-Si:H(i) layer affects the carrier transport across the heterojunction and leads to a low FF due to an increase in  $R_s$ .

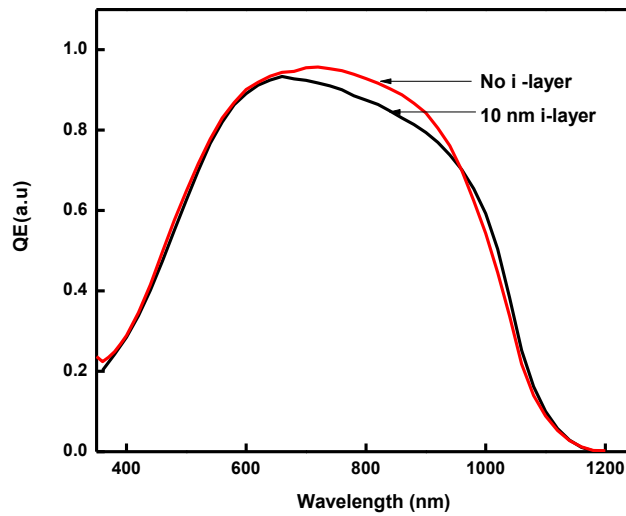


Figure 6.3-4: The QE spectra of SHJ cells with and without i-layer.

Figure 6.3-4 shows the external QE spectra of the solar cells shown in Figure 6.3-1 (SHJ cells with and without i-layer). It can be seen that including i-layer does not lead any significant reduction in the short wavelength region (<600 nm). However, the longer wavelength (>600 nm) response reduces. This implies that electric field within i-layer increases which leads to a reduction in the depletion layer thickness in c-Si (p) and hampers the diffusive carrier collection from the deeper part of the c-Si [82].

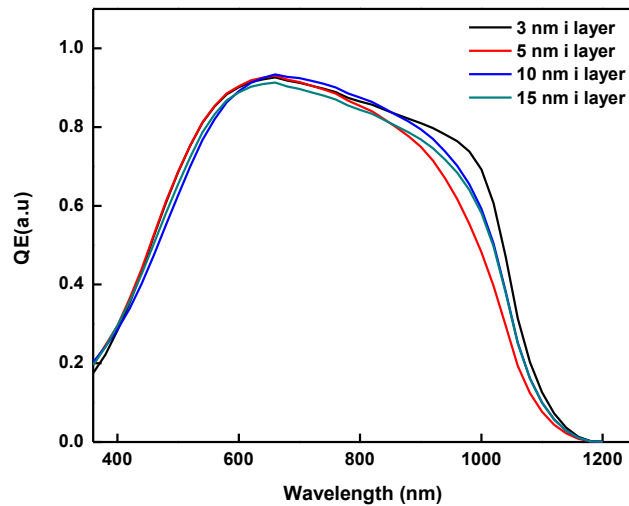


Figure 6.3-5: The QE spectra of SHJ cells with varying i-layer thicknesses.

In Figure 6.3-5, the QE spectra with varying i-layer thickness is displayed. As it is shown the short wavelength response decreases slightly by increasing i-layer thickness. Thus, the reduction in  $J_{sc}$  shown in Figure 6.3-2 arises from this small degradation of the short wavelength response. This is mainly due to absorption loss by increasing thickness. The same trend is observed at the long wavelength region. By increasing i-layer thickness the electric field increases at the high-resistive a-Si:H(i) layer side while electric field within the c-Si substrate decreases [82]. This leads to a reduction in

depletion layer thickness in the c-Si and hampers the diffusive carrier collection from the deeper part of the c-Si.

## 6.4 Temperature Dependence of J-V Analysis

In this section the transport mechanism in the SHJ solar cells 3nm i-layer were evaluated from the temperature dependence of dark current density-voltage characteristics. The dark J–V curves of SHJ cells were obtained at the temperatures between 0 and 100 °C. The results acquired from the analytical model are analyzed in terms of activation energies, saturation current densities and diode ideality factors, discussed by prevalent transport mechanism, and connected to device parameters.

Figure 6.1-1 shows the forward dark Ln(J)-V curve of SHJ solar cell with 3 nm i- layers as a function of temperature. As it is seen from the figure, in the region of  $0.3 < V < 0.5$  dark current density increases linearly.

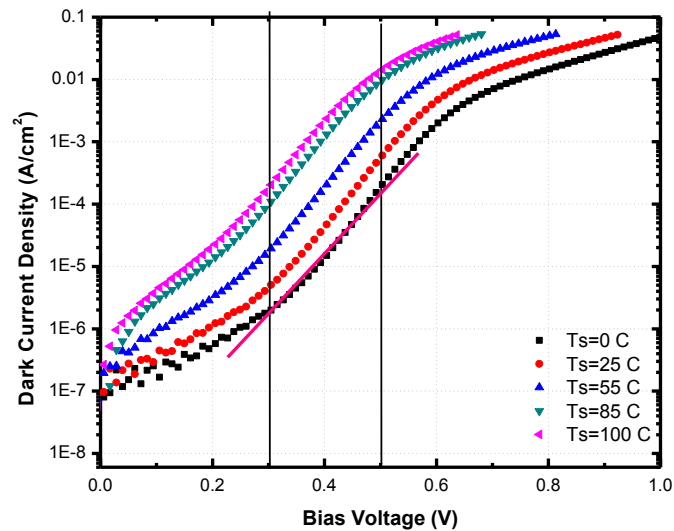


Figure 6.4-1: Semi-logarithmic graph of forward dark current density at different temperatures.

In this region the dark J-V characteristic is expressed by the familiar form as in Eq. (6.1)  $J_0$  and  $n$  are evaluated from the intercept at  $V=0$  and the slope of  $\ln(J) - V$  in the linear region ( $0.3 < V < 0.5$ ). This procedure was applied for J-V curves of each temperature. The  $J_0$ ,  $n$  values obtained from dark J-V analysis are listed in Table 12.

$$J = J_0 \left[ \exp\left(\frac{qV}{nkT}\right) - 1 \right] \quad (6.1)$$

Where  $J_0$  is expressed as;

$$J_0 = J_{00} \exp\left(\frac{-E_a}{kT}\right) \quad (6.2)$$

Table 12: The  $J_0$ ,  $n$  values evaluated from the temperature dependent J-V curves of SHJ solar cell with 3nm i buffer layer.

| <b>T (°C)</b> | <b><math>J_0(\text{mA/cm}^2)</math></b> | <b>n</b> |
|---------------|---|----------|
| <b>0</b>      | $7.0 \times 10^{-10}$                   | 1.0      |
| <b>25</b>     | $9.0 \times 10^{-10}$                   | 1.0      |
| <b>40</b>     | $2.0 \times 10^{-9}$                    | 1.0      |
| <b>55</b>     | $4.0 \times 10^{-9}$                    | 1.0      |
| <b>70</b>     | $9.0 \times 10^{-9}$                    | 1.1      |
| <b>85</b>     | $2.0 \times 10^{-8}$                    | 1.2      |
| <b>100</b>    | $7.0 \times 10^{-8}$                    | 1.2      |

As it can be seen from Table 12 ideality diode factor is temperature dependent and saturate around 1-1.2. As a general rule,  $n=1$  refers to diffusion or thermionic emission mechanism [87].  $n>1$  suggests that there is additional transport mechanisms such as recombination in the structure. The recombination mechanism is believed to be SRH recombination via defect states in the band gap enhanced by trap-assisted tunneling. In SHJ solar cells three recombination paths are dominant which are: recombination in the quasi-neutral bulk of the absorber, recombination in the space

charge region, and recombination at the interface. To decide whether recombination in the bulk or interface is dominant the activation energy  $E_a$  should be found. The activation energy was calculated by using Eq. (6.2) from the slope of  $\ln(J_0)$  versus  $1/T$  plot (see Figure 6.4-2).

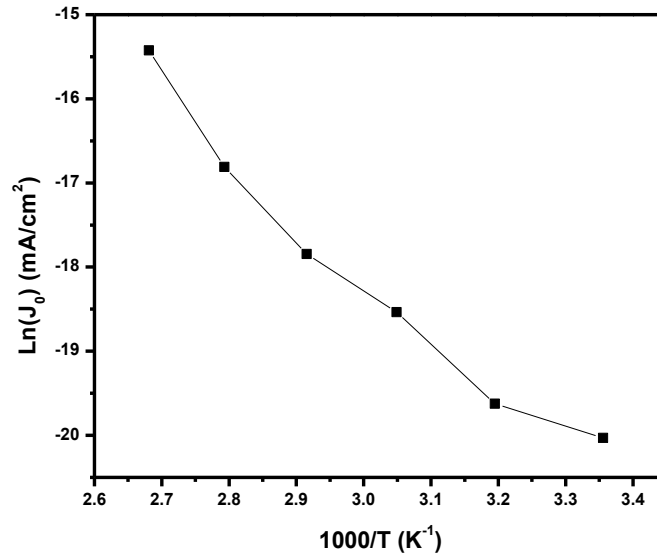


Figure 6.4-2: The plot of  $\ln(J_0)$  vs.  $1000/T$  for the SHJ cell with 3 nm i layer.

$\ln(J_0)$  versus  $1000/T$  shows a linear behavior and the activation energy value was estimated at around 0.57 eV which is close to  $E_g/2$ , where  $E_g$  is the band gap of c-Si, which claims that the dominant recombination mechanism is interface recombination [87].

The temperature dependent J-V analysis, as explained in this section, will be applied for the samples with varying i-layer thickness for future studies. This can lead us to obtain information and a correlation between the transport mechanism and solar cells parameters.

## 6.5 Conclusion

In the first part of this chapter plasma DC and H<sub>2</sub>-dilution effect on the a-Si:H(i) layer passivation quality were presented. It is shown that at higher plasma DC leads to better passivation quality and consequently higher effective lifetime of the Si wafer.

In the second part we fabricated a-Si:H/c-Si heterojunction solar cells including optimum a-Si:H(i) layer on both sides of c-Si(p). We analyzed different a-Si:H(i) layer thicknesses and evaluated the fundamental parameters of a-Si:H/c-Si solar cells. The optimum i-layer thickness was determined as 3-10 nm based on the reduction in FF increasing series resistance with thickness and decreasing J<sub>sc</sub> due to QE reduction in the long wavelength region. Conversely, while the n-layer thickness increases QE decreases only in the short wavelength region.

By using the optimum thicknesses of i and doped layers, we obtained a conversion efficiency of 14.1% with the V<sub>oc</sub> of 650 mV in a single heterojunction solar cell.

## CHAPTER 7

### CONCLUSION

In this thesis a-Si:H(n)/c-Si(p) heterojunction solar cells fabricated via magnetron sputtering and PECVD were investigated. Both techniques are widely used for thin film fabrication due to their superior features.

In the first part of the experimental study a-Si:H(n)/c-Si(p) solar cells were fabricated by magnetron sputtering technique. The low processing temperature, non-toxic gas media, easy thickness controlling, simple parameter adjustment are the main advantages of the sputtering technique. Furthermore non-toxic highly doped sputtering targets can last for many years, which is economically beneficial both for laboratory researches and large scale manufacturing.

Prior to fabrication of solar cells Si thin films were deposited and their optical, electrical and structural properties were analyzed in order to find optimum conditions for solar cell application. It was found that the deposition temperature has a great influence on film properties. It is observed that increasing substrate temperature yields higher optical band gap which is desirable for an emitter layer. On the other hand it was found via Raman spectroscopy that the samples deposited at high temperatures showed simultaneous presence of microstructure and amorphous phase. In order to achieve high band gap a-Si films, hydrogen was successfully introduced in to the deposition chamber at low deposition temperatures ( $\leq 200$  °C). The band gap increased from 1.4 eV to about 1.9 eV due to the saturation of tail states in the band gap of a-Si with the addition of hydrogen during the deposition. Although high band gap amorphous thin films were obtained at low temperatures, a-Si:H(n)/c-Si(p) solar cells exhibited very low rectification properties and poor solar cell performance. We found that this is mainly

due to high resistivity of the a-Si:H film which suggest that deposited films are not sufficiently doped. The insufficient doping in a-Si:H causes a poor p-n junction with low rectification and hence low  $V_{oc}$ . We conclude that the use of highly doped Si targets do not ensure enough doping concentrations in thin a-Si:H films. It should be also noted that high energetic ion bombardment in sputtering process causes damage on the c-Si surface which increases interface defects and hence causes low  $V_{oc}$ . Even though sputtering has advantages, proper doping techniques should be developed before it can applied to a solar cell. For this reason, PECVD is a better fabrication method for silicon heterojunction solar cells.

In addition to sputtering, a-Si:H(n)/c-Si(p) solar cells were fabricated by PECVD technique. Firstly, heterojunction cells were fabricated without any buffer layer and then a-Si:H(i) layer was included.

a-Si:H(n)/c-Si(p) solar cell performance was investigated with special emphasis on the effect of plasma process parameters of emitter a-Si:H(n) layer. The optimization of a-Si:H(n) as an emitter on p-type SHJ thin films was investigated by analyzing conductivity, band gap, and hydrogen bonding profile. It is shown that the choice of deposition parameters effects to the film properties. Among deposition parameters, doping gas flow rate and deposition temperature have considerable effect than the others. Higher FF and  $V_{oc}$  were achieved by increasing  $PH_3$  flow rate which implies that the improvement in the band offset between a-Si:H and c-Si. The FF increased from 53% to 64 % and  $V_{oc}$  improved from 0.552 to 0.600 V by increasing the doping gas flow. Deposition temperature on the other hand showed significant variation in FF. The FF was 67% for 200  $^{\circ}C$  and 76% for 250  $^{\circ}C$  while gaining almost the same  $V_{oc} \sim 0.600$  V. We found that this improvement is mainly the reason of decreasing series resistance of the device caused by improved ITO and emitter layer contact. After optimizing the emitter layer parameters we achieved  $J_{sc}=30.7$  mA / cm<sup>2</sup>  $V_{oc}=0.600$  V and FF=76% with the efficiency of 14.1%.

After obtaining optimum conditions for the heterojunction solar cells, a thin buffer layer was included on the front and on the rear side of the heterostructure to improve the c-Si surface passivation. a-Si:H(i) layer passivation quality was

investigated under the influence of plasma DC and H<sub>2</sub> dilution. It was shown that lower plasma DC causes poor passivation quality resulting low effective lifetime of the Si wafer. The optimum H<sub>2</sub> dilution was found to be 2.5 during the deposition of the intrinsic a-Si:H layer. The surface passivation quality was evaluated by measuring  $\tau_{\text{eff}}$  using QSSPC. In optimum deposition condition for a-Si:H(i),  $\tau_{\text{eff}}$  was obtained as ~1 ms by inserting a-Si:H(i) on both side of c-Si(p) wafer. Inserting a-Si:H(i) layers improve the passivation quality and enables high  $V_{\text{oc}}$ . The  $V_{\text{oc}}$  of the solar cells increases from 0.600 to 0.650 V while decreasing in FF to 65%. With increasing a-Si:H(i) layer thicknesses,  $V_{\text{oc}}$  increases slightly however  $J_{\text{sc}}$  reduces gradually. When i-layer thickness is greater than 10 nm FF reduces sharply due to increasing  $R_{\text{s}}$ . By using optimum a-Si:H(i) and emitter layer we achieved a solar cell efficiency of 14.1% with the FF of 65% and  $V_{\text{oc}}$  of 0.600 V.

## REFERENCES

- [1] "World Energy Outlook-2004" Online,  
www.iea.org/weo/docs/weo2004/WEO2004.pdf, Last access on (10/06/2011).
- [2] D. M. Chapin, C. S. Fuller, and G. L. Pearson, "A New Silicon p-n Junction Photocell for Converting Solar Radiation into Electrical Power," *J. Appl. Phys.*, vol. 25, 1954.
- [3] J. Nelson, *The Physics of Solar Cells.*, Imperial College Press, 2003.
- [4] S. Hegedus and A. Luque, *Handbook of Photovoltaic Science and Engineering.*  
John Wiley&Sons Ltd., 2003.
- [5] A. Goetzberger, J. Luther, and G. Willeke, "Solar Cells: Past, Present, Future," *Sol.Energy. Mat. and Sol.Cells.*, vol. 74, pp. 1-11, 2002.
- [6] M.A. Green, "Recent Developments in Photovoltaics," *Solar Energy*, vol. 76, pp. 3-8, 2004.
- [7] M.A Green, K. Emery, Y. Hishikawa and W. Warta, "Solar Cell Efficiency Tables (Version 37)," *Prog. Photovolt: Res. Appl*, vol. 19, pp. 84-92, 2011.
- [8] M.A Green, "Third Generation Photovoltaics: Ultra-high Conversion Efficiency at Low Cost," *Prog. Photovolt: Res. Appl*, vol. 9, pp. 123-135, 2001.
- [9] D.E. Carlson and C.R. Wronski, "Amorphous Silicon Solar Cells," *Appl. Phys. Lett.*, vol. 28, p. 671, 1976.
- [10] M. H. Brodsky, M. A. Frisch, J. F. Ziegler, and , W. A. Lanford, "Quantitative Analysis of Hydrogen in Glow Discharge Amorphous Silicon," *Appl. Phys. Lett.*, vol. 30, p. 561, 1977.

- [11] D. L. Staebler and C. R. Wronski, "Reversible Conductivity Changes in Discharge-Produced Amorphous Si," *Appl. Phys. Lett.*, vol. 31, p. 292, 1977.
- [12] M.A Green, "Thin-film Solar Cells: Review of Materials, Technologies and Commercial Status," *J Mater Sci: Mater Electron*, vol. 18, pp. S15–S19, 2007.
- [13] "New World Record With Efficient CIGS Solar Cell- Press release 11/2010" Online,  
[http://www.zswbw.de/fileadmin/ZSW\\_files/Infoportal/%20Presseinformationen/docs/pi11-2010-e\\_ZSW-Weltrekord-DS-CIGS.](http://www.zswbw.de/fileadmin/ZSW_files/Infoportal/%20Presseinformationen/docs/pi11-2010-e_ZSW-Weltrekord-DS-CIGS.), Last access on (19/01/2012).
- [14] RR King et al., "Band-Gap-Engineered Architectures For High-Efficiency Multijunction Concentrator Solar Cells," in *24th European Photovoltaics Solar Energy Conference and Exhibition*, Hamburg, 2009.
- [15] S. Wojtczuk et al., "InGaP/GaAs/InGaAs Concentrators Using Bi-Facial Epigrowth," in *35th IEEE PVSC*, Honolulu, 2010.
- [16] "NREL Compilation of Best Research Solar Cell Efficiencies." Online,  
<http://www.nrel.gov>, Last access on,12/10/2011.
- [17] F. Roca, J. Carabe, and A. Jäger-Waldau, "Silicon Heterojunction Cells R&D in Europe," in *31th IEEE Photovoltaics Specialists Conference*, Orlando, USA, 2005.
- [18] W. Fuhs, K. Niemann, and J. Stuk, "Heterojunctions of Amorphous Silicon & Silicon Single Crystals," *Int. Conf. Tetrahedrally Bonded Semiconductors, Yorktown Heights, N.Y.*, pp. 345-350, 1974.
- [19] W. E. Comber, "Substitutional Doping of Amorphous Silicon," *Solid State Communications*, vol. 17, pp. 1193-1196, 1975.

- [20] M Tanaka, M Taguchi, T. Matsuyama, T. Sawada, and S. Tsuda, "Development of New a-Si/c-Si Heterojunction Solar Cells: ACJ-HIT (Artificially Constructed Heterojunction With Intrinsic Thin-Layer).," *Jpn.J. Appl. Phys.*, vol. 31, pp. 3518–3522, 1992.
- [21] "SANYO Develops HIT Solar Cells with World's Highest Energy Conversion Efficiency of 23.0 %" , Online, <http://sanyo.com/solar/News>, Last access on (11/11/2011)
- [22] Q.Wang, "High-Efficiency Hydrogenated Amorphous/Crystalline Si Heterojunction Solar Cells", vol. 89, pp. 2587–2598, 2009.
- [23] L. Korte, A. Laades, and , M. Schmidt, "Electronic States in a-Si:H/c-Si Heterostructures," *J. of Non-Crystalline Solid*, vol. s 352 , pp. 1217-1220, 2006.
- [24] M. Schmidt et al., "Physical and Technological Aspects of a-Si:H/c-Si Heterojunction Solar Cells," in *2006 IEEE 4th World Conference on Photovoltaic Energy Conversion*, Hawaii, 2006.
- [25] Hiroyuki Fujiwara and Michio Kondo, "Impact of Epitaxial Growth at the Heterointerface of a -Si:H/ c - Si Solar Cells," *Appl. Phys.Lett.*, vol. 90, p. 013503, 2007.
- [26] E. Conrad, K. V. Maydell, H. Angermann, C. Schubert, and , M. Schmidt, "Optimization of Interface Properties in a-Si:H/c-Si Heterojunction Solar Cells.," in *IEEE 4th World Conference on Photovoltaic Energy Conversion, IEEE.*, Hawaii, 2006, pp. 1263-1266.
- [27] Q. Wang, M.R. Page, E. Iwaniczko, Y.Q. Xu, and L. Roybal, "Crystal Silicon Heterojunction Solar Cells by Hot-Wire CVD," in *33rd IEEE Photovoltaic Specialists Conference* , 2008.
- [28] B. Jagannathan, W.A Anderson, and J. Coleman, "Amorphous Silicon/p-type Crystalline Silicon Heterojunction Solar Cells," *Sol.Energy Mat. and Sol. Cells*,

vol. 46, pp. 289-310, 1997.

- [29] J.E Cotter, J. H. Guo, P. J. Cousins, M. D. Abbott, and F. W. Che, "P-Type Versus n-Type Silicon Wafers: Prospects for High-Efficiency Commercial Silicon Solar Cells," *IEEE Transactions On Electron Devices*, vol. 53, no. 8, 2006.
- [30] J. Schmidt, K. Bothe, R. Bock, and C. Schmiga, "N-Type Silicon – The Better Material Choice for Industrial High-Efficiency Solar Cells ?," in *22nd European Photovoltaic Solar Energy Conference* , Milan, Italy, 2007.
- [31] W. Shockley, "The Theory of pn Junctions in Semiconductors and pn Junction Transistors," *Bell Syst. Tech.*, vol. J.28, pp. 435-489, 1949.
- [32] C. T. Sah, R. N. Noyce, and W. Shockley, "Carrier Generation and Recombination in p-n Junctions and p-n Junction Characteristics.," in *Proceedings of the IRE*, vol. 45, 1957, pp. 1228-1243.
- [33] R. L. Anderson, "Experiments on Ge-GaAs Heterojunctions," *Solid-State Electron*, vol. 5, p. 341, 1962 1962.
- [34] A.G Milnes and D. Feucht, *Heterojunctions and Metal-Semiconductor Junctions.:* London Acedemic Press, 1972.
- [35] T. F. Schulze, L. Korte, E. Conrad, M. Schmidt, and B. Rech, "Electrical Transport Mechanisms in a -Si: H/c -Si Heterojunction Solar Cells," vol. 107, p. 023711, 2010.
- [36] D.Schroeder., *Semiconductor Material and Device Characterization.:* John Wiley&Sons, Inc., 1998.
- [37] E. Yablonovitch, T. Gmitter, RM. Swanson, and YH. Kwark, "A 720mV Open Circuit Voltage SiO<sub>x</sub>:c-Si:SiO<sub>x</sub> Double Heterostructure Solar Cell", *Applied Physics Letters*, vol. 47, no. 11, pp. 1211-1213, 1985.

- [38] M. R. Page et al., "Passivated a-Si:H Back Contacts for Double-Heterojunction Silicon Solar Cells.," in *IEEE 4th World Conference on Photovoltaic Energy Conversion (WCPEC-4)*, vol. 3, Waikoloa, Hawaii, 2006, pp. 1485-1488.
- [39] Vi. A Dao et al., "Simulation and Study of the Influence of the Buffer Intrinsic Layer, Back-Surface Field, Densities of Interface Defects, Resistivity of p-type Silicon Substrate and Transparent Conductive Oxide on Heterojunction With Intrinsic Thin Layer (HIT) Solar Cell," *Solar Energy*, vol. 84, pp. 777–783, 2010.
- [40] M. Taguchi, A. Terakawa, E. Maruyama, and M. Tanaka, "Obtaining a Higher Voc in HIT Cells," *Prog. Photovolt: Res. Appl.*, vol. 13, pp. 481–488, 2005.
- [41] T.H. Wang et al., "Toward Better Understanding and Improved Performance of Silicon Heterojunction Solar Cells."
- Online, <http://www.nrel.gov/docs/fy04osti/36669.pdf>, Last access on (4/1/2011)
- [42] W. Shockley and W. Read, "Statistics of Recombination of Holes and Electrons.," *Phys Rev*, vol. 87, pp. 835-842, 1952.
- [43] R.N Hall, "Electron-Hole Recombination in Germanium," *Phys. Rev.*, vol. 87, p. 387, 1952.
- [44] Thomas Mueller, *Heterojunctions Solar Cells (a-Si:H / c-Si) Investigations on PECV Deposited Hydrogenated Silicon Alloys for use as High-Quality Surface Passivation and Emitter/BSF.*: Logos , 2009.
- [45] M.J. Kerr and A. Cuevas, "Very Low Bulk and Surface Recombination in Oxidized Silicon Wafers," *Semicond. Sci. Technol.*, vol. 17, pp. 35-38, 2002.
- [46] J. Schmidt and , A.G. Aberle, "Carrier Recombination at Silicon-Silicon Nitride Interfaces Fabricated by Plasma-Enhanced Chemical Vapor Deposition," *J. Appl.Phys.*, vol. 85, pp. 3626-3633, 1999.

- [47] T. Sawada, T. Norihiro, S. Tsuge, and B. Toshiaki, "High-Efficiency a-Si/c-Si Heterojunction Solar Cell," *IEEE Photovoltaic Specialists Conference*, vol. 2, pp. 1219 - 1226, 1994.
- [48] T. Mueller, S. Schwertheim, M. Scherff, and R.F Wolfgang, "High Quality Passivation For Heterojunction Solar Cells By Hydrogenated Amorphous Silicon Suboxide Films," *Appl. Phys. Lett.*, vol. 92, p. 033504, 2008.
- [49] S. Olibet, E. Vallat-Sauvain, C Ballif, and L. Fesquet, "Recombination Through Amphoteric States at the Amorphous/Crystalline Silicon Interface: Modelling and Experiment," EPFL-Infoscience, 2007.
- [50] W. Schmidt, K. D. Rasch, and K. Roy, in *16 IEEE Photovoltaic Specialist Conference*, San Diego, 1982, pp. 537-542.
- [51] Mitsuharu Konuma, *Plasma Techniques for Film Deposition.*: Alpha Science, 2005.
- [52] R.C. Chittick and J.H. Alexander, "The Preparation and Properties of Amorphous Silicon," *J. Electrochem. Soc.*, vol. 116, no. 1, pp. 77-81, 1969.
- [53] A. Matsuda, M. Takai, T. Nishimoto, and M. KondoKerr, "Control of Plasma Chemistry for Preparing Highly Stabilized Amorphous Silicon at High Growth Rate.," *J. Appl. Phys.*, 2003.
- [54] S. Bowden, U. Das, S. S. Hegedus, and R. W. Birkmire, "Carrier Lifetime as A Developmental and Diagnostic Tool in Silicon Heterojunction Solar Cells," in *IEEE 4th World Conference on Photovoltaic Energy Conversion*, 2006, pp. 1295 – 1298.
- [55] J. Appel et al., "Effect of Junction Interface Modification of Silicon Heterojunction Solar Cells," in *35th IEEE Photovoltaic Specialists Conference*, 2010, pp. 001295 –001298.

- [56] E. Matthew, S. Bowden, U. Das, and M. Burrows, "Effect of Texturing And Surface Preparation On Lifetime And Cell Performance In Heterojunction Silicon Solar Cells.," *Sol. Energ. Mater.*, vol. 92, pp. 1373-1377, 2008.
- [57] *Photovoltaics CDROM*” Online, <http://pvcdrrom.pveducation.org/>, Last access on (24/02/2010).
- [58] Christopher P. Thompson, “Characterization of Photocurrent and Voltage Limitations of Cu(In-Ga)Se<sub>2</sub> Thin-Film Polycrystalline Solar Cells.”, M.S. Thesis, Dept. Electrical & Computer Eng., University of Delaware, 2008.
- [59] S. S. Hegedus and W. N. Shafarman, "Thin-Film Solar Cells: Device Measurements and Analysis. ," *Prog. Photovolt: Res. Appl.*, vol. 12, pp. 155-176, 2004.
- [60] R. A. Sinton and A. Cuevas, "Contactless Determination of Current-Voltage Characteristics and Minority-Carrier Lifetimes in Semiconductors From Quasi-Steady-State," *Appl. Phys. Lett*, vol. 37, pp. 515–533, 1980.
- [61] M. J. Kerr, A. Cuevas, and R. A. Sinton, "Generalized Analysis of Quasi-Steady-State and Transient Decay Open Circuit Voltage Measurements," vol. 91, pp. 399–404, 2002.
- [62] S. Perkowitz, *Optical Characterization of Semiconductors*:: Academic Press., 1993.
- [63] T. Lohner et al., "Composition and Thickness of RF Sputtered Amorphous Silicon Alloy Films ," *Acta Polytechnica Hungarica*, vol. 5, no. 2, pp. 23-30, 2008.
- [64] M.J. Thompson, J. Allison, and M. Alkaisi, "Doping of Sputtered Amorphous-Silicon Solar Cells," *Solid-State and Electron Devices*, vol. 2 , no. Special Issue , 1978.
- [65] A. J. Lewis, G. Connell, W. Paul, J. R. Pawlik, and R. J. Temkin, *The tetrahedrally*

*Bonded Amorphous Semiconductors*, M.H. Brodsky and S. Kirkpatrick, Eds. New York: Am. Inst. Phys, 1974.

- [66] J. I. Pankove, M. A. Lampert, and M. L. Tarnag, "Hydrogenation and Dehydrogenation of Amorphous and Crystalline Silicon," *Appl. Phys. Lett.*, vol. 32, p. 439, 1978.
- [67] D. Han, J.D. Lorentzen, J. Weinberf-Wolf, and L.E. McNeil, "Raman Study of Thin Films of Amorphous-to-Microcrystalline Silicon Prepared by Hot-Wire Chemical Vapor Deposition," *J. Appl. Phys.*, vol. 94, p. 2930, 2003.
- [68] A. Froitzheim, M. Schmidt, W. Fuhs R. Stangl, "Design Criteria for Amorphous/Crystalline Silicon Heterojunction," *Proceedings of 3rd World Conference on Photovoltaic Energy Conversion*, vol. 2, pp. 1005-1008, 2003.
- [69] W Fuhs, L. Korte, and M. Schmidt, "Heterojunctions of Hydrogenated Amorphous Silicon and Monocrystalline Silicon," *J.Optoelectron Adv. M.*, vol. 8, pp. 1989-1995, 2006.
- [70] E. Conrad, H. Angermann, R. Stangl, M. Schmidt L. Korte, "Advances in a-Si:H/c-Si Heterojunction Solar Cell Fabrication and Characterization," *Solar Energy Materials & Solar Cells*, vol. 93, pp. 905-910, 2009.
- [71] R.A. Sinton and A. Cuevas, "Contactless Determination of Current-Voltage Characteristics and Minority-Carrier Lifetimes in Semiconductors From Quasi-Steady-State Photoconductance Data," *Appl. Phys. Lett.*, vol. 69, p. 2510, 1996.
- [72] H. Fujiwara, M. Kondo, and A Matsuda, "Depth Profiling of Silicon-Hydrogen Bonding Modes in Amorphous And Microcrystalline Si:H Thin Films by Real-Time Infrared Spectroscopy And Spectroscopic Ellipsometry," *Journal of Applied Physics*, vol. 91, pp. 4181-4190, 2002.
- [73] W Fuhs, L. Korte, and Schmidt Schmidt, "Heterojunctions of Hydrogenated Amorphous Silicon and Monocrystalline Silicon," *Journal of Optoelectronics and*

*Advanced Materials*, vol. 8, pp. 1989 - 1995, 2006.

- [74] Kwang-sun Ji, Junghoon Choi, Won-seok Choi, Heon-Min Lee, and Donghwan Kim, "Surface Passivation Properties of Boron And Phosphor-Doped a-Si:H Films With Multi-Step Deposition For Si Heterojunction Solar Cells," in *35th IEEE Photovoltaic Specialists Conference (PVSC)* , Honolulu, 2010, pp. 003190 - 003192.
- [75] W. N. Shafarman and S. S. Hegedus, "Thin-Film Solar Cells: Device Measurements and Analysis," *Prog. Photovolt: Res. Appl.*, vol. 12, pp. 155-176, 2004.
- [76] Jui-Chung Hsiao, "Effect of Hydrogen Dilution on the Intrinsic a-Si:H Film of the Heterojunction Silicon-Based Solar Cell," *J. Electrochem. Soc.*, vol. 158, no. 9, pp. H876-H878, 2011.
- [77] Ujjwal Das, Stuart Bowden, Michael Burrows, Steven Hegedus, and Robert Birkmire, "Effect of Process Parameter Variation in Deposited Emitter And Buffer Layers on the Performance of Silicon Heterojunction Solar Cells," in *Conference Record of the 2006 IEEE 4th World Conference on Photovoltaic Energy Conversion*, vol. 2, Waikoloa, 2006, pp. 1283 - 1286.
- [78] Chen Fengxiang and Ai Yu Wang Lisheng, "Simulation of High Efficiency Heterojunction Solar Cells with AFORS-HET," *Journal of Physics: Conference Series* , vol. 012177, p. 012177, 2011.
- [79] Hiroyuki Fujiwara, Tetsuya Kaneko, and Michio Kondo, "Optimization of Interface Structures in Crystalline Silicon Heterojunction Solar Cells," *Sol. Energ. Mat. Sol. Cells*, vol. 93, pp. 725-728, 2009.
- [80] S. De Wolf and M. Kondo, "Abruptness of a-Si:H/c-Si Interface Revealed by Carrier Lifetime Measurements," *App. Phys. Letters*, vol. 90, p. 042111, 2007.

- [81] M. Burrows, "Role Of Silicon Hydride Bonding Environment in a-Si:H Films for C-Si Surface Passivation," Materials Science and Engineering University of Delaware, PhD.Thesis 2008.
- [82] Hiroyuki Fujiwara and Michio Kondo, "Effects of a-Si:H Layer thicknesses on The Performance of a-Si:H/c-Si Heterojunction Solar Cells," *J. Appl. Phys.*, vol. 101, p. 054516, 2007.
- [83] S. Kim, J.C. Lee, S. Park, Y.J Kim, and K.H Yoon, "Effect of Hydrogen Dilution on Intrinsic a-Si:H Layer Between Emitter and Si Wafer in Silicon Heterojunction Solar Cell," *Sol. Energ.Mat.Sol. Cells*, vol. 92, pp. 298-301, 2008.
- [84] U. K. Das, M. Burrows, M. Lu, S. Bowden, and R. Birkmire, "Surface Passivation Quality and Structure of Thin a-Si:H Layers on n-Type Crystalline Si (100) And (111) Wafers," in *22. European Photovoltaic Solar Energy Conference and Exhibition*, Milan, 2007.
- [85] W.M.M. Kessels, A.H.M. Smets, J.P.M. Hoefnagels, and M.G.H. Boogaarts, "Relation Between Growth Precursors and Film Properties for Plasma Deposition of a-Si:H at Rates up to 100 Å/s," *Mat. Res. Soc. Symp. Proc.* , vol. 609, 2000.
- [86] W. M. M. Kessels, R.J. Severens, A.H.M Smets, and B.A. Korevaar, "Hydrogenated Amorphous Silicon Deposited at Very High Growth Rates by Expanding Ar-H<sub>2</sub>-SiH<sub>4</sub> Plasma," *J. Appl. Phys.*, vol. 89, no. 4, 2001.
- [87] T. F. Schulze, L. Korte, E. Conrad, M. Schmidt, and B. Rech, "Electrical Transport Mechanisms in a-Si:H / c -Si Heterojunction Solar Cells," *J. App.Phys.*, vol. 107, p. 023711, 2010.

## **CURRICULUM VITAE**

### **PERSONEL INFORMATION**

Surname, Name: Eygi, Zeynep Deniz

Nationality: Turkish (TC)

Date and Place of Birth: 25 September 1978, İstanbul

Email: zeynepdeniz@gmail.com

Phone: +90 312 210 43 24

### **EDUCATION**

PhD: Middle East Technical University (METU), Physics Department, Ankara  
December-2011.

M.Sc (With Thesis): Middle East Technical University (METU), Physics Department,  
Ankara, January-2004.

M.Sc (Without Thesis): Gazi University, Physics Education Department, Ankara,  
January-2004.

B.Sc.: Gazi University, Physics Department, June-2001.

High School: Fethiye Kemal Mumcu Anatolian High School, January-1996.

## PUBLICATIONS

1. Turan G., Eygi Z.D. “Standard Model CP Violation in  $B \rightarrow X_d l^+ l^-$  Decays.” Mod.Phys.Lett.A.18, No. 38, 2735–2747 (2003).
2. Eygi Z.D., Das U., Hegedus S. “Optimizing Emitter-Buffer Layer Stack Thickness For p-Type SHJ Solar Cells” will be submitted

## PROCEEDINGS

1. Z.D. Eygi, U. Das, S. Hegedus and R. Birkmire, “Improved FF in p-Si Heterojunction Solar Cells Due To Optimized ITO/Emitter Contact”, 2011 37th IEEE Photovoltaic Conference (PVSC)
2. Z.D.Eygi, U.Bostancı, R.Turan ,Ç.Erçelebi, “Optimization of Hydrogenated Amorphous Silicon (a-Si:H) Thin Films Deposited By RF Magnetron Sputtering For a-Si:H/c-Si Photovoltaic Applications.” 24th EU PVSEC, September 2009, Hamburg, Germany.
3. Z.D.Eygi, R.Turan, “Characterization of the Amorphous Silicon Thin Films Deposited by Magnetron Sputtering for a-Si /c-Si Heterojunction Solar Cells” 5. Ulusal Nanobilim ve Nanoteknoloji Konferansı, Eskisehir 2009
4. Z. D. Eygi, O. Ege, E. Yılmaz, E. Bulur “Development of High Power Blue and IR Stimulation Units for an OSL Measurement System.” Balkan Physics Letters, 2008 Special Issue, Boğaziçi University Press, (24th International Physics Congress of Turkish Physical Society, 2007, Malatya)

## **EXPERIENCES**

1. Teaching and Research Assistant, METU, Physics Department, Ankara, 2005-2012.
2. Visiting Scholar, Institute of Energy Conversion-University of Delaware, USA  
February 2010-June2011.
3. European School: Physics of Solar Cells: From Basics to Last Developments,  
February 8-13, 2009, Les Houches, France